Tectonic Evolution of Oceanic Plateaus and Hotspot-Ridge Interactions: Walvis Ridge – Rio Grande Rise, South Atlantic and Tamu Massif, Pacific Ocean

By

Sriharsha Thoram

A Dissertation Submitted to

the Department of Earth and Atmospheric Sciences,

College of Natural Sciences and Mathematics

In Partial Fulfillment

of the Requirements for the Degree

Doctor of Philosophy

in Geophysics

Chair of Committee: William W. Sager

Committee Member: Dale Bird

Committee Member: Jonny Wu

Committee Member: Maurice Tivey

University of Houston
December 2021

DEDICATION

To my parents

ACKNOWLEDGEMENTS

Firstly, I would like to thank my advisor, Dr. William W. Sager, for providing me with this invaluable opportunity to work on this challenging research and for constant mentoring and support throughout my stay at University of Houston. Secondly, I would like to thank my committee members – Dr. Dale Bird, Dr. Jonny Wu, and Dr. Maurice Tivey – for their timely assistance, insightful comments, and encouragement and for providing access to proprietary software that I could not afford.

Thanks also to my colleagues and friends, especially Abdullah, Avisha, Avradip, Ibrahim, Malik, Matt, and Yanming, for all the good memories shared in the last seven years. Thanks to the department faculty and staff for helping me in some form or the other during my stay, more so during these testing times, at University of Houston.

Finally, thanks to my family for their faith in me and for allowing me to be as ambitious as I wanted.

ABSTRACT

Oceanic plateaus are large basaltic provinces on the seafloor formed due to massive magma outpourings from an upwelling mantle. Many of these plateaus were formed at or near spreading ridges, suggesting that hotspot-ridge interaction was involved in their formation. However, the extent of ridge influence in their evolution remains unknown due to poor data coverage owing to their large size and remote locations. Magnetic anomaly patterns and geomorphology of these plateaus can provide important clues into their tectonic evolution. In this study, the tectonic evolution of three oceanic plateaus – Walvis Ridge (WR) and Rio Grande Rise (RGR) hotspot twins in South Atlantic Ocean and Shatsky Rise in Pacific Ocean – was investigated using magnetic, bathymetry, and seismic data.

In the South Atlantic, a major reorganization of the Mid-Atlantic Ridge (MAR) began before anomaly C34n (83.6 Ma) and ended before anomaly C30n (66.4 Ma), complicating the tectonics of RGR and older WR that formed together at the MAR. This reorganization is poorly understood because magnetic anomalies, C34n-C30n, are poorly defined near WR and RGR. Chapter 2 presents an initial review of magnetic anomaly picks near WR and attempts to trace down missing anomalies. Subsequently, large amounts of magnetic data from WR and RGR were collected onboard research vessels Thomas G. Thompson (2019) and Nathaniel B. Palmer (2018). In Chapter 3, magnetic anomaly maps were generated for WR and RGR using all existing magnetic data and reconstructed to their past configurations to study the tectonic evolution of the plate reorganization. The anomaly patterns indicate that WR and RGR formed around a microplate between C34n-C33n, producing various edifices at or near a reorganizing ridge.

In the northwest Pacific, a significant part of southern Shatsky Rise was mapped using multibeam sonar onboard R/V Falkor during a 2015 cruise. In Chapter 4, a new high-resolution bathymetry map of southern Shatsky Rise was generated and geomorphological implications of its tectonic and sedimentary evolution were studied in detail. The map reveals that the Tamu Massif is segmented, consisting of four smaller rises that suggest it formed by a series of ridge centered eruptions along a moving triple junction.

NOMENCLATURE

AFR	African Plate
CB	Centaurus Basin
CCD	Calcite Compensation Depth
CNS	Cretaceous Normal Superchron
COE	Crossover Errors
FZ	Fracture Zone
GMT	Generic Mapping Tools
IGRF	International Geomagnetic Reference Field
JAMSTEC	Japan Agency for Marine-Earth Science and Technology
LIP	Large Igneous Province
Ma	Mega annum or Millions of years
MAR	Mid-Atlantic Ridge
MBES	Multi Beam Echo Sounder
NCEI	National Center for Environmental Information
NRL	Naval Research Laboratory
nT	Nano Teslas
RGR	Rio Grande Rise
RJ	Ridge Jump
SA	South American Plate
TJ	Triple Junction

VB	Valdivia Bank
VT	Vema Trough
WR	Walvis Ridge

TABLE OF CONTENTS

LIST OF TABLES

LIST OF FIGURES

CHAPTER 1

INTRODUCTION

1.1 Objectives and Study Area

Oceanic plateaus are large basaltic constructions found in all major ocean basins and make up to 5% of the entire ocean floor (Figure 1.1; Harris, 2014; Sager et al., 2011). Most are often characterized by large shallow areas (> $2x10^5$ km^2) elevated ~2-3 km above the surrounding seafloor, and above average crustal thickness several times greater than regular oceanic crust (Kerr and Mahoney, 2007). These plateaus are a submarine form of Large Igneous Provinces (LIPs) and are massive crustal emplacements believed to have formed by large scale mantle melting caused by processes other than normal seafloor spreading or subduction (Coffin and Eldholm, 1994), although the mechanism underlying their formation is not well understood.

The Mantle Plume model, which has been widely used to explain plateau formation (Figure 1.2A), attributes melting to the surfacing of a deep mantle thermal plume (Richards et al., 1989; Duncan and Richards, 1991; Campbell, 2005). An alternative idea, the Plate model (Figure 1.2B), explains the massive eruptions through decompression melting of fertile (low melting point) upper mantle material (Foulger, 2007; Anderson and Natland, 2014).

Whatever mechanism led to the formation of oceanic plateaus; their subsequent evolution is also poorly understood. In its simplest form, these plateaus cool and subside with the lithosphere while they get buried by a drape of pelagic sedimentation. During this process, their summits often rise above the Carbonate Compensation Depth (CCD), accumulating a thick carbonate sediment cap (Moberly and Larson, 1975; Sliter and Brown, 1993). Plateaus can also come back to life, volcanically speaking, rejuvenated with small-volume volcanism after tens of millions of years quiescence (Homrighausen et al., 2019; Tejada et al., 2016). Since these oceanic plateaus are usually large and located in remote locations (Figure 1.1), most such inferences are based on scant data and not completely accurate.

Some researchers have noted that oceanic plateaus commonly form at spreading ridges (e.g., Whittaker et al, 2015; Sager et al., 2019), suggesting a strong link between ridge and plume volcanism. But the extent to which a spreading ridge controls the evolution of a plateau is unclear.

Linear magnetic anomalies (magnetic lineations) are recorded in the seafloor due to combination of crustal formation at divergent plate boundaries (midocean ridges) and geomagnetic field reversals (Vine and Matthews, 1963; Vine, 1966). These magnetic lineations can be used to determine the past positions of spreading ridges and studying these patterns can provide important clues on the tectonic evolution of an oceanic plateau and its relation to the coeval spreading ridges.

The geomorphology of oceanic plateaus reflects their formation processes and history, but bathymetric data over most of these structures are rudimentary owing to the difficulty of surveying large undersea features, resulting in a sparse distribution of high-resolution data. Multibeam-echosounder (MBES) data have become more common and provide significant improvement in horizontal topographic resolution and therefore have the potential to provide important clues about oceanic plateau formation.

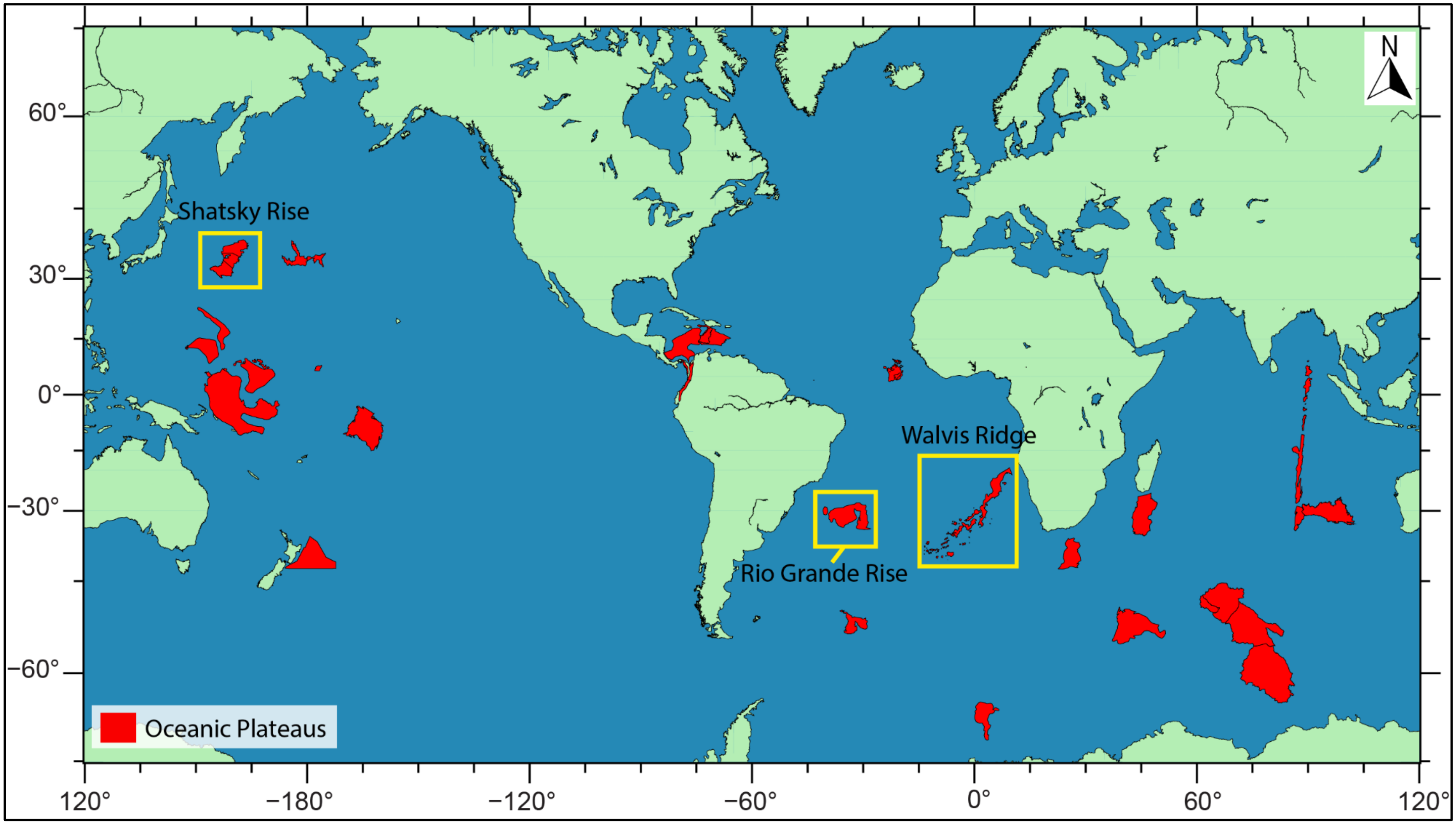

Figure 1.1 – World Map of various oceanic plateaus. Oceanic plateaus investigated in this dissertation are bounded by yellow rectangles. Digital data for oceanic plateaus are obtained from Coffin et al., 2013 and plotted using GMT (Wessel et al., 2019)

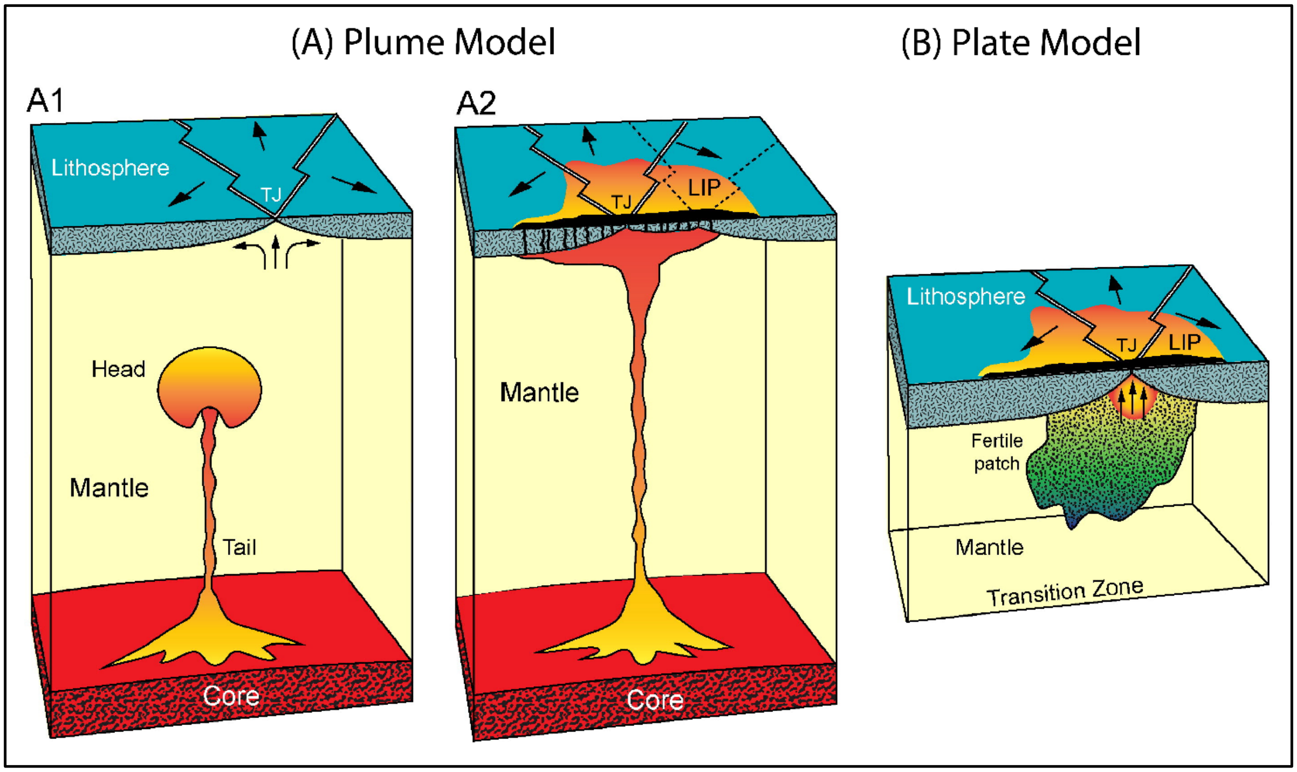

Figure 1.2 – Sketch depicting two models explaining the formation of oceanic plateaus. (A) The plume model - A large voluminous blob of magma is generated at the core-mantle boundary and rises trough the upper mantle (A1). This blob of magma erupts at the lithosphere producing massive amounts of volcanic material (A2). (B) The plate model - A fertile shallow mantle material patch exists under a thin lithosphere. The rifting of this lithosphere causes this fertile material to melt due to decompression melting producing massive amounts of magma. (Modified from Sager et al., 2016)

This study investigates the tectonic evolution of three oceanic plateaus by analyzing magnetic, bathymetry, and seismic data (Figure 1.1) – Walvis Ridge and Rio Grande Rise (South Atlantic) and Shatsky Rise (Pacific Ocean). For this purpose, vast amounts of geophysical data were collected onboard R/V Falkor (Shatsky Rise, 2015), R/V Nathaniel Palmer (Rio Grande Rise, 2018), and R/V Thomas G. Thompson (Walvis Ridge, 2019). This newly acquired data along with the pre-existing data in the region was used to study the tectonic evolution of these plateaus and deepen our understanding of oceanic plateau evolution and ridge-hotspot interactions.

This dissertation is comprised of four chapters:

1. Chapter 1 establishes the context behind this research and its main objectives. It also summarizes the outline of this dissertation.
2. Chapter 2 is adapted from a journal paper published in Geophysical Research Letters (Thoram et al., 2019), reformatted for this dissertation. This chapter analyzes the existing magnetic data over Walvis Ridge to identify Late Cretaceous magnetic anomalies C34n (83.6 Ma) to C30n (66.4 Ma) that were not mapped by prior studies and understand their tectonic implications on the evolution of Walvis Ridge.
3. Chapter 3 is an extension of Chapter 2 and provides a detailed outlook on the tectonic evolution of Walvis Ridge and Rio Grande Rise that formed together at the Mid-Atlantic Ridge during Late Cretaceous. In this chapter, magnetic anomaly maps of these plateaus were generated using both newly acquired and existing magnetic data. These maps were then reconstructed back to their previous configurations to study the Late Cretaceous tectonic evolution of Walvis Ridge and Rio Grande Rise.
4. In Chapter 4, an improved bathymetry map of Tamu Massif and southern Shatsky Rise is generated by merging multibeam bathymetry data with a satellite altimetry-based bathymetry model for Shatsky Rise. This improved bathymetry map is then used to better understand the geological evolution of this plateau.

1.2 Bibliography

Anderson, D., & Natland, J. (2014). Mantle updrafts and mechanisms of oceanic volcanism. Proceedings of the National Academy of Sciences, 111(41), E4298–E4304.

Campbell, I. (2005). Large igneous provinces and the mantle plume hypothesis. Elements, 1(5), 265–269.

Coffin, M., & Eldholm, O. (1994). Large igneous provinces: crustal structure, dimensions, and external consequences. Reviews of Geophysics, 32(1), 1–36.

Coffin, M. F., Gahagan, L. M., Lawver, L. A., & Dalziel, I. W. D. (2013). Large Igneous Provinces: Map and Data. University of Texas Institute for Geophysics Technical Report No. 221 (2013), 1p plus data

Duncan, R., & Richards, M. (1991). Hotspots, mantle plumes, flood basalts, and true polar wander. Reviews of Geophysics, 29(1), 31–50.

Foulger, G. (2007). The "plate" model for the genesis of melting anomalies. Special Papers-Geological Society of America, 430, 1.

Harris, P., Macmillan-Lawler, M., Rupp, J., & Baker, E. (2014). Geomorphology of the oceans. Marine Geology, 352, 4–24.

Homrighausen, S., Hoernle, K., Hauff, F., Wartho, J.-A., van den Bogaard, P., & Garbe-Schönberg, D. (2019). New age and geochemical data from the Walvis Ridge: The temporal and spatial diversity of South Atlantic intraplate volcanism and its possible origin. Geochimica et Cosmochimica Acta, 245, 16–34.

Kerr, A., & Mahoney, J. (2007). Oceanic plateaus: Problematic plumes, potential paradigms. Chemical Geology, 241(3-4), 332–353.

Moberly, R., Larson, R.L., 1975. Synthesis of deep sea drilling results from Leg 32 in the northwest Pacific Ocean. In: Moberly, R., Larson, R.L., et al. (Eds.), Init. Repts. DSDP. 32. U.S. Govt. Printing Office, Washington, DC, pp. 945–957.

Richards, M., Duncan, R., & Courtillot, V. (1989). Flood basalts and hot-spot tracks: plume heads and tails. Science, 246(4926), 103–107.

Sager, W. W., Sano, T., & Geldmacher, J. (2011). How do oceanic plateaus form? Clues from drilling at Shatsky Rise. Eos, Transactions American Geophysical Union, 92(5), 37–38.

Sager, W., Sano, T., & Geldmacher, J. (2016). Formation and evolution of Shatsky Rise oceanic plateau: Insights from IODP Expedition 324 and recent geophysical cruises. Earth-science reviews, 159, 306–336.

Saunders, A., England, R., Reichow, M., & White, R. (2005). A mantle plume origin for the Siberian traps: uplift and extension in the West Siberian Basin, Russia. Lithos, 79(3-4), 407–424.

Sliter, W.V., Brown, G.R., 1993. Shatsky Rise: seismic stratigraphy and sedimentary record of Pacific paleoceanography since the Early Cretaceous. In: Natland, J.H.,Storms, M.A., et al. (Eds.), Proc. ODP, Sci. Res. 132. Ocean Drilling Program, College Station, TX, pp. 3–13.

Tejada, M. L. G., Geldmacher, J., Hauff, F., Heaton, D., Koppers, A. A. P., Garbe-Schönberg, D., Sager, W. W. (2016). Geochemistry and age of Shatsky, Hess, and Ojin Rise seamounts: Implications for a connection between the Shatsky and Hess Rises. Geochimica et Cosmochimica Acta, 185, 302–327.

Thoram, S., Sager, W. W., & Jokat, W. (2019). Implications of updated magnetic anomalies for the Late Cretaceous tectonic evolution of Walvis Ridge. Geophysical Research Letters, 46(16), 9474–9482.

Vine, F., & Matthews, D. (1963). Magnetic anomalies over oceanic ridges. Nature, 199(4897), 947–949.

Wessel, P., Luis, J. F., Uieda, L., Scharroo, R., Wobbe, F., Smith, W. H. F., & Tian, D. (2019). The generic mapping tools version 6. Geochemistry, Geophysics, Geosystems, 20(11), 5556–5564.

CHAPTER 2

IMPLICATIONS OF UPDATED MAGNETIC ANOMALIES FOR THE LATE CRETACEOUS TECTONIC EVOLUTION OF WALVIS RIDGE

2.1 Introduction

Walvis Ridge (WR) and Rio Grande Rise (RGR) are two prominent Large Igneous Provinces in the South Atlantic Ocean (Figure 2.1). WR is a southwest trending submarine ridge extending from the coast of Namibia to the islands of Tristan and Gough near the Mid-Atlantic Ridge (MAR), whereas RGR is a submarine plateau east of Brazil. During the Late Cretaceous, the old WR (Frio Ridge, Valdivia Bank and Central WR) and main RGR (RGR Massif) were emplaced at or near the MAR axis by a Tristan-Gough hotspot (Morgan, 1981; O'Connor & Duncan, 1990; O'Connor & Jokat, 2015a). About 60-70 Ma, the MAR moved away from the hotspot, and as a result RGR formation ceased and three seamount chains were formed on the African plate, their volcanism continuing to the present day (O'Connor & Duncan, 1990; O'Connor & Jokat, 2015a).

Though formed in similar settings, WR and RGR exhibit contrasting morphologies. WR is mostly a linear ridge but changes character along its length, whereas RGR consists of two subrounded plateaus (RGR Massif and SE-RGR) and a spreading-axis parallel ridge (E-RGR; Figure 2.1). O'Connor and Jokat (2015a, 2015b) attribute changes in WR morphology to the interaction of the hotspot and MAR and their divergence during the Cenozoic.

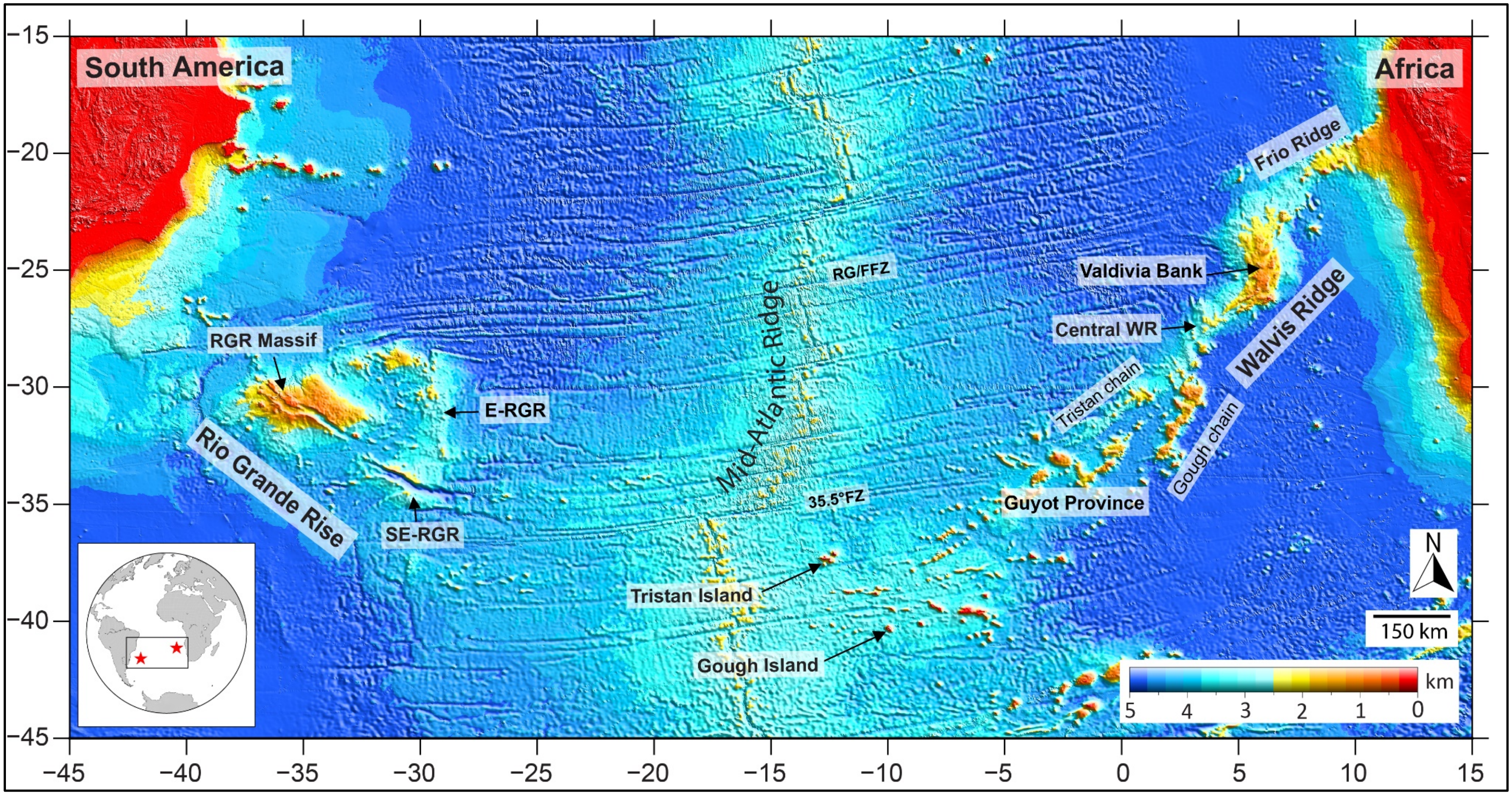

Figure 2.1 – Bathymetry of the South Atlantic Ocean; features of the Walvis Ridge and Rio Grande Rise. Background is satellite-predicted bathymetry (Smith & Sandwell, 1997). RG/FFZ = Rio Grande - Florianopolis Fracture Zone; RGR = Rio Grande Rise; WR = Walvis Ridge.

Authors have tried to fit the WR with hotspot models having a monotonic age progression (Duncan, 1981; O'Connor & le Roex, 1992; Müller et al., 1993; Torsvik et al., 2008; Doubrovine et al., 2012), but the chain has a complex morphology that fits partly with simple hotspot models. WR begins offshore of Africa as a narrow ridge (Frio Ridge) near the continental margin, continues as an oceanic plateau (Valdivia Bank) at right angles, changes to a series of N-S trending ridges (Central WR), and finally splits into three distinct seamount chains (Guyot Province; Figure 2.1). In response, authors have resorted to models with multiple hotspots (O'Connor & le Roex, 1992), moving hotspots (Doubrovine et al., 2012), and hotspot-ridge interaction (O'Connor & Jokat, 2015a, 2015b) to explain WR morphologic changes.

A tectonic reorganization occurred near WR and RGR between anomalies C34n-C30n (Cande et al., 1988; Sager et al., 2021), during which a long right-lateral transform fault, once located north of Frio Ridge at the Rio Grande- Florianopolis Fracture Zone (FZ; e.g., Pérez-Díaz & Eagles, 2014), broke up and reformed as smaller offset transforms ~10° farther south. This reorganization is not well understood as magnetic isochrons C34n-C30n are poorly defined in the vicinity of WR owing to sparse ship track coverage (Figure 2.2). Coincidently, spreading rate reduced from ~70 mm/year (end of C34) to ~40 mm/year (end of C30), several new FZs formed between WR and RGR, and eastward ridge jumps occurred (Cande et al., 1988; Sager et al., 2021). Tectonic fabric and magnetic anomalies in the spreading corridor between WR and RGR and the Rio Grande-Florianopolis FZ and 35.5°S FZ (Figure 2.1) indicate that the reorganization occurred within these bounds (Sager et al., 2021). Previous studies (Cande et al., 1988) failed to identify anomalies C34n-C33n along the WR and avoided making picks over bathymetric features (including Valdivia Bank).

Several studies (Cande et al., 1988; Huang et al., 2018; Nakanishi et al., 1999; Sager et al., 2019) have documented linear magnetic anomalies in oceanic plateaus formed near spreading centers, providing important information on their tectonic history. Cande et al. (1988) mapped anomaly C34n-C33o in RGR, suggesting that these anomalies might also be found in WR. Our current understanding of anomaly C34n geometry over WR comes mainly from RGR picks rotated across the Atlantic and may do not accurately reflect MAR position owing to complex tectonics and microplate formation (Sager et al., 2021). Because the seafloor generated by spreading is dictated by the opening between separating plates, missing anomalies on a plate have either not been identified or been transferred to the conjugate plate owing to a ridge jump.

In this study, new and preexisting magnetic data (Figures 2.2 and Table 2.1) were analyzed to improve our understanding of magnetic anomalies and tectonic implications around WR. This study focuses on the anomalies between C34n-C30n (83.6 and 66.4 Ma, respectively), the magnetic anomalies that potentially record details of the plate reorganization. After anomaly C30n, South Atlantic spreading is highly regular, indicating stable tectonics.

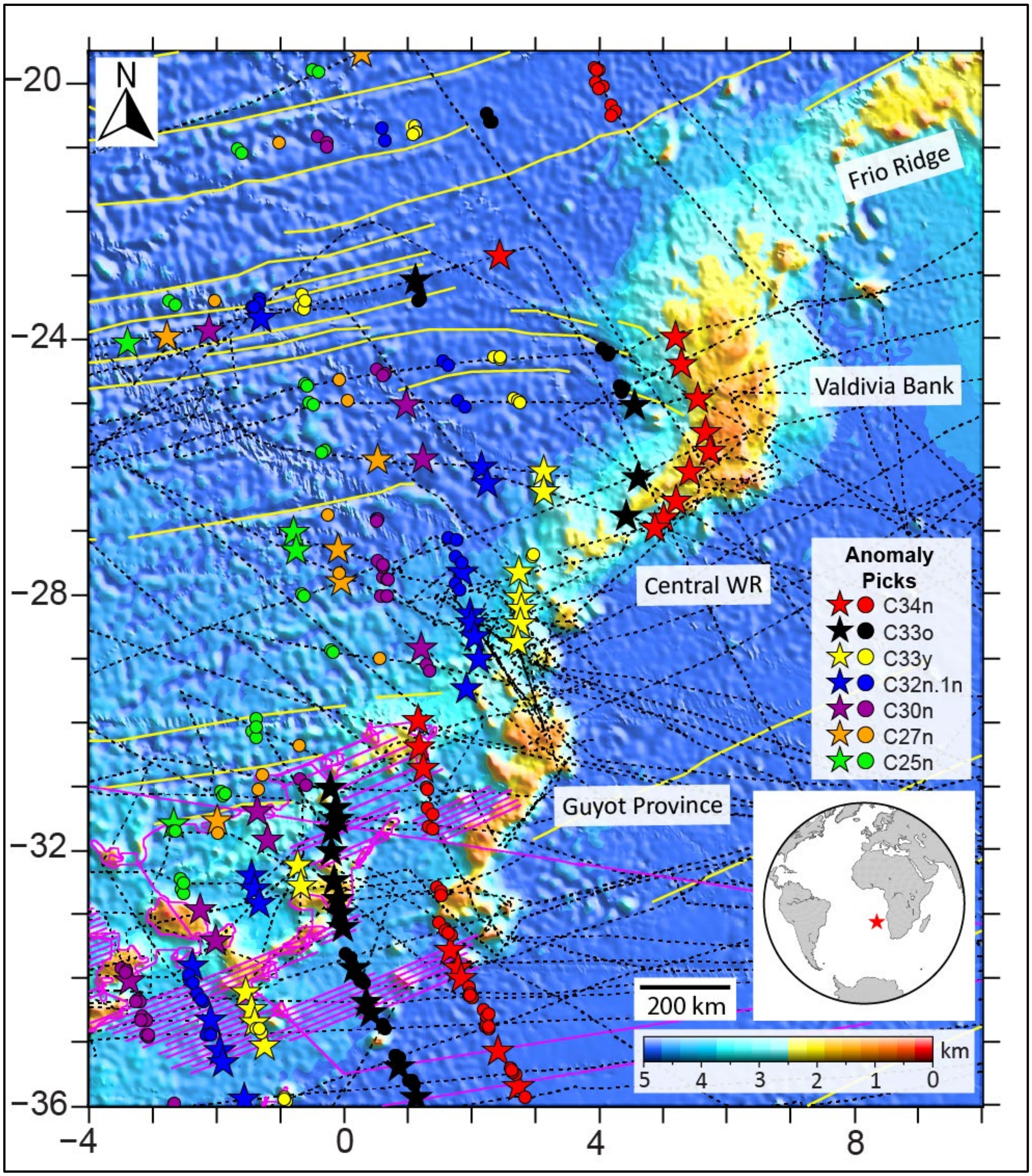

Figure 2.2 – Walvis Ridge bathymetry and magnetic anomaly picks from C25n to C34n. Background is satellite-predicted bathymetry (Smith & Sandwell, 1997). Stars denote new magnetic picks identified in this study. Circles denote magnetic picks from prior studies (Cande et al., 1988) published in the Global Seafloor Feature and Magnetic Lineations database project (Seton et al., 2014). Yellow lines represent fracture zones; pink lines denote new data tracks; black dashed lines show data tracks from the National Centers for Environmental Information repository.

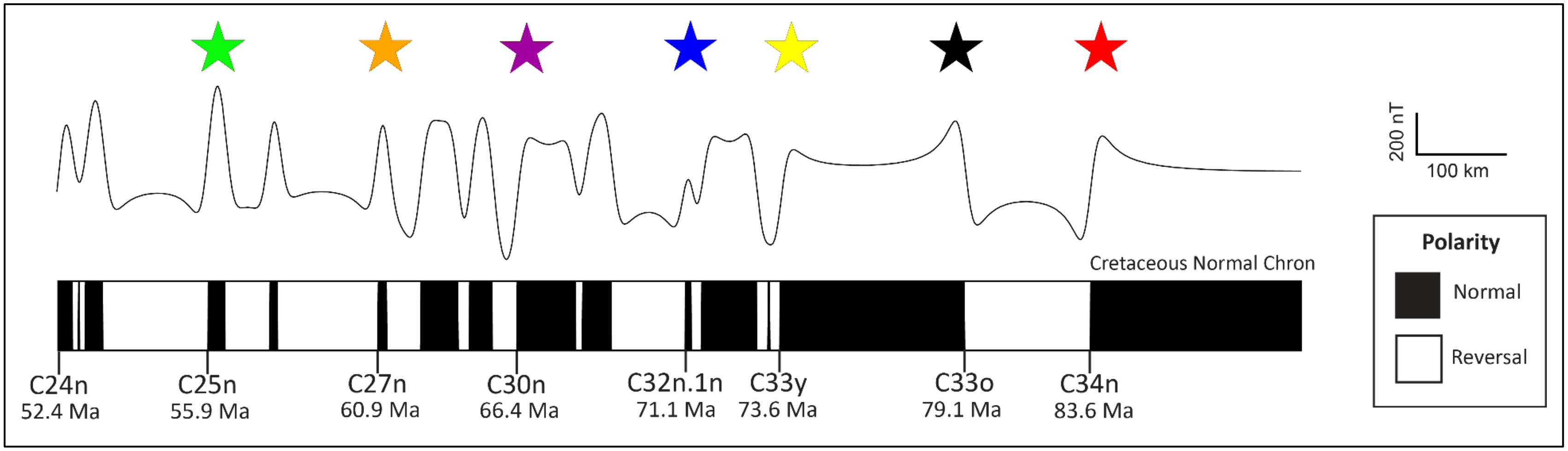

Figure 2.3 – Magnetic anomaly model for area near Walvis Ridge. Polarity sequence (Ogg, 2012) is shown at the bottom and the calculated anomaly model is shown above. Colored, filled stars are used to represent anomaly picks in Figures 2.2, 2.4, 2.8, 2.9, 2.10. The model has been generated assuming a half spreading rate of 35 kmMyr-1, an oceanic crust magnetic layer thickness of 1 km (top: 3 km and bottom: 4 km) and a magnetization of 10 Am-1. The direction of the current magnetic field is calculated at site 25°N, 6°E. The present Inclination is -66.5° and present declination is -16.94°. The remanent field directions were (Inclination = -42.9°, Declination = -6.0°) calculated using the Africa paleomagnetic pole for 80 Ma (Besse and Courtillot, 2002). The lineation azimuth is 164°.

2.2 Data and Methods

A total of ~9,000 line km of new magnetic data that was collected during several geophysical research expeditions (Figure 2.2 and Table 2.1), are available around WR. But there are large gaps in many places between tracks covering anomalies C34n-C33y in the vicinity of WR. In this document, a pick is a selected location of a particular anomaly interpreted on a magnetic profile. Following the convention used in Müller et al. (1999), a pick always represents the young end of an anomaly. Some anomaly picks published in the Global Seafloor Feature and Magnetic Lineation Database Project (Seton et al., 2014) do not coincide with available magnetic trackline data from the National Centers for Environmental Information (NCEI), suggesting that they were based on unarchived or proprietary data. We also found few errors in the published magnetic picks, suggesting that there were problems with digitization, interpretation, navigation, or bookkeeping.

Table 2.1 – Magnetic Data Source Cruises

Cruise ID	Year	Source Institution	Ship
V1604	1959	Lamont–Doherty Geological Observatory	*Vema*
V1809	1962	Lamont–Doherty Geological Observatory	*Vema*
RC0801	1963	Lamont–Doherty Geological Observatory	*Robert D. Conrad*
V1912	1963	Lamont–Doherty Geological Observatory	*Vema*
V2011	1964	Lamont–Doherty Geological Observatory	*Vema*
V2204	1966	Lamont–Doherty Geological Observatory	*Vema*
V2206	1966	Lamont–Doherty Geological Observatory	*Vema*
RC1103	1967	Lamont–Doherty Geological Observatory	*Robert D. Conrad*
V2412	1967	Lamont–Doherty Geological Observatory	*Vema*
AMC0168	1968	NOAA	*Discoverer*
CIRC08AR	1968	Scripps Institution of Oceanography	*Argo*
V2605	1968	Lamont–Doherty Geological Observatory	*Vema*
RC1214	1969	Lamont–Doherty Geological Observatory	*Robert D. Conrad*
CH099L04	1970	Woods Hole Oceanographic Institution	*Chain*
RC1312	1970	Lamont–Doherty Geological Observatory	*Robert D. Conrad*
RC1313	1970	Lamont–Doherty Geological Observatory	*Robert D. Conrad*
RC1314	1970	Lamont–Doherty Geological Observatory	*Robert D. Conrad*

A2060L05	1971	Woods Hole Oceanographic Institution	*Atlantis II*
A2067L02	1972	Woods Hole Oceanographic Institution	*Atlantis II*
A2067L03	1972	Woods Hole Oceanographic Institution	*Atlantis II*
A2067L04	1972	Woods Hole Oceanographic Institution	*Atlantis II*
A2067L05	1972	Woods Hole Oceanographic Institution	*Atlantis II*
A2067L06	1972	Woods Hole Oceanographic Institution	*Atlantis II*
A2067L07	1972	Woods Hole Oceanographic Institution	*Atlantis II*
RC1504	1972	Lamont–Doherty Geological Observatory	*Robert D. Conrad*
RC1604	1972	Lamont–Doherty Geological Observatory	*Robert D. Conrad*
V2905	1972	Lamont–Doherty Geological Observatory	*Vema*
V2906	1972	Lamont–Doherty Geological Observatory	*Vema*
CH115L02	1973	Woods Hole Oceanographic Institution	*Chain*
RC1703	1973	Lamont–Doherty Geological Observatory	*Robert D. Conrad*
CH115L03	1974	Woods Hole Oceanographic Institution	*Chain*
CH115L04	1974	Woods Hole Oceanographic Institution	*Chain*
CH115L05	1974	Woods Hole Oceanographic Institution	*Chain*
DSDP39GC	1974	Scripps Institution of Oceanography	*Glomar Challenger*
DSDP40GC	1974	Scripps Institution of Oceanography	*Glomar Challenger*
A2093L02	1975	Woods Hole Oceanographic Institution	*Atlantis II*
A2093L03	1975	Woods Hole Oceanographic Institution	*Atlantis II*
78009911	1978	France IFREMER	*Jean Charcot*
AG04	1978	S Africa Data Center Ocean	*Agulhas*
INMD12MV	1978	Scripps Institution of Oceanography	*Melville*
RC2105	1978	Lamont–Doherty Geological Observatory	*Robert D. Conrad*
TD377	1978	S Africa Cape Town, U	*Thomas B. Davie*
79000211	1979	France IFREMER	*Jean Charcot*
79000212	1979	France IFREMER	*Jean Charcot*
AG06	1979	S Africa Data Center Ocean	*Agulhas*
AG08	1979	S Africa Data Center Ocean	*Agulhas*
AG16	1979	S Africa Data Center Ocean	*Agulhas*
FM0102	1979	Univ. Texas Institute for Geophysics	*Fred H. Moore*
FM0103	1979	Univ. Texas Institute for Geophysics	*Fred H. Moore*
FM0104	1979	Univ. Texas Institute for Geophysics	*Fred H. Moore*
FM0105	1979	Univ. Texas Institute for Geophysics	*Fred H. Moore*
TBD396	1979	S Africa Geological Survey	*Thomas B. Davie*
TD388	1979	S Africa Cape Town, U	*Thomas B. Davie*
TD397	1979	S Africa Cape Town, U	*Thomas B. Davie*
AG10	1980	S Africa Data Center Ocean	*Agulhas*
DSDP73GC	1980	Scripps Institution of Oceanography	*Glomar Challenger*
DSDP74GC	1980	Scripps Institution of Oceanography	*Glomar Challenger*
DSDP75GC	1980	Scripps Institution of Oceanography	*Glomar Challenger*
V3620	1981	Lamont–Doherty Geological Observatory	*Vema*
MRTN10WT	1984	Scripps Institution of Oceanography	*Thomas Washington*

MRTN13WT	1985	Scripps Institution of Oceanography	*Thomas Washington*
RC2711	1986	Lamont–Doherty Geological Observatory	*Robert D. Conrad*
RC2802	1987	Lamont–Doherty Geological Observatory	*Robert D. Conrad*
EW9011	1990	Lamont–Doherty Geological Observatory	*Maurice Ewing*
PLUM04WT	1990	Scripps Institution of Oceanography	*Thomas Washington*
PLUM05WT	1990	Scripps Institution of Oceanography	*Thomas Washington*
EW9309	1993	Lamont–Doherty Geological Observatory	*Maurice Ewing*
NBP0102	2001	Lamont–Doherty Geological Observatory	*Nathaniel B. Palmer*
VANC05MV	2002	Scripps Institution of Oceanography	*Melville*
MR03-K04	2003	JAMSTEC	*Mirai*
ANT XXIII-5	2006	Alfred Wegener Institute	*Polarstern*
MV1203	2012	Scripps Institution of Oceanography	*Melville*
YK13-04	2013	JAMSTEC	*Yokosuka*

Cruise ID bold = New data since (Cande et al., 1988)
MR03-K04, YK13-04 available on Jamstec database (http://www.godac.jamstec.go.jp/darwin)
ANT XXIII-5, MV1203 available on Earthref.org
(MV1203 - http://earthref.org/ERDA/2398/ ; ANTXXIII-5 - http://earthref.org/ERDA/2397/)
All other cruises available from NCEI database (https://www.ngdc.noaa.gov/)

For this study, we reexamined all available magnetic trackline data in the study area and reanalyzed magnetic profiles over bathymetric features to improve anomaly pick coverage near WR. From the total field, the twelfth generation International Geomagnetic Reference Field (Thébault et al., 2015) was removed to produce magnetic anomalies. Anomalies were in turn analyzed by modeling profiles using a current geomagnetic polarity time scale (Ogg, 2012) to identify seafloor spreading magnetic anomalies (Figure 2.3). We used the EMAG2v3 global magnetic grid (Meyer et al., 2017; Figure 2.4) to help identify the trends in magnetic anomalies and validate the picking process. Because EMAG2v3 is a gridded data collection with no evidence of data control, it can't be utilized to find anomalies. As a result, all anomaly picks presented here were made from individual magnetic anomaly tracks (Figure 2.5 – 2.7).

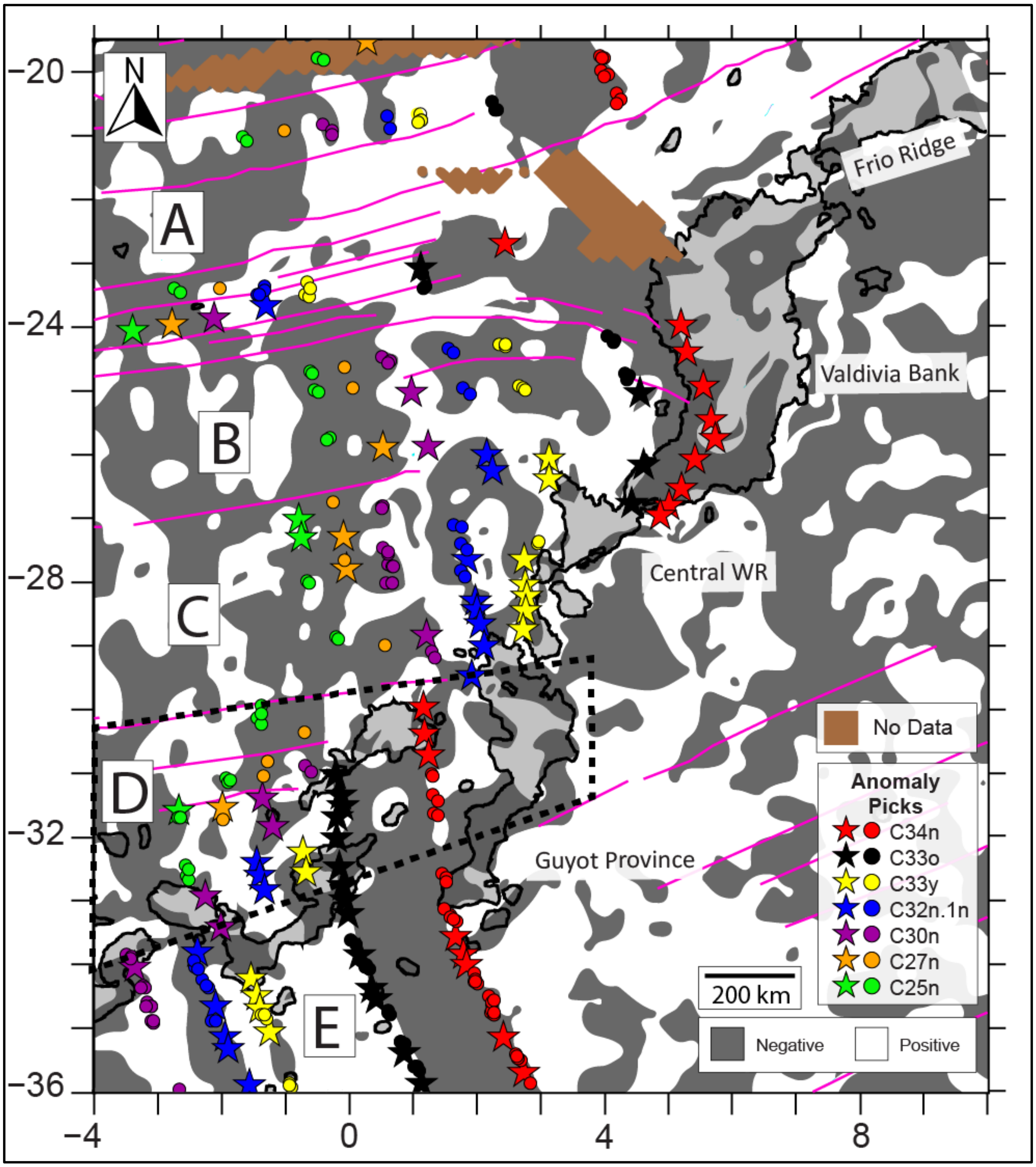

Figure 2.4 – Magnetic anomaly picks and EMAG2v3 global magnetic grid (Meyer et al., 2017) near WR. White (gray) areas denote positive (negative) magnetic anomaly values from EMAG2v3. Brown colored areas in EMAG2v3 have no data to define the anomaly. Magnetic anomaly picks from C25n to C34n are plotted by symbols. Stars denote the new magnetic picks identified in this study. Circles denote magnetic picks from previous studies (Cande et al., 1988) published in the Global Seafloor Feature and Magnetic Lineations database project (Seton et al., 2014). Letters refer to spreading corridors discussed in text. Dashed box represents spreading Corridor D. Light gray polygons represent WR bathymetry above the 3,000-m contour. Pink lines represent fracture zones. WR = Walvis Ridge.

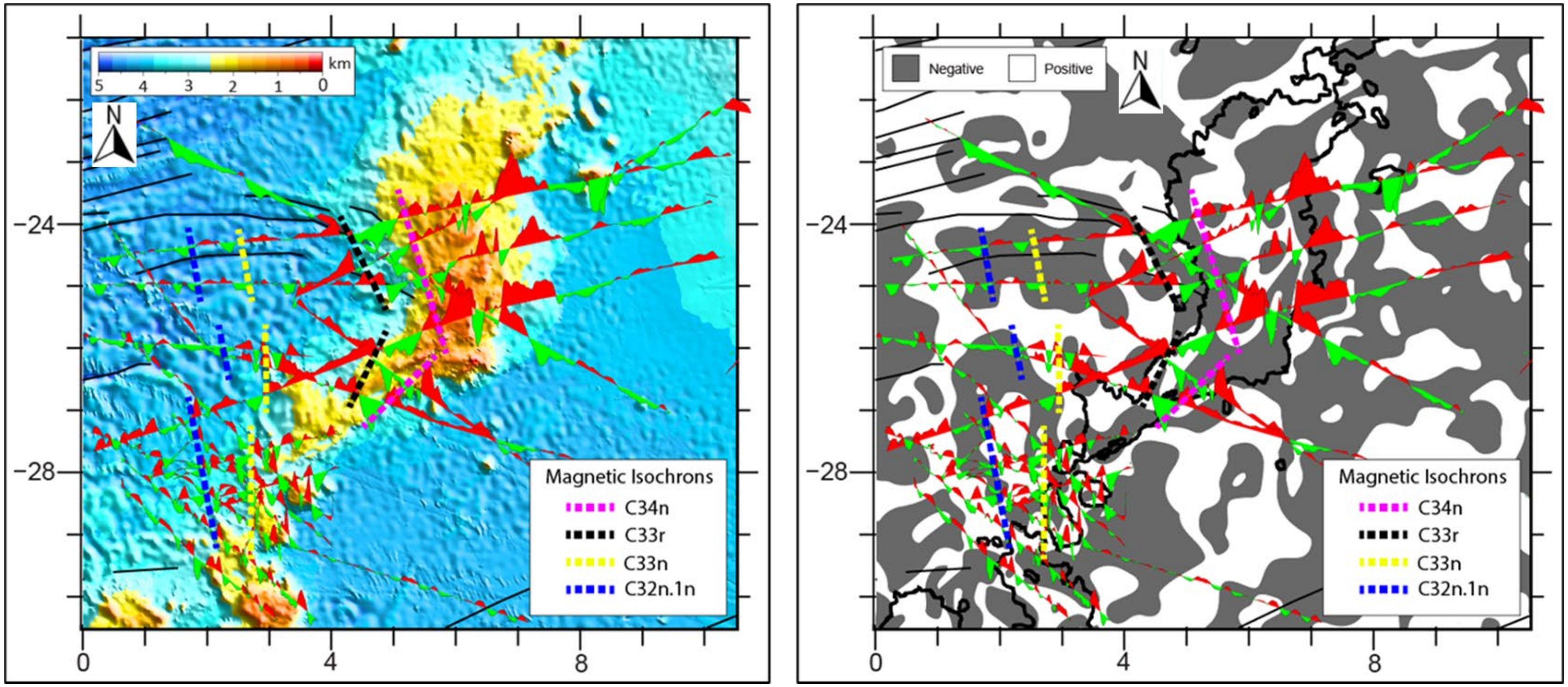

Figure 2.5 – Wiggle plot of key magnetic profiles along Valdivia Bank and Central WR. Anomalies are plotted perpendicular to ship tracks (thin black lines) and shaded red if positive and green if negative. Colored, dashed lines show anomaly correlations. Black lines represent FZs. Background is (left) satellite-predicted bathymetry (Smith and Sandwell, 1997); (right) EMAG2v3 (Meyer et al., 2017) global magnetic grid.

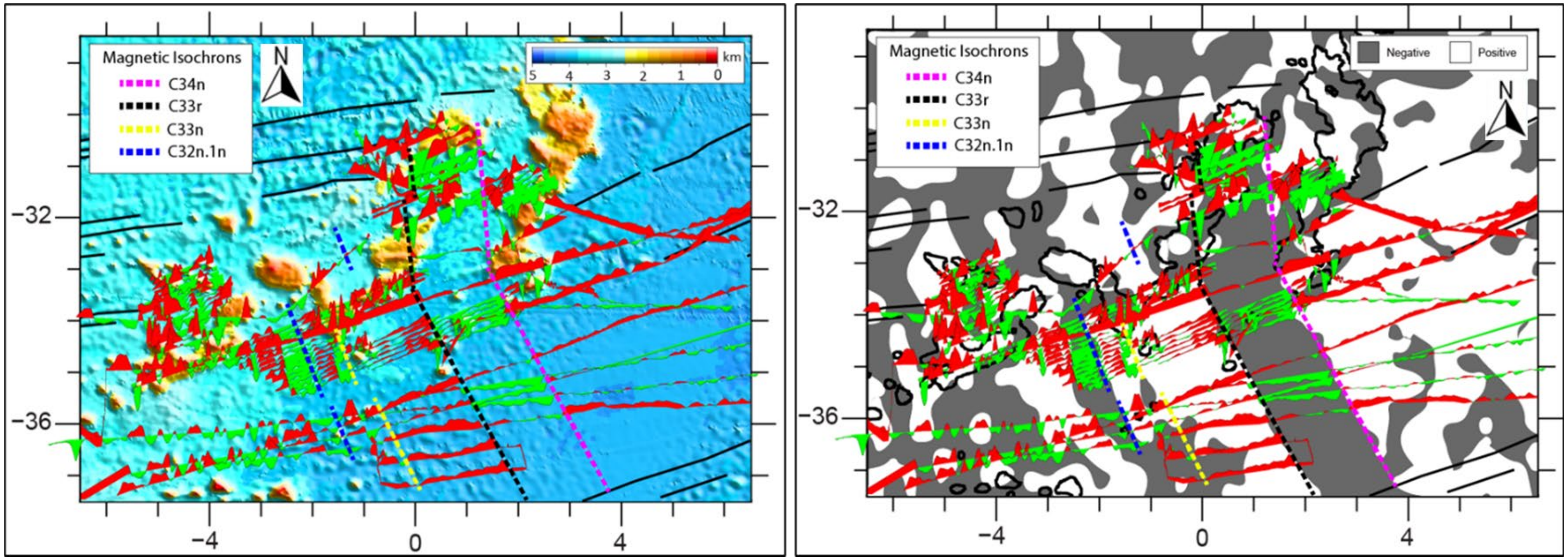

Figure 2.6 – Wiggle plot of key magnetic profiles in Guyot Province. Anomalies are plotted perpendicular to ship tracks (thin black lines) and shaded red if positive and green if negative. Colored, dashed lines show anomaly correlations. Black lines represent FZs. Background is (top) satellite-predicted bathymetry (Smith and Sandwell, 1997); (bottom) EMAG2v3 (Meyer et al., 2017) global magnetic grid.

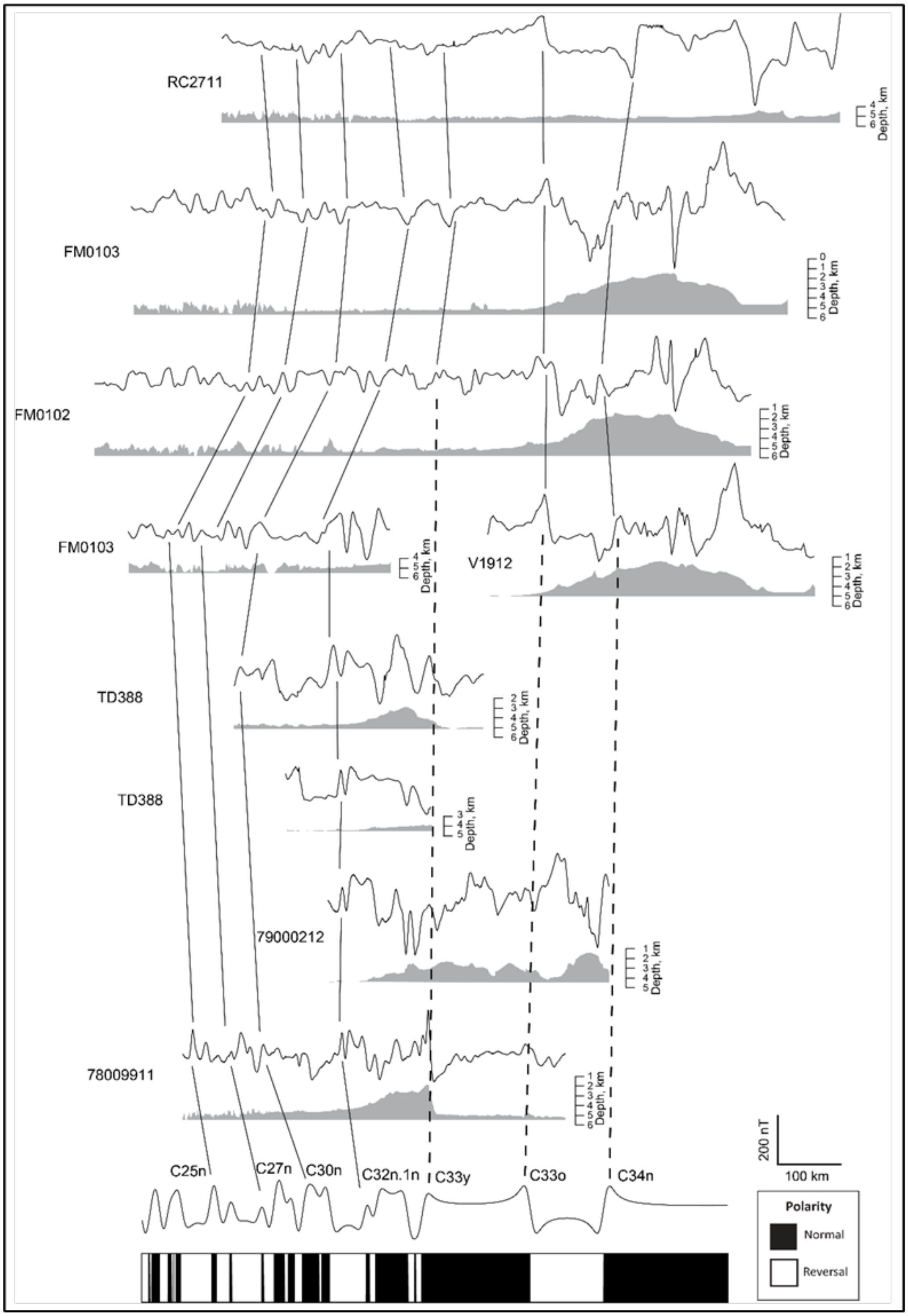

Figure 2.7 – Cartesian plot showing magnetic anomaly profiles with underlying bathymetry for key magnetic tracks along Valdivia Bank and Central WR. The profiles have been projected perpendicular to the spreading axis. The profiles are arranged N to S. Thin solid and dashed lines denote correlations for anomalies C25n – C34n between the model and various profiles. Anomaly model details are mentioned in Figure 2.3. Black lines show correlations between adjacent profiles. Black dashed lines show correlations between non-adjacent profiles.

Several studies (Cande et al., 1988; Huang et al., 2018; Nakanishi et al., 1999; Sager et al., 2019) have shown that linear magnetic anomalies can be mapped over oceanic plateaus (such as RGR Massif and Valdivia Bank) formed near spreading centers. To confirm that our anomaly picks over Valdivia Bank indeed originate due to lateral polarity changes in oceanic crust and not due to bathymetry, we modeled the magnetization from the magnetic field and bathymetry for key magnetic profiles over Valdivia Bank (Figure 2.8) and found that the anomalies bear no obvious relation to topography. Following the standard convention (e.g., Cande et al. (1988), Müller et al. (1999)), all magnetic anomaly picks (isochrons or "chrons") correspond to the young end of the normal polarity block anomaly, except for anomaly C33o, where it corresponds to the young end of the reversed block (Figure 2.3). The following magnetic picks were identified – C25n (57.1 Ma), C27n (62.2 Ma), C30n (66.4 Ma), C32n.1n.1n (71.4 Ma), C33y (74.2 Ma), C33o (79.9), and C34n (83.6 Ma) (Ogg, 2012). In the following text, when describing magnetic anomalies, we use the appropriate chron number and append its polarity; for example, chrons C33y and C33o bracket positive anomaly C33n, whereas chrons C33o and C34n bound negative anomaly C33r (see caption of Figure 2.3).

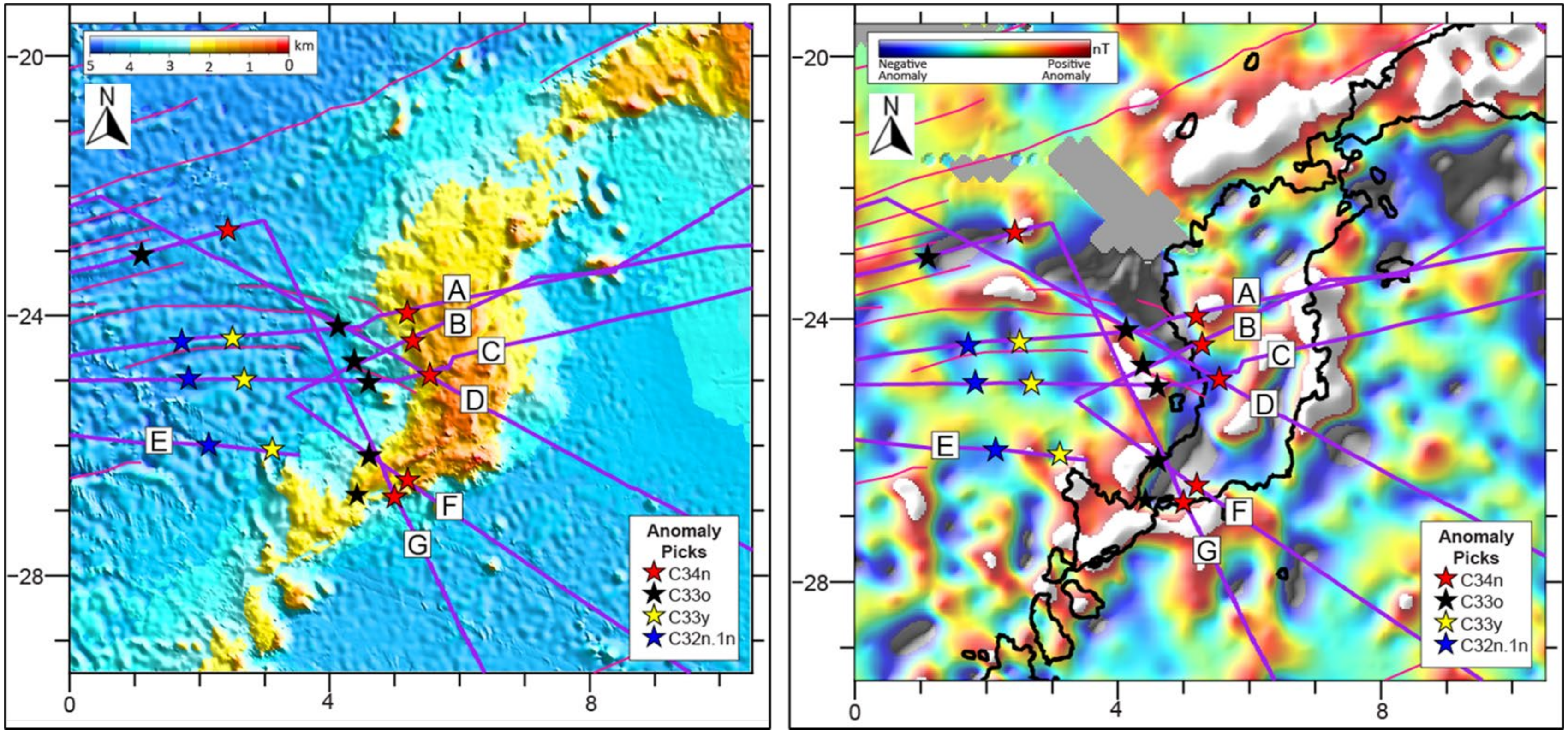

Figure 2.8 – Magnetization modeling (Parker and Heuestis, 1974) using magnetic field and bathymetry for key profiles over Valdivia Bank. (This page) Maps showing profile tracks (Purple lines) along with an ID, plotted on (left) predicted bathymetry (Sandwell and Smith, 1997) and (right) EMAG2v3 (Meyer et al., 2017); (Next page) Calculated magnetization profiles (Red) plotted along with anomaly field (Blue) and bathymetry (Gray). Anomaly picks are shown by symbols at the top of each profile. The modeling was done assuming a geocentric dipole direction and that the magnetization is remanent and using Fourier inversion approach using these parameters: wavelength cutoff (low = 10 km and high = 300km), thickness of source layer (constant, 1km), observation level (sea level). Pink lines denote FZs. Profile A=FM0102; B, F=V1912; C, E=FM0103; D=V2011; G=RC2711. Stars represent isochron picks.

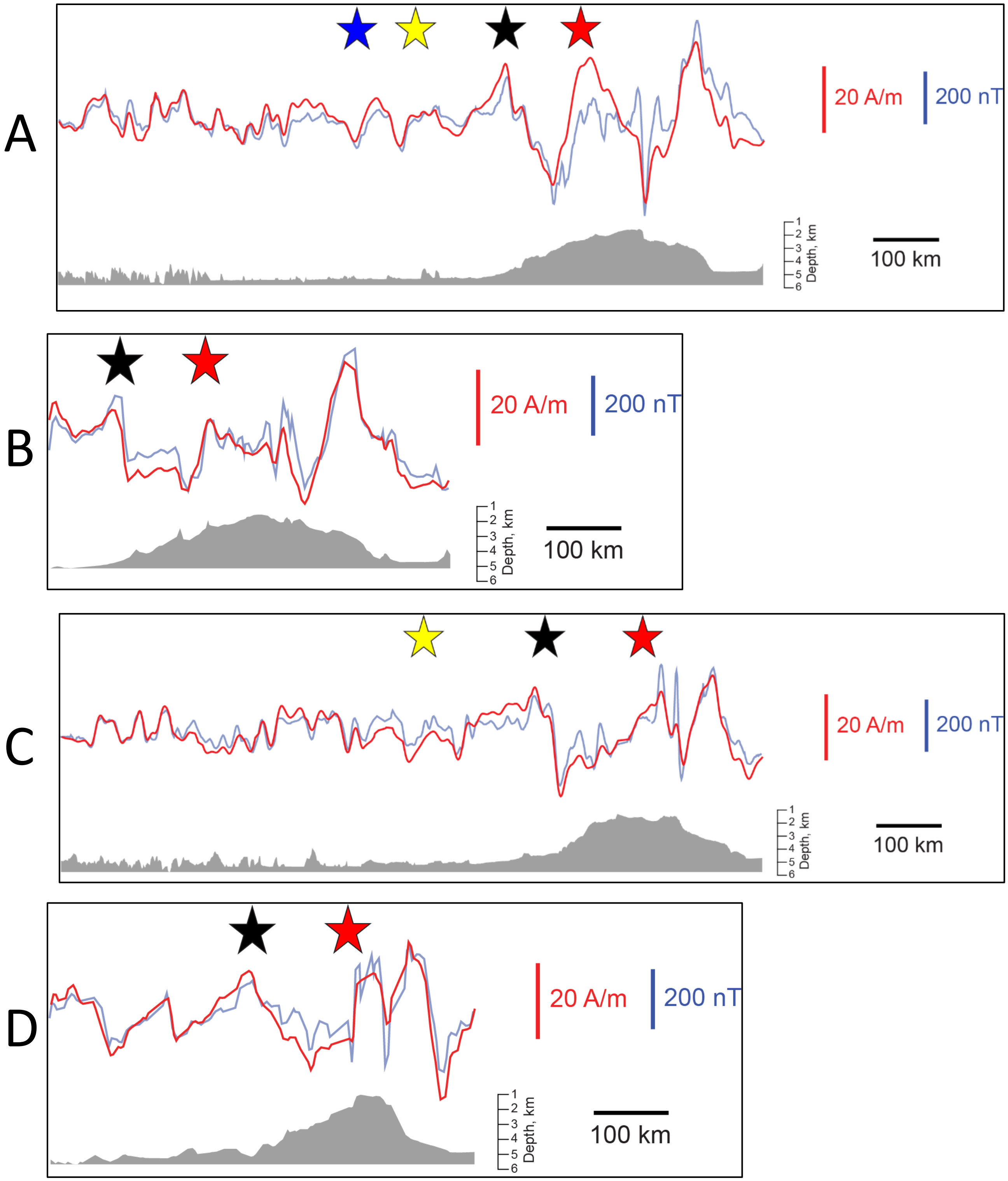

Figure 2.8 (continued)

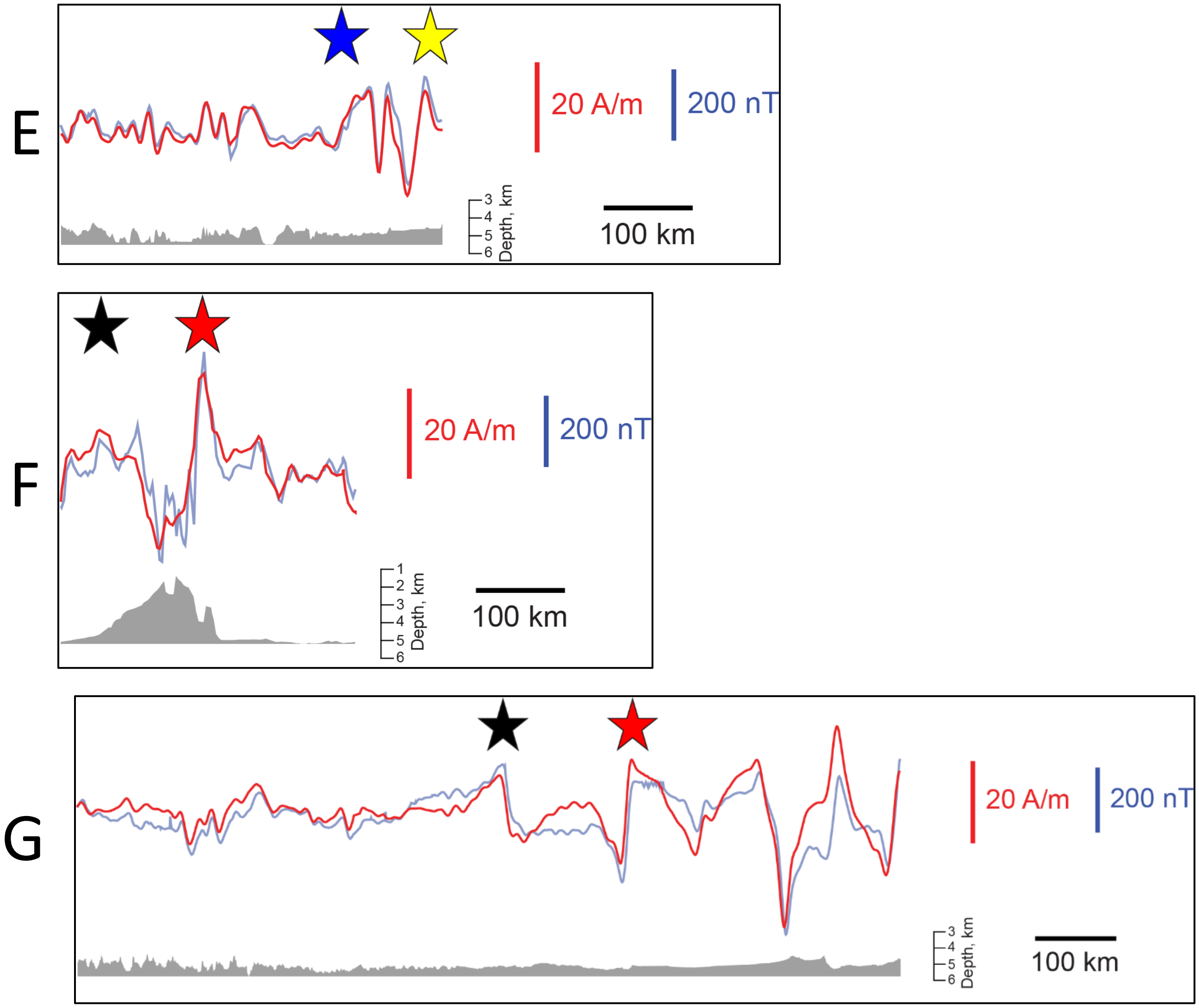

Figure 2.8 (continued)

2.3 Results

The Late Cretaceous reorganization in South Atlantic is restricted to the region between the Rio Grande- Florianopolis FZ (22°S) on the north and the 35.5°S FZ (Figure 2.1) on the south. When rotated to the conjugate plate, Late Cretaceous South American plate anomalies match in areas outside this zone but do not overlap in the region between these FZs (Figures 2.9 & 2.10).

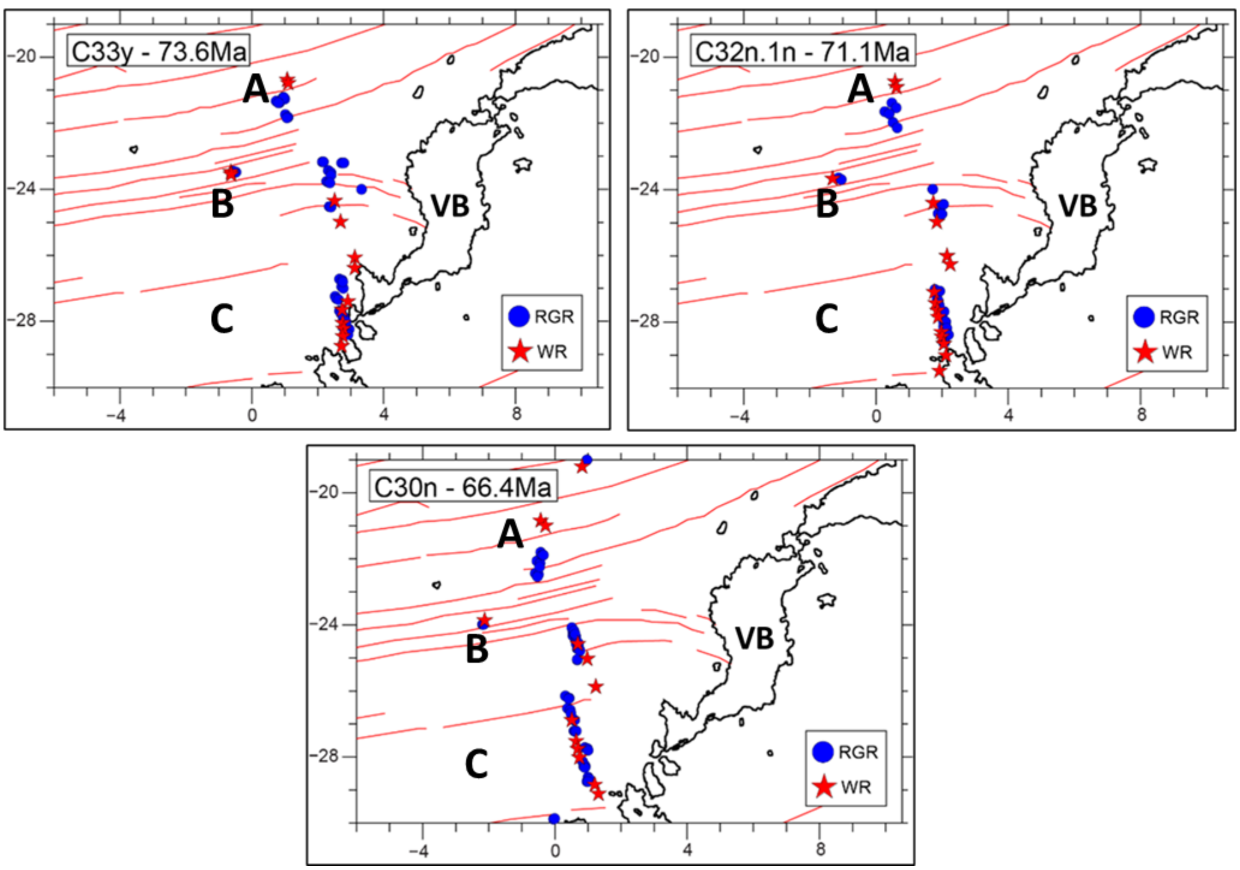

Figure 2.9 – Comparison of South American and African magnetic isochron picks near Valdivia Bank (VB) and Central WR. Picks on the African plate are shown by stars, whereas rotated anomaly picks from the conjugate South American plate are filled circles. Chron number and age are given in upper left corner of each plot. Black lines are 3 km bathymetry contours. Red lines represent FZs. The Matthews et al. (2016) global plate rotation model was used to rotate South American picks onto African plate.

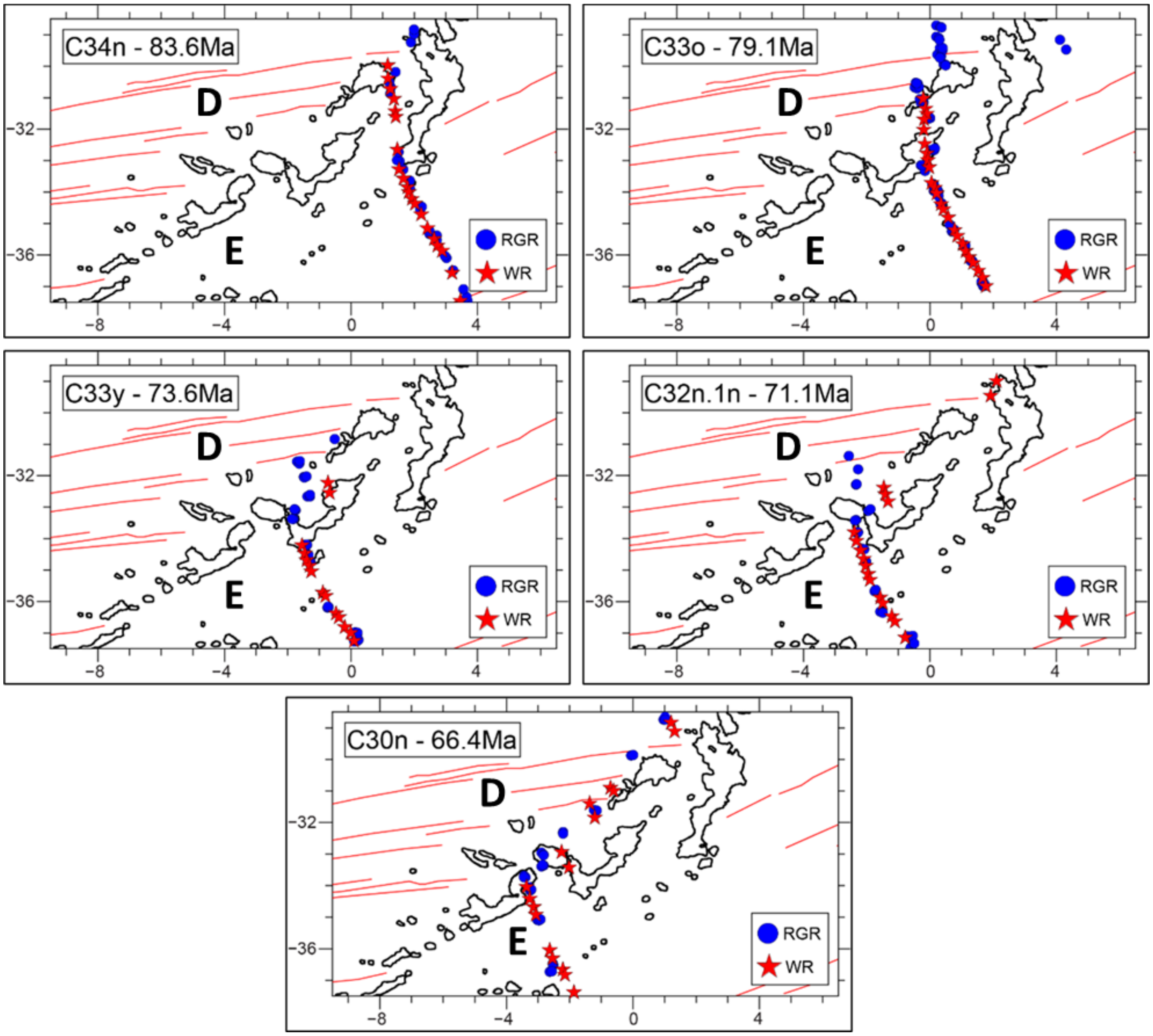

Figure 2.10 – Comparison of South American and African magnetic isochron picks near WR Guyot Province. Picks on the African plate are shown by stars, whereas rotated anomaly picks from the conjugate South American plate are filled circles. Chron number and age given in upper left corner of each plot. Black lines are 3 km bathymetry contours. Red lines represent FZs. The Matthews et al. (2016) global plate rotation model was used to rotate South American picks onto African plate.

The corridors to the north (A) and south (E) of the reorganization zone display similar, regular spreading histories and anomalies C25n-C34n can all be identified with locations consistent with opening models for the South Atlantic. A large aeromagnetic data set (cruise ANT XXIII-5; Jokat & Reents, 2017) significantly improved the coverage of anomalies C30n-C34n. Although these data were used in another anomaly study (Pérez-Díaz & Eagles, 2017), anomaly picks were poorly documented, so we made our own. Anomalies C32n.1n-C33o can easily be traced in EMAG2v3, which clearly shows the distinct wide negative band of anomaly C33r. This is preceded by wide (C33n) and narrow (C32n.1n) positive bands. All the anomalies in this corridor exhibit a trend of ~338°.

In Corridor A, at the edge of the reorganization zone, magnetic tracks are few, providing an incomplete picture. At ~24°S, a series of closely spaced FZ is present to the east of anomaly C30n, and the width of the anomalies younger than C30n is irregular and do not fit the expected model. To the east, these FZs end at a wide, well-defined negative anomaly at ~23°S, 2°E, which has been interpreted as anomaly C33r (between chrons C33o and C33y; Cande et al., 1988). In addition, most of the picks in this region cannot be recovered; we found only one magnetic track in the NCEI database. The southernmost FZs in this corridor diverge eastward, forming a series of curved FZs and implying complex spreading. In corridor E with normal spreading history, all anomalies are well defined and can be identified on multiple magnetic profiles (Figure 2.6).

Within the reorganization zone (Corridors B–D), the spreading is complex with uneven anomaly spacing and missing sequences. In Corridor B, anomalies C25n-C33y are consistent and regular and have been picked by previous studies, but anomalies C33o and C34n have not been mapped near Valdivia Bank. Anomalies C33y and C33o, the wide normal and reversed polarity zones following the normal polarity C34n anomaly, can be seen in the EMAG2v3 magnetic field map over and near western Valdivia Bank (Figure 2.4), where they were not previously mapped. The EMAG2v3 anomalies at this location are confirmed by magnetic profiles (Figures 2.5–2.7). Further, we confirmed these anomaly picks by magnetization modeling of key profiles over Valdivia Bank (Figure 2.8), which show that these anomalies are due to lateral polarity changes in the oceanic crust and not bathymetry effects. Anomaly C33r is a distinct broad negative anomaly that is present along the west edge of Valdivia Bank and we made anomaly C34n picks at its east side and anomaly C33y picks at its west side. Notably, the width of the anomaly C33r is less than that in Corridors A and D, implying that the entire anomaly is not preserved at this location. Moreover, its width decreases from north to south. Also, EMAG2v3 shows that at the southern end of Valdivia Bank, the negative C33r anomaly appears split into two with a small positive anomaly in between. Although we picked the edge of the western negative anomaly as chron C33o, this might not represent this reversal boundary owing to complex tectonics. The north side of this corridor is bounded by the aforementioned series of curved FZs that end near the western flank of Valdivia Bank. EMAG2v3 implies an age discontinuity across these curved FZs, with a negative anomaly to the north and a positive anomaly to the south. We were not able to find any magnetic profiles in NCEI database over the negative anomaly so this anomaly feature cannot be confirmed.

In Corridor C, though many magnetic profiles exist in this region, only anomalies C25n to C30n were identified by previous studies. Previously, anomaly C32n.1n has only been picked in the northern section of the corridor, but here we expand its identification into the southern part of the corridor (Figure 2.4). As predicted by the model, the wide positive peak east of chron C32n.1n has been interpreted as chron C33y. However, spreading appears complex near WR and the widths of anomalies C30n-C33y narrow southward. At 27–28°S, good correlations can be made in seafloor older than C33y and north of WR. Negative and positive anomaly bands east of chron C33y are interpreted as C33o and C34n respectively. Anomalies C33o-C34n form a V-shaped pattern narrowing southward. This narrowing implies that anomaly C34n changes from a N-S trend over Valdivia Bank in Corridor B but runs SW parallel to WR in corridor C. No correlations could be drawn to the east of anomaly C33y at 28–29°S, and there is an abrupt break in anomaly sequence east of WR. All of negative anomaly C33o and part of positive anomaly C34n seem to be missing at this latitude.

In Corridor D, the magnetic anomaly pattern is complex and cannot be easily traced. An age offset of ~15 Ma occurs across the northern edge of WR (the Tristan seamount trail)—younger to the north and older to the south. To the north of the Tristan trail, only anomalies C30n and younger have been identified. Though some correlations can be made, the anomalies in this area are poorly defined due to sparse data coverage and closely spaced FZs. South of the Tristan trail, there is a wedge-shaped pattern of magnetic anomalies where spreading is more regular, and anomalies correspond well with the normal spreading pattern. Anomalies C33y-C34n in this region are northward continuations of anomalies in Corridor E. These anomalies exhibit a trend of ~353°. The younger anomalies C30n-C32n.1n are offset from the corresponding anomalies in Corridor E by ~150 km. Anomalies C33o and C34n, which are two broad negative and positive anomalies, are well defined and can easily be traced in EMAG2v3. The width of the anomalies is consistent with normal spreading except for C32n.1n-C33o, which are about half the expected width. The large positive anomaly to the north of the Tristan seamount trail (~33°S, 1°E) has not been interpreted as it appears to be the anomaly of a large guyot, rather than representing spreading (Figure 2.6).

2.4 Discussion

A reorganization of the MAR occurred between RGR and WR, beginning prior to C34n (83.6 Ma) and ending before C30n (66.4 Ma). It likely involved a microplate (Figure 2.11), with a split MAR, and played a significant role in the development of WR morphology (Sager et al., 2021). The reorganization is poorly understood due to the sparse distribution of anomaly picks, large width of many anomalies, and time proximity to the Cretaceous Quiet Period. The current model (Seton et. al, 2012) that explains the geometry of these anomalies near WR was derived mainly from the South American plate and implies that an implausible ridge orientation oblique to spreading directions and spreading ridge faults near WR.

Updated magnetic anomalies support the hypothesis of a MAR reorganization in which a large transform offset north of WR during the Cretaceous Quiet Period evolved southward into multiple small transform offsets by anomaly C30n, resulting in the formation of several new transform faults south of ~30°S. Magnetic anomalies C34n, C33r, and C32n.1n display trends that follow WR bathymetry, supporting the idea that spreading ridge-hotspot interaction largely controlled WR morphology (Figure 2.12; O'Connor & Jokat, 2015a, 2015b). Updated anomalies show irregular geometry and spacing between isochrons C33y-C34n, with the width of anomalies C33r-C34n near WR narrowing southward. In this study, chrons C33o and C34n were picked near the western flank of Valdivia Bank, where previously no anomalies were picked. Studies (Cande et al., 1988; Huang et al., 2018; Nakanishi et al., 1999; Sager et al., 2019) have shown that large oceanic plateaus like Valdivia Bank can record coherent magnetic anomalies. These anomaly bands inside Valdivia Bank can be clearly seen in EMAG2v3, which shows two broad negative and positive anomaly bands over western Valdivia Bank. These anomalies infer that the age progression in Valdivia Bank is E-W trending and not N-S as predicted by various hotspot models (e.g., Doubrovine et al., 2012).

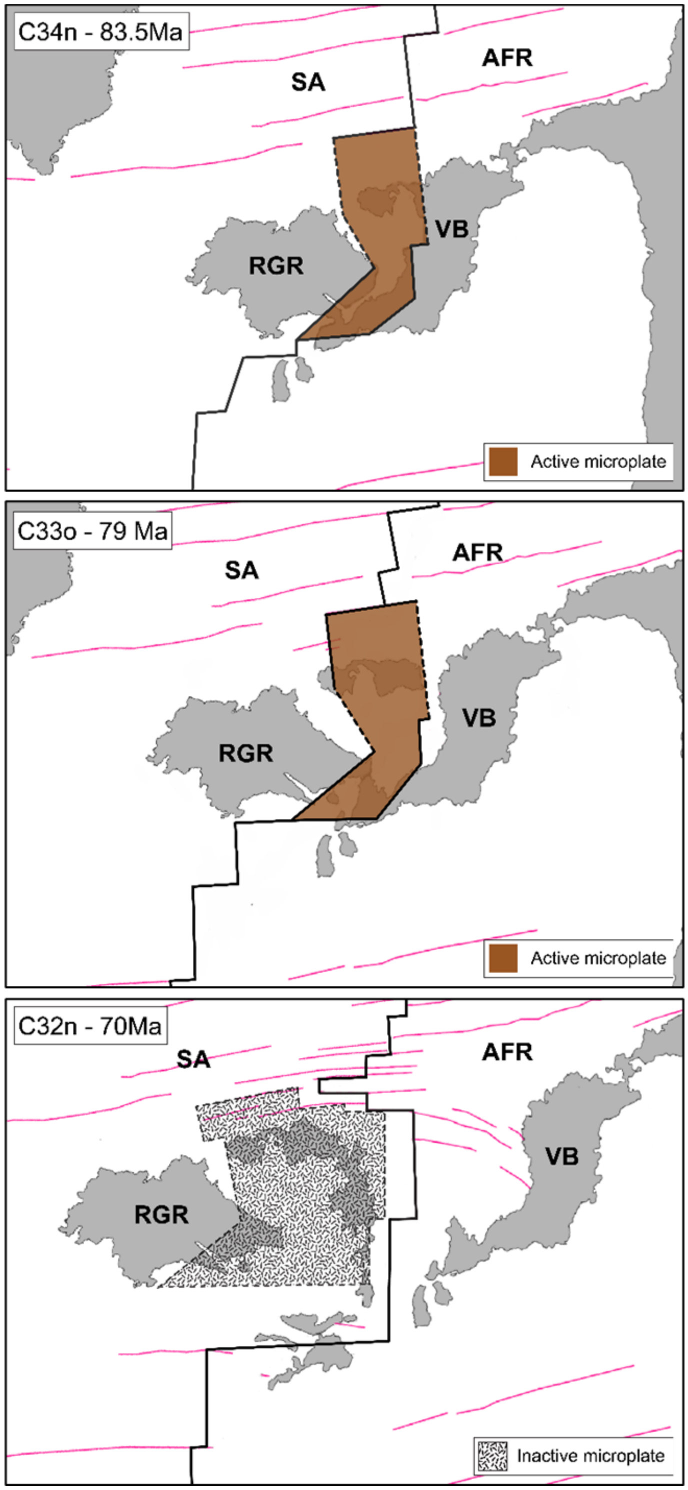

Figure 2.11 – Tectonic reconstruction sketch of Rio Grande Rise (RGR) and Valdivia Bank (VB) showing the potential boundary of the microplate active at (a) anomaly C34n (83.6 Ma) and (b) anomaly C33o (79.1 Ma); (c) the microplate that has been incorporated into the SA plate by anomaly C32n.1n (71.1 Ma). Black line represents spreading ridge geometry at that time; solid black represents ridge with good data control; dashed black represents poor data control and is a potential ridge geometry. SA = South American plate; AFR = African plate.

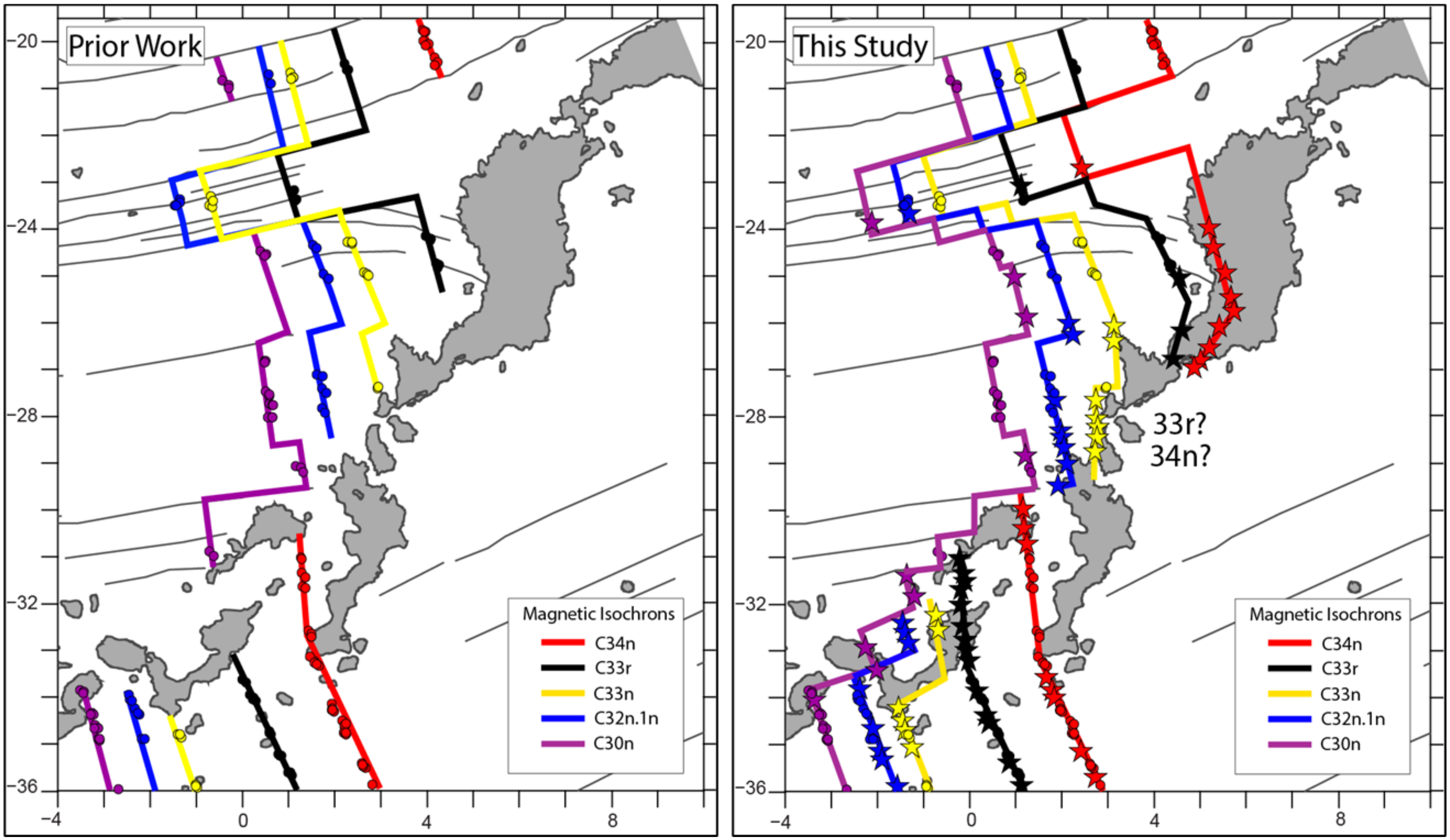

Figure 2.12 – Mid-Atlantic Ridge geometry of chrons C30n to C34n along Walvis Ridge based on magnetic picks from (left) Prior work (Cande et al., 1988; Seton et al., 2014) (right) this study. The magnetic picks from the prior work have been obtained from Global Seafloor Fabric and Magnetic Lineation Data Base Project (Seton et al., 2014). Gray polygons represent 3 km bathymetry contours of Walvis Ridge. Black lines represent FZs.

In spreading corridors B and C, chrons C34n through C33o from South America do not close with the same anomalies on Africa (Figure 2.9). This gap represents extra crust between the reconstructed chrons and implies that the chrons formed on different ridge boundary segments of a microplate (Sager et al., 2021; Figure 2.11). The microplate may have existed prior to C34n, but there are no magnetic anomalies of this age to confirm. The gap in rotated anomalies disappears by C32n.1n, indicating the end of the microplate, which was incorporated into the South American plate, between RGR Massif and ERGR, probably by an eastward ridge jump.

The southern FZs in Corridor A curve southward, diverge eastward, and end near Valdivia Bank. There is likely an age discontinuity across these FZs with a negative anomaly to the north and a positive anomaly to the south, implying an age offset across the curved FZ. The pattern of anomalies C32n.1n-C33n in Corridor C is perturbed, with anomalies narrowing southward, implying ridge propagation. In addition, identifications could not be made for chrons older than C33y in this corridor. Either the anomalies were not recognized, owing to poor track control and complex shapes, or they were transferred to the South American plate. Extra crust between anomalies C33r and C32n.1n exists on the South American plate east of RGR within the same spreading corridor. We think the missing anomalies were likely transferred to the South American plate in this area. Currently, public magnetic profiles do not exist over that region, so this hypothesis cannot be confirmed. There is an ~19° change in trend of chrons C33y-C34n from corridor D to corridor C. The anomalies in corridor C are not orthogonal to the South America-Africa spreading direction suggesting that either the ridge in this corridor was spreading obliquely or the ridge was a boundary with a microplate (i.e., not South America-Africa spreading).

Uneven and rapidly narrowing anomalies, curved FZs, age offsets, disturbed anomaly sequences, and rapid changes in anomaly trends are often found at microplate boundaries (e.g., Naar & Hey, 1991; Bird et al.,1998), where propagating rifts and ridge jumps progressively transfer crust from one plate to another, resulting in rapid anomaly width changes within short distances. Magnetic anomalies near WR indicate that the Late Cretaceous tectonic evolution of WR was complex, possibly involving propagating rifts and microplates. This finding implies that hotspot age progression models might be regionally more complex than published so far.

2.5 Conclusions

In this study, magnetic chrons C34n-C33y along WR that were not previously identified were mapped. Chron C34n was identified along the western flank of Valdivia Bank, a plateau feature, and new chron C33o picks were added in the area. New picks for chrons C33y and C32n.1n were added along the Central WR and chrons C34n-C32n.1n were identified in Guyot province, where only few picks previously existed.

The spacing and geometry of the magnetic isochrons between the Rio Grande -Florianopolis FZ on the north and 35°S FZ on the south and between chrons C34n-C30n is not regular, with varied spacing in different locations. In particular, chrons C34n and C33o reconstructed to close subsequent opening between South America and Africa do not align, leaving a gap of 100–200 km. This gap implies that the anomalies formed on different ridges with older lithosphere in between (possibly forming a microplate). By chron C32n.1n, reconstructed chrons match, indicating that spreading returned to normal and the microplate was incorporated into the South American plate possibly by eastward ridge jump.

Magnetic anomalies imply that the reorganization shifted the large, right-lateral MAR offset across WR from north to south, eventually forming a series of short-offset transforms at ~30–35°S by C30n. The width of anomaly C33o near WR is uneven and narrows southward, indicating that this anomaly may be incomplete owing to asymmetric accretion caused by ridge jumps or propagation. Anomalies C33o-C34n are truncated at the north edge of the Central WR, implying that these anomalies were transferred to the South American plate by a ridge jump, probably to the basin between RGR Massif and E-RGR.

Anomaly patterns imply that Valdivia Bank has an E-W trending age progression in contrast with the N-S age progression implied by the hotspot models. Previously, only one ridge jump associated with MAR reorganization near RGR-WR was identified in South Atlantic at anomaly C32n.1n, located to the south of RGR (Cande et al., 1988). Our anomaly pattern implies that additional ridge jumps occurred along WR before anomaly C30n, transferring lithosphere from African to South American plate. This study suggests that formation of the WR-RGR large igneous provinces was associated with a major reorganization of the MAR, resulting in complex tectonics that likely modified the morphology of these features.

2.6 Bibliography

Besse, J., & Courtillot, V. (2002). Apparent and true polar wander and the geometry of the geomagnetic field over the last 200 Myr. Journal of Geophysical Research: Solid Earth, 107(B11), EPM-6.

Bird, R. T., Naar, D. F., Larson, R. L., Searle, R. C., & Scotese, C. R. (1998). Plate tectonic reconstructions of the Juan Fernandez microplate: Transformation from internal shear to rigid rotation. Journal of Geophysical Research: Solid Earth, 103(B4), 7049–7067.

Cande, S. C., LaBrecque, J. L., & Haxby, W. F. (1988). Plate kinematics of the South Atlantic: Chron C34 to present. Journal of Geophysical Research: Solid Earth, 93(B11), 13479–13492.

Doubrovine, P. V., Steinberger, B., & Torsvik, T. H. (2012). Absolute plate motions in a reference frame defined by moving hotspots in the Pacific, Atlantic, and Indian oceans. Journal of Geophysical Research: Solid Earth, 117(B9).

Duncan, R. A. (1981). Hotspots in the southern oceans—an absolute frame of reference for motion of the Gondwana continents. Tectonophysics, 74(1–2), 29–42.

Huang, Y., Sager, W. W., Tominaga, M., Greene, J. A., Zhang, J., & Nakanishi, M. (2018). Magnetic anomaly map of Ori Massif and its implications for oceanic plateau formation. Earth and Planetary Science Letters, 501, 46–55.

Jokat, W., & Reents, S. (2017). Hotspot volcanism in the southern South Atlantic: Geophysical constraints on the evolution of the southern Walvis Ridge and the Discovery Seamounts. Tectonophysics, 716, 77–89.

Matthews, K. J., Maloney, K. T., Zahirovic, S., Williams, S. E., Seton, M., & Mueller, R. D. (2016). Global plate boundary evolution and kinematics since the late Paleozoic. Global and Planetary Change, 146, 226–250.

Meyer, B., Chulliat, A., & Saltus, R. (2017). Derivation and error analysis of the earth magnetic anomaly grid at 2 arc min resolution version 3 (EMAG2v3). Geochemistry, Geophysics, Geosystems, 18(12), 4522–4537.

Morgan, W. J. (1981). 13. Hotspot tracks and the opening of the Atlantic and Indian Oceans. The oceanic lithosphere, 7, 443.

Müller, R. D., Royer, J.-Y., & Lawver, L. A. (1993). Revised plate motions relative to the hotspots from combined Atlantic and Indian Ocean hotspot tracks. Geology, 21(3), 275–278.

Müller, R. D., Royer, J.-Y., Cande, S. C., Roest, W. R., & Maschenkov, S. (1999). New constraints on the Late Cretaceous/Tertiary plate tectonic evolution of the Caribbean. In Sedimentary basins of the world (Vol 4, bll 33–59). Elsevier.

Naar, D. F., & Hey, R. N. (1991). Tectonic evolution of the Easter microplate. Journal of Geophysical Research: Solid Earth, 96(B5), 7961–7993.

Nakanishi, M., Sager, W. W., & Klaus, A. (1999). Magnetic lineations within Shatsky Rise, northwest Pacific Ocean: Implications for hotspot-triple junction interaction and oceanic plateau formation. Journal of Geophysical Research: Solid Earth, 104(B4), 7539–7556.

O'Connor, J. M., & Duncan, R. A. (1990). Evolution of the Walvis Ridge-Rio Grande Rise hotspot system: Implications for African and South American plate motions over plumes. Journal of Geophysical Research: Solid Earth, 95(B11), 17475–17502.

O'Connor, J. M., & Jokat, W. (2015a). Age distribution of Ocean Drill sites across the Central Walvis Ridge indicates plate boundary control of plume volcanism in the South Atlantic. Earth and Planetary Science Letters, 424, 179–190.

O'Connor, J. M., & Jokat, W. (2015b). Tracking the Tristan-Gough mantle plume using discrete chains of intraplate volcanic centers buried in the Walvis Ridge. Geology, 43(8), 715–718.

O'Connor, J. M., & le Roex, A. P. (1992). South Atlantic hotspot-plume systems: 1. Distribution of volcanism in time and space. Earth and Planetary Science Letters, 113(3), 343–364.

Ogg, J. G. (2012). Geomagnetic polarity time scale. In F. M. Gradstein, J. G. Ogg, M. Schmitz, G. Ogg (Eds.), The geologic time scale 2012 (pp. 85–113).

Pérez-Díaz, L., & Eagles, G. (2014). Constraining South Atlantic growth with seafloor spreading data. Tectonics, 33(9), 1848–1873.

Pérez-Díaz, L., & Eagles, G. (2017). A new high-resolution seafloor age grid for the S outh A tlantic. Geochemistry, Geophysics, Geosystems, 18(1), 457–470.

Rohde, J. K., van den Bogaard, P., Hoernle, K., Hauff, F., & Werner, R. (2013). Evidence for an age progression along the Tristan-Gough volcanic track from new 40Ar/39Ar ages on phenocryst phases. Tectonophysics, 604, 60–71.

Sager, W. W., Huang, Y., Tominaga, M., Greene, J. A., Nakanishi, M., & Zhang, J. (2019). Oceanic plateau formation by seafloor spreading implied by Tamu Massif magnetic anomalies. Nature Geoscience, 12(8), 661–666.

Sager, W. W., Thoram, S., Engfer, D. W., Koppers, A. A. P., & Class, C. (2021). Late Cretaceous Ridge Reorganization, Microplate Formation, and the Evolution of the Rio Grande Rise-Walvis Ridge Hotspot Twins, South Atlantic Ocean. Geochemistry, Geophysics, Geosystems, 22(3), e2020GC009390.

Seton, M., Müller, R. D., Zahirovic, S., Gaina, C., Torsvik, T., Shephard, G. (2012). Global continental and ocean basin reconstructions since 200 Ma. Earth-Science Reviews, 113(3–4), 212–270.

Seton, M., Whittaker, J. M., Wessel, P., Müller, R. D., DeMets, C., Merkouriev, S. (2014). Community infrastructure and repository for marine magnetic identifications. Geochemistry, Geophysics, Geosystems, 15(4), 1629–1641.

Smith, W. H. F., & Sandwell, D. T. (1997). Global sea floor topography from satellite altimetry and ship depth soundings. Science, 277(5334), 1956–1962.

Thébault, E., Finlay, C. C., Beggan, C. D., Alken, P., Aubert, J., Barrois, O. (2015). International geomagnetic reference field: the 12th generation. Earth, Planets and Space, 67(1), 1–19.

Thoram, S., Sager, W. W., & Jokat, W. (2019). Implications of updated magnetic anomalies for the Late Cretaceous tectonic evolution of Walvis Ridge. Geophysical Research Letters, 46(16), 9474–9482.

Torsvik, T. H., Müller, R. D., Van der Voo, R., Steinberger, B., & Gaina, C. (2008). Global plate motion frames: toward a unified model. Reviews of geophysics, 46(3).

CHAPTER 3

NEW MAGNETIC ANOMALY MAPS AND TECTONIC RECONSTRUCTIONS OF WALVIS RIDGE AND RIO GRANDE RISE: IMPLICATIONS FOR LATE CRETACEOUS EVOLUTION OF HOTSPOT TWINS IN SOUTH ATLANTIC

3.1 Introduction

Oceanic plateaus have long been understood to have formed by massive eruptions due to an upwelling mantle (Coffin and Eldholm, 1994). These eruptions are commonly attributed to a rising deep mantle plume, originating at the core mantle boundary (e.g., Richards et al., 1989). Alternative hypotheses explain these enormous eruptions from fertile mantle melt escaping through the cracks in lithospheric plates (Anderson et al. 1992; Saunders 2005; Foulger, 2007). Nevertheless, the origin and subsequent tectonic evolution of oceanic plateau remains enigmatic due to their enormous size and remote locations in the ocean, often a result of sparse data coverage.

Hotspots and mid-ocean ridges (divergent plate boundaries) are major sources of magma eruptions at the Earth's surface, as evidenced by their high level of volcanic activity. Originally, a hotspot was thought to be a narrow, isolated, vertical thermal plume arising from deep inside the mantle that was unrelated to ridges (Wilson, 1965; Morgan, 1971). Some researchers have noted that oceanic plateaus commonly form at spreading ridges and triple junctions, suggesting a strong link between ridge and plume volcanism (Whittaker et al., 2015; Sager, 2007; Sager et al., 2019). Other researchers concluded that mantle plumes are thermochemical (i.e., have both chemical and thermal anomalies) and can be complex in morphology (Koppers et al., 2021).

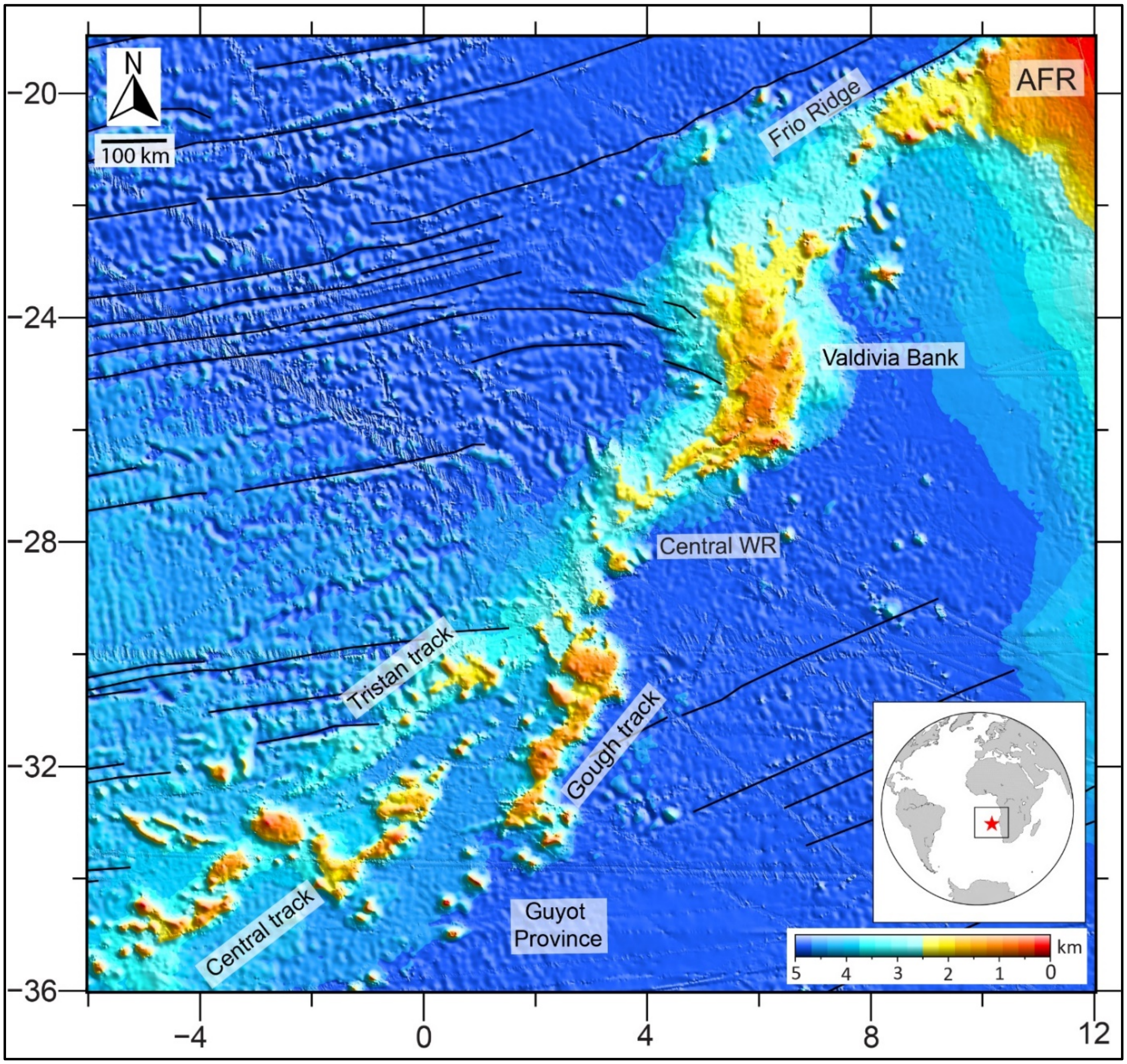

Figure 3.1 – Walvis Ridge bathymetry and feature names. Black lines are fracture zones (Sager et al., 2021). Background is SRTM15+ predicted bathymetry (Tozer et al., 2019). Inset shows Walvis Ridge location relative to Africa. AFR=Africa; WR = Walvis Ridge.

Walvis Ridge (WR) and Rio Grande Rise (RGR) are two large oceanic plateaus in South Atlantic located on the conjugate African and American plates (Figures 3.1, 3.2). They are considered to have simultaneously formed due to eruptions from the Tristan-Gough hotspot, centered at the Mid-Atlantic Ridge (MAR) (O'Connor and Duncan, 1990). Despite being formed under similar tectonic conditions, WR and RGR have contrasting morphologies. WR is a quasi-linear submarine ridge (Figure 3.1) while RGR consists of two subrounded plateaus (RGR Massif and SE-RGR) and a spreading-axis parallel ridge (E-RGR) (Figure 3.2). Any model that attempts to explain their evolution must account for the difference in their structures. Recent studies have suggested that a major MAR reorganization in the South Atlantic occurred during the Late Cretaceous time, between magnetic anomalies (isochrons) C34-C30 (83.6 Ma – 66.4 Ma; Ogg, 2012), involving hotspot-ridge interactions, propagating rifts and microplates, complicating the tectonics between WR and RGR (O'Connor & Jokat, 2015a; Thoram et al., 2019; Sager et al., 2021).

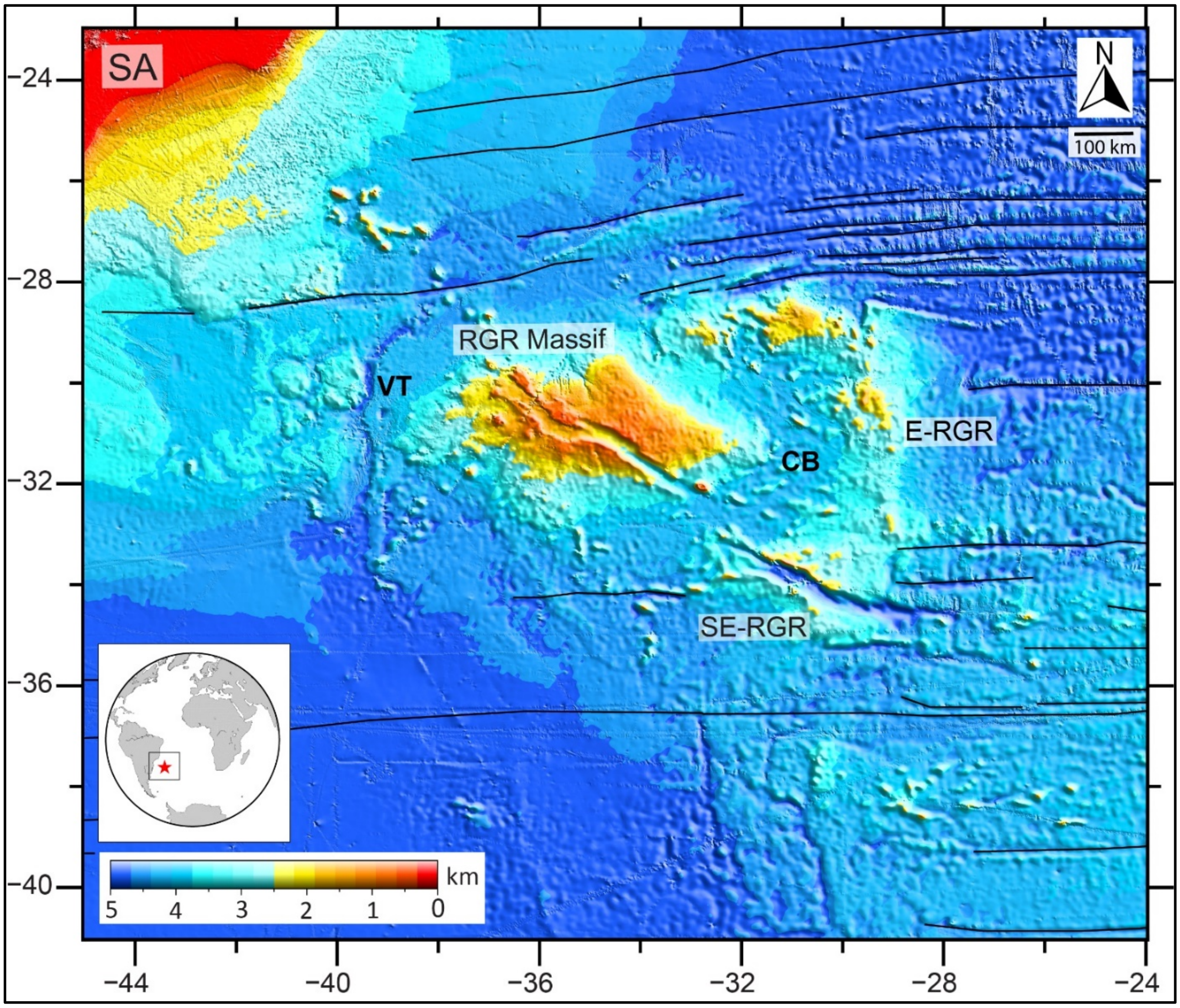

Figure 3.2 – Rio Grande Rise bathymetry and feature names. Black lines are fracture zones (Sager et al., 2021). Background is SRTM15+ predicted bathymetry (Tozer et al., 2019). Inset shows Rio Grande Rise location relative to South America. SA=South America; RGR = Rio Grande Rise; E-RGR= East Rio Grande Rise; SE-RGR= Southeast Rio Grande Rise; VT=Vema Trough; CB=Centaurus Basin.

Magnetic anomaly patterns play an essential role in determining the age of the oceanic crust and in reconstructing the tectonic history of oceanic plateaus (Heirtzler et al., 1968; Gee and Kent, 2007; Sager et al., 2019). Unfortunately, many oceanic plateaus were formed during Cretaceous Normal Superchron (CNS), a ~35 Myr period of no magnetic reversals, which lasted from approximately 121 to 83 Ma (Ogg, 2012). Seafloor formed during this period is characterized as having no distinct correlatable patterns of magnetic anomalies, making it difficult to use magnetic lineations to study tectonic evolution. Fortunately, WR and RGR formed at the end of CNS, when Earth's magnetic field experienced reversals again, making it possible to identify the Late Cretaceous chrons (C34-C33) along these features and study their evolution and understand the hotspot-ridge interactions shaping them.

Because the ship tracklines used to generate that map were not specified, the current global magnetic grid for the South Atlantic (EMAG2v3; Meyer et al., 2017) cannot be utilized as a basis for the magnetic maps. Furthermore, reconstructions of WR and RGR are based on decades-old anomaly identifications from Cande et al. (1988), with a few later additions (Müller et al., 1999; Nankivell, 1997; Seton et al., 2014; Pérez-Díaz et al., 2017; Bird and Hall, 2010; see Chapter 2). Geophysical surveys in the South Atlantic have been rare and only a few studies have added more anomaly picks in the area (Bird and Hall, 2016; Hall et al., 2018; Pérez-Díaz and Eagles, 2017; Thoram et al., 2019) since the work of Cande et al. (1988).

There are huge gaps in anomalies published in Global Seafloor Fabric and Magnetic Lineations database (GSFML; Seton et al., 2014). Late Cretaceous chrons C34-C33 are not consistently picked over WR and RGR. West of WR, where C34 has not been previously recognized, chrons 33r and 33n are each identified by only a small number of anomaly picks. In Chapter 2, we analyzed the magnetic tracks over this region and identified these missing chrons.

Furthermore, the distance between chrons C34 and C30 varies east of RGR Massif, implying complex ridge behavior. In this interval, isochrons have not been mapped in a large area east of RGR Massif, probably because Cretaceous crust from the Africa plate was abandoned on the South America plate during the C34-C30 reorganization (Thoram et al., 2019; Sager et al., 2021). The reconstructions based on these chrons are not well constrained and may not reflect the actual tectonic evolution of WR and RGR. The studies (Thoram et al., 2019; Sager et al., 2021) also suggested that the anomalous Cretaceous crust was probably an active microplate that got incorporated into the South American plate, complicating the tectonics of WR and RGR.

In order to decipher the complex tectonic history and test the microplate hypothesis, we conducted large scale magnetic surveys over WR (cruises TN373, TN374; 2019) collecting ~15,000 line km of data (Figure 3.3). Over RGR, we acquired some magnetic data during a dredging cruise (NBP1808; 2018). Additionally, we collaborated with German institutions to collect more magnetic data over WR (cruise ANT XXIII-5; 2017) and RGR (cruise MSM82; 2019). Using the newly acquired data in conjunction with available magnetic data in the region (Tables 3.1, 3.2), we generated magnetic anomaly maps for WR and RGR. Unlike previous studies which relied on manual picking of magnetic anomalies, which can be subjective and difficult for sparse datasets and often pick only positive anomalies, we opted to generate magnetic anomaly maps (Figures 3.10, 3.11) which are useful to visualize and identify complex anomaly patterns in 2D. Magnetic anomaly profiles were plotted over these generated maps to guide our interpretations. Reconstructions were made by rotating anomalies and comparing widths and variations of anomaly bands on both sides of the Atlantic and comparing to expected widths based on the opening rate.

3.2 Geologic Setting

WR and RGR are examples of oceanic plateaus formed by ridge-centered hotspot volcanism (Morgan, 1981; O'Connor and Duncan, 1990). WR is a large submarine ridge extending from the Namibian continental margin to the islands of Tristan and Gough, whereas RGR is a sub-rounded plateau located east of Brazil (Figures 3.1, 3.2). Although formed by the same ridge-centered hotspot magmatism, WR and RGR exhibit different morphologies. WR is a linear ridge with varying morphology over its length. It consists of a narrow linear ridge (Frio Ridge), an oceanic plateau (Valdivia Bank), and three linear seamount chains (Figure 3.1), whereas RGR consists of several sub-rounded plateaus and a spreading-perpendicular ridge (Figure 3.2). A distinct SE-NW trending rift with unknown origin, Cruzeiro do Sul Rift, cuts across the center of RGR Massif and SE-RGR.

During the Late Cretaceous, while the Tristan-Gough hotspot was at or near the Mid-Atlantic Ridge, volcanism erupted on the African and South American plates forming older parts of WR and RGR respectively. At around 70 Ma, the spreading axis migrated west away from the hotspot beneath the African plate. Around this time, WR transitioned from forming short spreading center-parallel ridges to three linear seamount chains while volcanism on the South American plate began to dwindle, forming a Zapiola seamount complex south of RGR. Around 35 Ma, volcanism ceased over the South American plate, ending the formation of Zapiola seamount complex. The hotspot is currently located under the Tristan and Gough volcanic islands ~550 km east of the spreading axis (O'Connor & Duncan, 1990).

Various studies have attempted to explain the differences in structure, but none completely explain all observations. According to O'Connor and Jokat (2015a; b), the interaction of the Tristan-Gough hotspot with the MAR, caused the morphological changes along WR. They propose that during the Late Cretaceous, plume volcanism erupted along an SW-NE trending segment of the MAR forming Valdivia Bank and spreading-perpendicular ridges to its immediate SW. The plume later erupted at the MAR as the latter restructured into N-S trending segments, to construct WR down to the trident (the point at which the ridge splits into three seamount chains). When the plume drifted away from the MAR under the African plate, WR transitioned into three distinct seamount chains, forming the Tristan chain at the MAR and the Central and Gough chains in an intraplate setting (Figure 3.1)

While there is no clear explanation for the distinct morphology of the RGR, its complex structure appears to have formed by hotspot interacting with the MAR with varying volumes of eruption, with larger eruptions forming RGR Massif and smaller eruptions forming other edifices (O'Connor & Duncan, 1990; O'Connor & Jokat, 2015a; Galvo & de Castro, 2017). The Cruzeiro do Sul Rift, that cuts across RGR Massif and SE-RGR is thought to be due to an Eocene rifting event that occurred in a mid-plate setting (Gamboa and Rabinowitz, 1984; Mohriak et al., 2010), but there appears to be no obvious tectonic event that caused it (Figure 3.2).

During the Late Cretaceous, a major plate reorganization occurred in the South Atlantic, resulting in change in spreading direction as indicated by the change in azimuth of the fracture zones. Sager et al. (2021) noted this reorganization occurred as ~600 km long-offset right-lateral transform fault (at C34) north of WR, moved southward and split into multiple, lesser-offset transforms (at C30). Studies (Sager et al., 2021; see Chapter 2) suggested that a microplate formed during this reorganization, which was eventually captured by the South American plate, and is part of the anomalous extra crust located east of RGR Massif. However, the detailed evolution is still not well documented due to missing anomaly sequences and a poorly constrained Late Cretaceous tectonic reconstruction model for WR and RGR. Through the newly generated magnetic anomaly maps, this study aims at identifying the missing anomaly sequences and using them to study the detailed Late Cretaceous tectonic evolution of WR and RGR.

3.3 Data and Methods

3.3.1 Magnetic Data

A total of 105 magnetic cruises, 52 over WR and 53 over RGR, spanning over 60 years (1959-2019), have been used to compile the magnetic anomaly maps for this study (Figures 3.3, 3.4; Tables 3.1, 3.2). The combined dataset accounts to ~800,000 data points along ~332,757 km of track length. These data have been acquired from various sources. 96 of the tracks were acquired from the National Center for Environmental Information (NCEI) database, 2 tracks from the Japan Agency for Marine-Earth Science and Technology (JAMSTEC) database and 4 tracks acquired from German scientists (Tables 3.1, 3.2). The remaining 3 surveys were funded by the NSF (National Science Foundation) to collect other magnetic data from the study area. We recently collected large amounts of magnetic data onboard R/V *Thomas G. Thompson* during cruises TN373 and TN374, which collected ~3 x 10^6 data points in a grid of 25 transects across eastern WR. Magnetic data were also collected over RGR, onboard R/V *Nathaniel B. Palmer* (cruise NBP1808 during 2018) which collected ~4 x 10^5 magnetic readings.

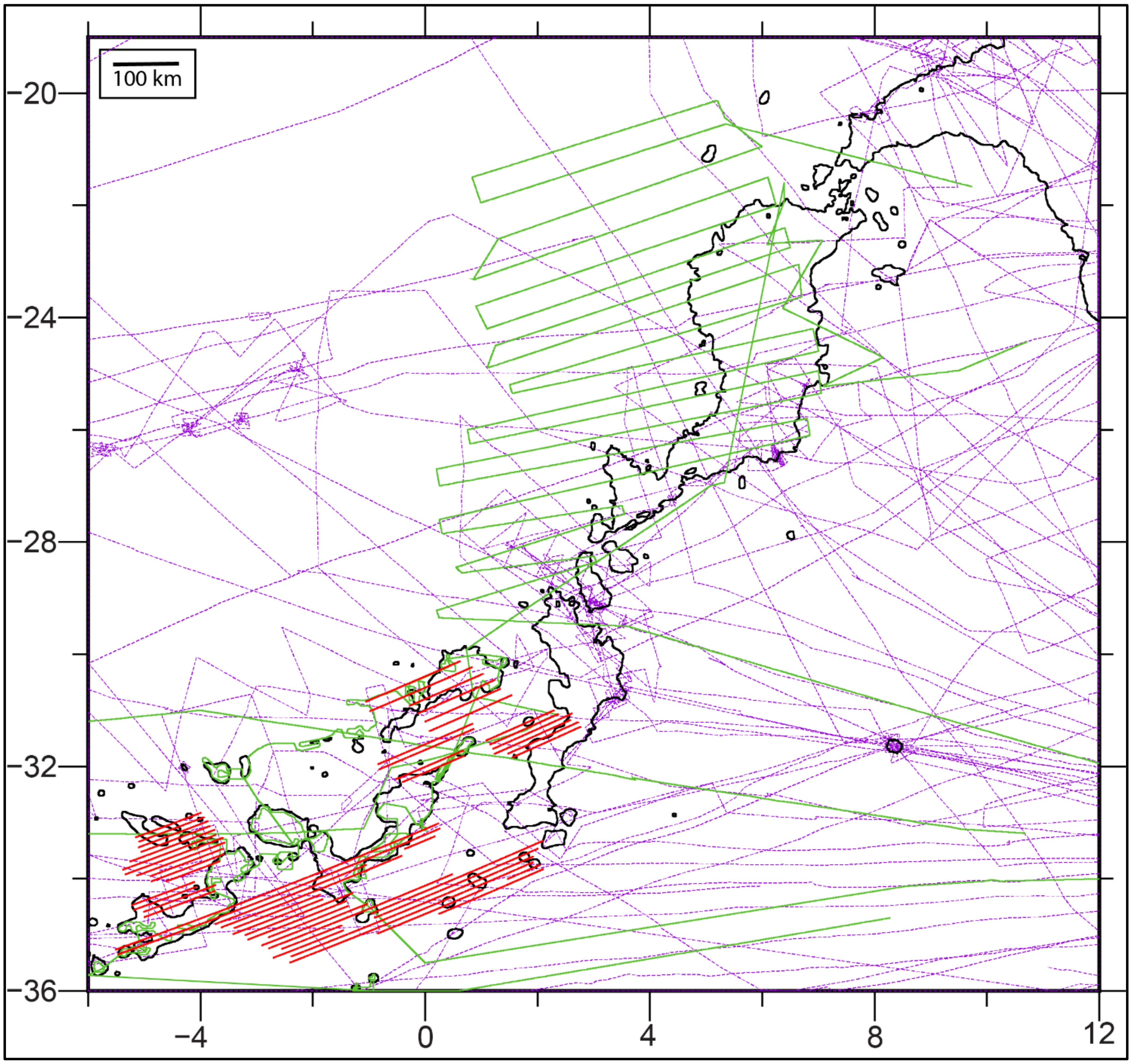

Figure 3.3 – Magnetic ship tracks over WR. Green solid lines show tracks of new cruises TN374, TN373. Red solid lines show the tracks of German aeromagnetic survey (Jokat & Reents, 2017). Dashed purple lines denote older magnetic cruises from the National Centers for Environmental Information (NCEI) repository. Black solid lines show the 3000 m bathymetry contour.

Table 3.1 – Magnetic Surveys over Walvis Ridge

Cruise ID	Year	Ship	Source Institute	Navi¶
V1604	1959	*Vema*	Lamont-Doherty Earth Observatory	U
V1809	1962	*Vema*	Lamont-Doherty Earth Observatory	C
RC0801	1963	*Robert D. Conrad*	Lamont-Doherty Earth Observatory	U
V1912	1963	*Vema*	Lamont-Doherty Earth Observatory	C
V2011	1964	*Vema*	Lamont-Doherty Earth Observatory	C
V2206	1966	*Vema*	Lamont-Doherty Earth Observatory	C
V2412	1967	*Vema*	Lamont-Doherty Earth Observatory	D/C
CIRC08AR	1968	*Argo*	Scripps Institute of Oceanography	D
RC1214	1969	*Robert D. Conrad*	Lamont-Doherty Earth Observatory	D
CH099L04	1970	*Chain*	Woods Hole Oceanographic Institute	U
RC1313	1970	*Robert D. Conrad*	Lamont-Doherty Earth Observatory	D
71003311	1971	*Jean Charcot*	France CNEXO	U
71003411	1971	*Jean Charcot*	France CNEXO	U
V2906	1972	*Vema*	Lamont-Doherty Earth Observatory	D/C
CH115L02	1973	*Chain*	Woods Hole Oceanographic Institute	D
RC1703	1973	*Robert D. Conrad*	Lamont-Doherty Earth Observatory	D
CH115L05	1974	*Chain*	Woods Hole Oceanographic Institute	D
DSDP39GC	1974	*Glomar Challenger*	Scripps Institute of Oceanography	D
DSDP40GC	1974	*Glomar Challenger*	Scripps Institute of Oceanography	D
A2093L02	1975	*Atlantis II*	Woods Hole Oceanographic Institute	D
A2093L03	1975	*Atlantis II*	Woods Hole Oceanographic Institute	D
78009911	1978	*Jean Charcot*	France IFREMER	D
AG04	1978	*Agulhas*	S Africa Data Center Ocean	U
TD377	1978	*Thomas B. Davie*	S Africa University of Cape Town	D
79000211	1979	*Jean Charcot*	France IFREMER	D
79000212	1979	*Jean Charcot*	France IFREMER	D
AG08	1979	*Agulhas*	S Africa Data Center Ocean	U
FM0102	1979	*Fred H. Moore*	University of Texas	D
FM0103	1979	*Fred H. Moore*	University of Texas	D
FM0104	1979	*Fred H. Moore*	University of Texas	D
FM0105	1979	*Fred H. Moore*	University of Texas	D
TD388	1979	*Thomas B. Davie*	S Africa University of Cape Town	D
TD397	1979	*Thomas B. Davie*	S Africa University of Cape Town	D
DSDP73GC	1980	*Glomar Challenger*	Scripps Institute of Oceanography	D
DSDP74GC	1980	*Glomar Challenger*	Scripps Institute of Oceanography	D
DSDP75GC	1980	*Glomar Challenger*	Scripps Institute of Oceanography	D
V3620	1981	*Vema*	Lamont-Doherty Earth Observatory	U
MRTN10WT	1984	*Thomas Washington*	Scripps Institute of Oceanography	D
MRTN13WT	1985	*Thomas Washington*	Scripps Institute of Oceanography	D
RC2711	1986	*Robert D. Conrad*	Lamont-Doherty Earth Observatory	G/D
ODP208JR‡	2003	*JOIDES Resolution*	ODP/Texas A and M	G
MV1203‡	2012	*Melville*	Scripps Institute of Oceanography	G
ANT XXIII-5‡	2014	*Polarstern*	Alfred Wegener Institute	G
TN373‡	2019	*Thomas G. Thompson*	Univ. of Washington	G
TN374‡	2019	*Thomas G. Thompson*	Univ. of Washington	G

¶Navigation codes: Celest=celestial; Loran=Long Range (radio) Navigation; C=Celestial navigation (sextant); D=Doppler satellite (NNSS); G=Global Positioning System (GPS satellite); U=Unknown. ‡Data not used in previous compilations (Cande et al., 1988; Bryan et al., 2017).

Table 3.2 – Magnetic Surveys over Rio Grande Rise

Cruise ID	Year	Ship	Source Institute	Navi¶
V1611	1960	*Vema*	Lamont-Doherty Earth Observatory	C
V1712	1961	*Vema*	Lamont-Doherty Earth Observatory	C
V1808	1962	*Vema*	Lamont-Doherty Earth Observatory	C
V1809	1962	*Vema*	Lamont-Doherty Earth Observatory	C
V2011	1964	*Vema*	Lamont-Doherty Earth Observatory	C
OPR470	1966	*Oceanographer*	NOAA	D
RC1102	1966	*Robert D. Conrad*	Lamont-Doherty Earth Observatory	D
V2203	1966	*Vema*	Lamont-Doherty Earth Observatory	C
V2412	1967	*Vema*	Lamont-Doherty Earth Observatory	D/C
V2413	1967	*Vema*	Lamont-Doherty Earth Observatory	D/C
RC1213	1968	*Robert D. Conrad*	Lamont-Doherty Earth Observatory	D
V2604	1968	*Vema*	Lamont-Doherty Earth Observatory	D/C
V2605	1968	*Vema*	Lamont-Doherty Earth Observatory	D/C
V2606	1969	*Vema*	Lamont-Doherty Earth Observatory	D/C
CATO05MV	1972	*Melville*	Scripps Institute of Oceanography	D
CATO06MV	1972	*Melville*	Scripps Institute of Oceanography	D
RC1507	1972	*Robert D. Conrad*	Lamont-Doherty Earth Observatory	D
RC1508	1972	*Robert D. Conrad*	Lamont-Doherty Earth Observatory	D
RC1605	1972	*Robert D. Conrad*	Lamont-Doherty Earth Observatory	D
73003011	1973	*Jean Charcot*	France CNEXO	U
73003021	1973	*Jean Charcot*	France CNEXO	U
73003111	1973	*Jean Charcot*	France CNEXO	U
RC1610	1973	*Robert D. Conrad*	Lamont-Doherty Earth Observatory	D
CH115L05	1974	*Chain*	Woods Hole Oceanographic Institute	D
CH115L06	1974	*Chain*	Woods Hole Oceanographic Institute	D
DSDP36GC	1974	*Glomar Challenger*	Scripps Institute of Oceanography	D
DSDP39GC	1974	*Glomar Challenger*	Scripps Institute of Oceanography	D
V3101	1974	*Vema*	Lamont-Doherty Earth Observatory	D/C
V3104	1974	*Vema*	Lamont-Doherty Earth Observatory	D/C
V3105	1974	*Vema*	Lamont-Doherty Earth Observatory	D/C
I1678	1978	*Islas Orcadas*	Lamont-Doherty Earth Observatory	D
INMD12MV	1978	*Melville*	Scripps Institute of Oceanography	D
RC2105	1978	*Robert D. Conrad*	Lamont-Doherty Earth Observatory	D
FM0105	1979	*Fred H. Moore*	Texas, U Inst Geophysics	D/R
FM0106	1979	*Fred H. Moore*	Texas, U Inst Geophysics	D
DSDP71GC	1980	*Glomar Challenger*	Scripps Institute of Oceanography	D
DSDP72GC	1980	*Glomar Challenger*	Scripps Institute of Oceanography	D
DSDP73GC	1980	*Glomar Challenger*	Scripps Institute of Oceanography	D
MRTN10WT	1984	*Thomas Washington*	Scripps Institute of Oceanography	D
NRL	Early	*P-3 survey aircraft*	US Naval Oceanographic Office	G

aeromagnetic‡ survey	1980s*			
RC2711	1986	*Robert D. Conrad*	Lamont-Doherty Earth Observatory	G/D
RC2802	1987	*Robert D. Conrad*	Lamont-Doherty Earth Observatory	G/D
EW9011	1990	*Maurice Ewing*	Lamont-Doherty Earth Observatory	G/D
PLUM04WT	1990	*Thomas Washington*	Scripps Institute of Oceanography	G
PLUM05WT	1990	*Thomas Washington*	Scripps Institute of Oceanography	G
YK13‡	2013	*Yokosuka*	The University of Tokyo	G
NBP1808‡	2018	*Nathaniel B. Palmer*	United States Antarctic Program	G
TN373‡	2019	*Thomas G. Thompson*	University of Washington	G
MSM82‡	2020	*Maria S. Merian*	University of Hamburg	G

¶Navigation codes: Celest=celestial; Loran=Long Range (radio) Navigation; C=Celestial navigation (sextant); D=Doppler satellite (NNSS); G=Global Positioning System (GPS satellite); U=Unknown. ‡Data not used in previous compilation (Cande et al., 1988; Bryan et al., 2017).

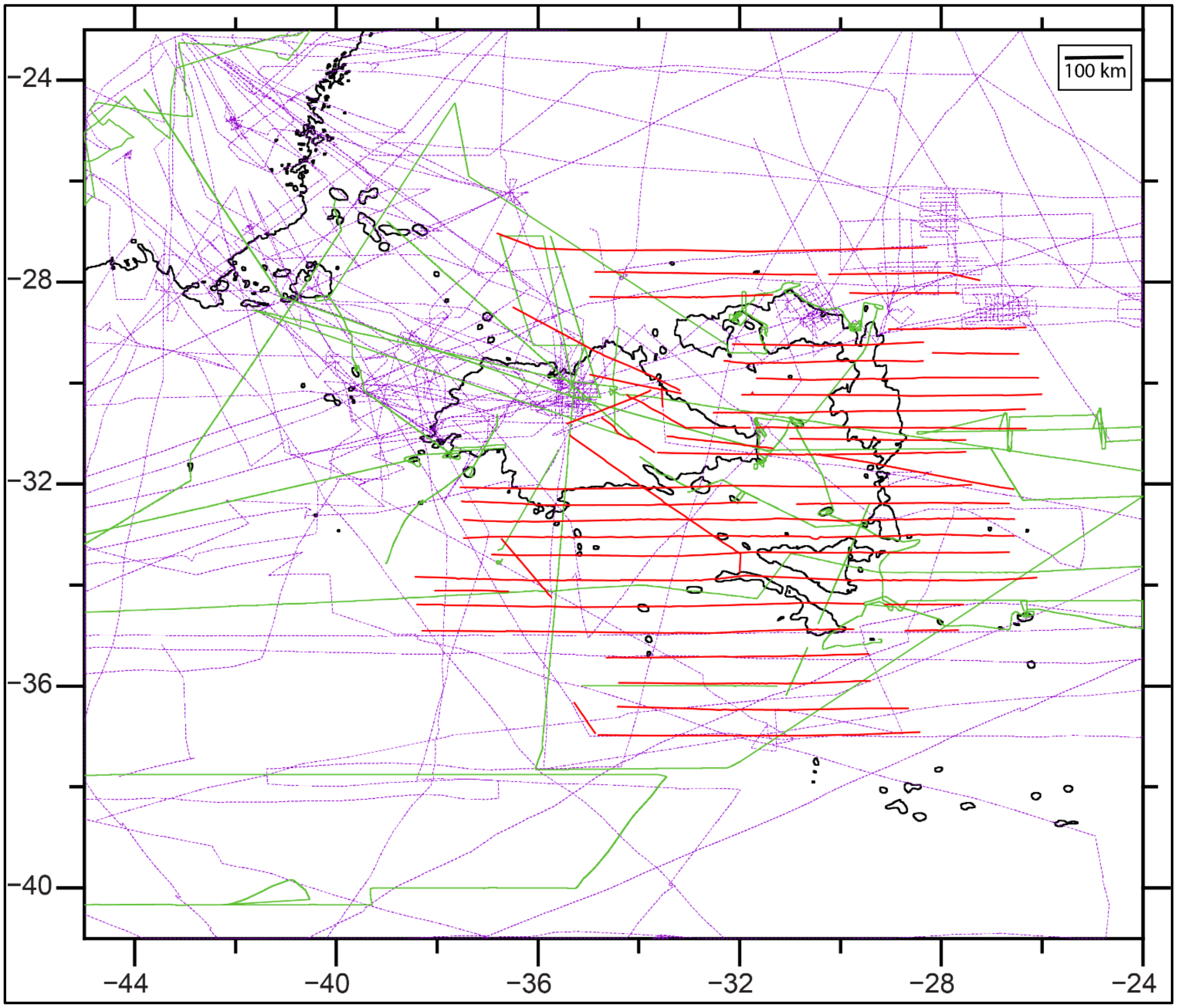

Figure 3.4 – Magnetic ship tracks over RGR. Green solid lines show tracks of new magnetic tracks collected since Cande et al., (1988). Red solid lines show the tracks of Naval Research Laboratory (NRL) aeromagnetic survey. Dashed purple lines denote older magnetic cruises from the NCEI repository. Black solid lines show the 3000 m bathymetry contour.

The majority of the magnetic data were acquired from marine platforms except for 2 surveys, which were collected from low altitude (100 m) aeromagnetic surveys. Aeromagnetic data were collected over WR by helicopter during cruise ANT XXIII-5 (Jokat & Reents, 2017), during which collected 15,417 line km of data were obtained near the trident. An aeromagnetic survey was conducted over RGR by the Naval Research Laboratory (NRL) in the early 1980s. This survey gathered over 43,000 line km of aeromagnetic data with flight line spacing from 30 km to 50 km. Unfortunately, these data were neither published or archived, but we were able to obtain a magnetic anomaly (Figure 3.5; John L. LaBrecque, personal communication, 2018). We used Didger software to digitize the magnetic anomaly profiles from the plot by sampling the amplitude of the profile every 2' of longitude (Figure 3.6). We calibrated the anomaly amplitudes by comparing these data where the lines cross available digital marine magnetic data. However, this process cannot fully recover the original data due to limitations in accurately digitizing the location of the magnetic value and these data should therefore be interpreted with caution. Because of this uncertainty, we made two versions of the magnetic anomalies maps for RGR, one with only marine magnetic data and the other integrating the recovered NRL aeromagnetic data.

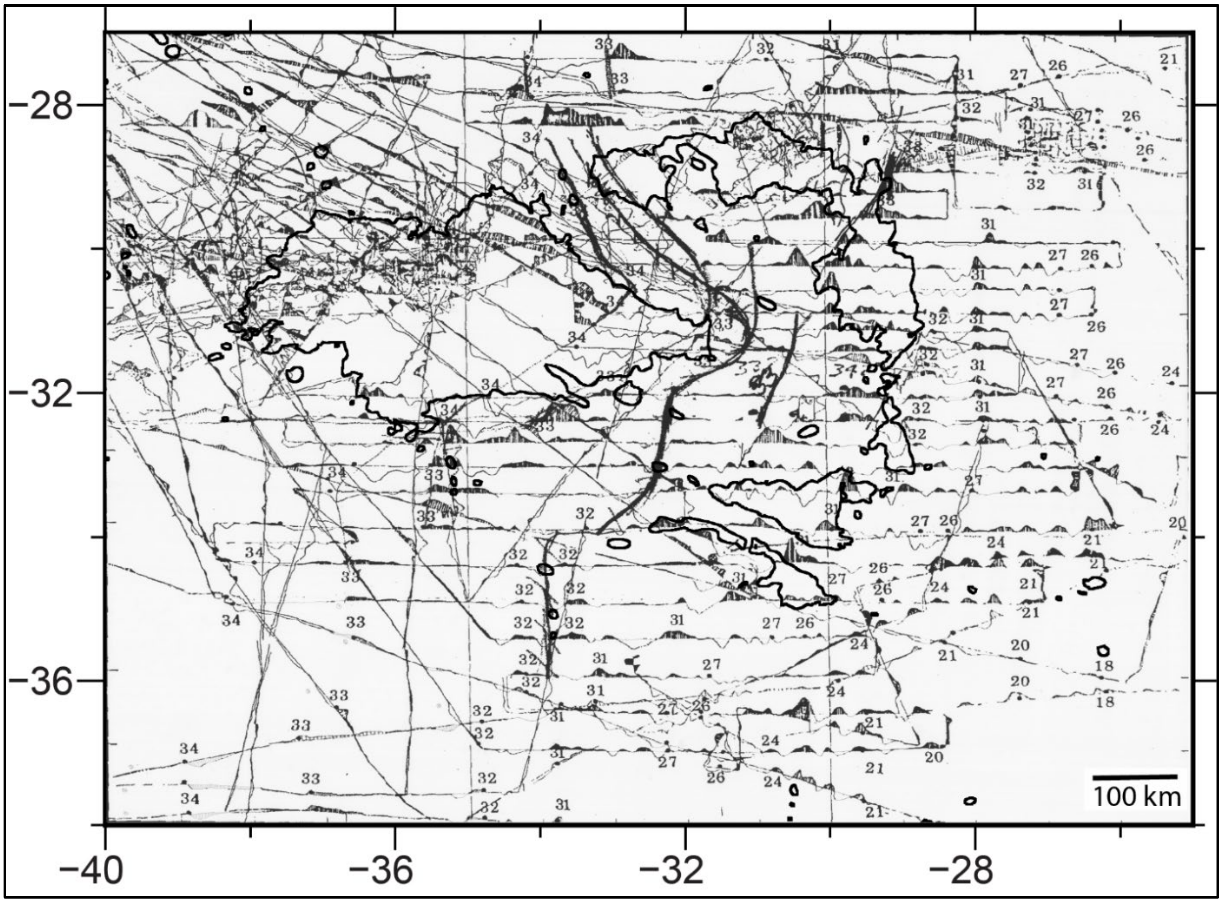

Figure 3.5 – Plot of aeromagnetic survey done by NRL over RGR (source: J.L. LaBrecque)

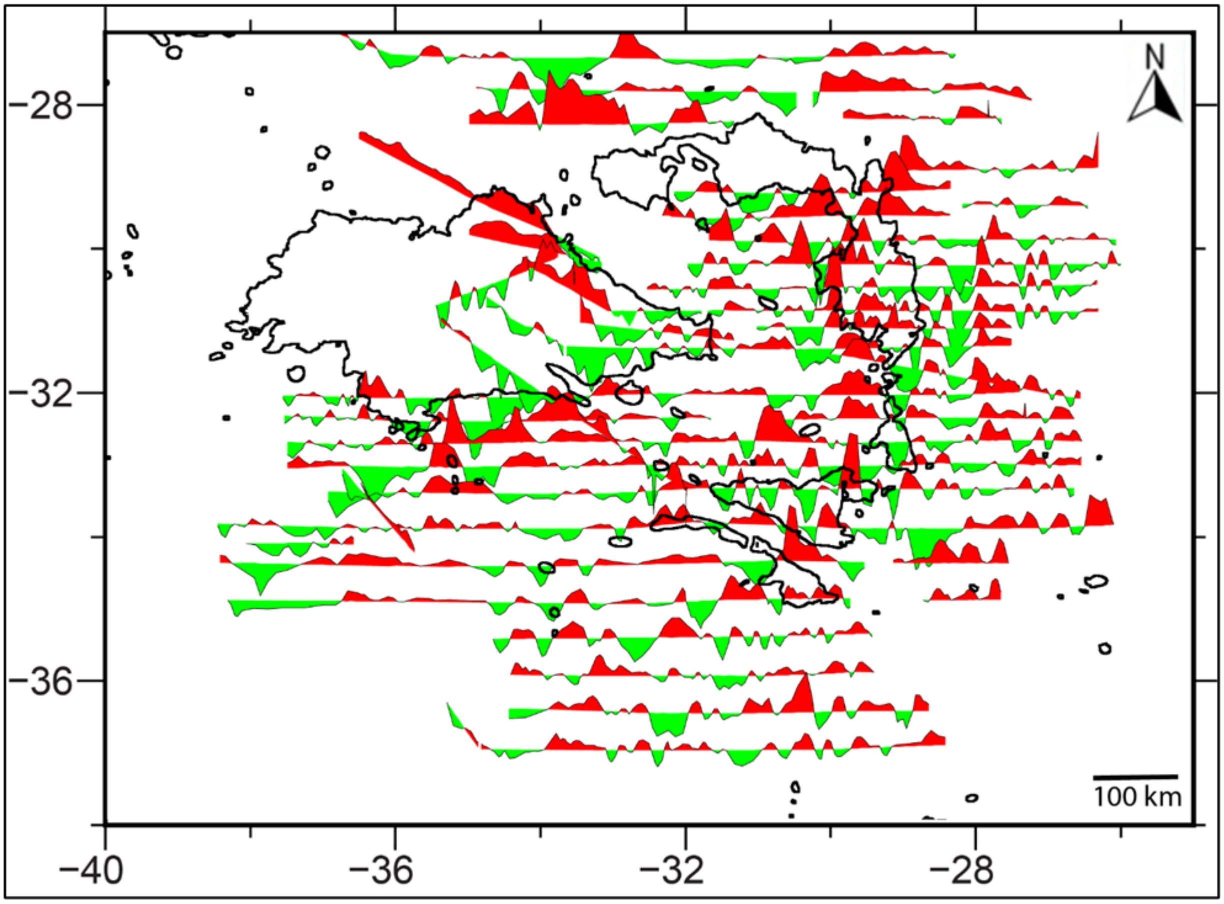

Figure 3.6 – Plot showing magnetic anomaly "wiggle" profiles digitized from the NRL survey shown in Figure 3.5.

Only 30 of the magnetic surveys were navigated using GPS, while the rest were surveyed using less accurate navigation systems such as Doppler satellite systems and celestial navigation. For generating magnetic anomaly maps, all surveys must be carefully merged to generate a coherent magnetic dataset. For this, we followed a "backbone" analysis method, discussed in Huang et al. (2021), which uses GPS navigated data as a backbone and iteratively integrates other navigation type data into the backbone by minimizing error misfits at the "crossover" or intersection points. This method is discussed in detail in the next section.

3.3.2 Data Processing

Magnetometers measure the total field strength at a given location, which is the sum of contributions from internal (core, crustal magnetic sources) and external (e.g., atmospheric and space current systems) sources. To understand the tectonic evolution of oceanic plateaus, we are interested in the magnetic signature of the crust, and the contribution of the other sources must be removed from the total field measurements. In addition, most cruise data contain noise, such as spikes or offsets, probably due to technical issues or disturbance from external factors (e.g., magnetic storms) (Figure 3.7). These noise sources must be removed from the data to reduce the offsets between various surveys and improve the data consistency. After the removal of random noise, the data must be checked for systematic errors such as drifts or offsets by analyzing the Crossover Errors (COE). When merging data spanning several decades, the observed data from different surveys often do not agree at track intersections, for reasons such as navigation uncertainties, resulting in COE. Solving for the COE between tracks is essential prior to gridding and can significantly reduce artificial artifacts and improve data quality.

The first processing step was a careful examination of each survey data file to look for incorrectly recorded date and time entry. For example, most of the early 1960s Vema ship tracks, have incorrectly recorded time 00:00:00 as the end of day (rather than 23:59:59), which leads to incorrect diurnal correction. Similarly, other issues such as missing location fields (latitude or longitude) and non-increasing times have been identified and manually corrected. Due to scant data in the region, we tried to correct and retain as much data as possible. After survey data review, the data are then corrected for the magnetometer layback, which is the offset between the ship position and magnetometer sensor towed behind the ship. Magnetometers are usually towed ~3x the ship length behind the ship to avoid interferences from the vessel. All magnetic data are reported by platform position, so the layback correction calculated the coordinates of the magnetometer by translating the ship GPS coordinates back to the magnetometer based on the assumed layback. Since layback information is not available for most cruises, a value of 3x ship length was assumed for layback when otherwise unavailable.

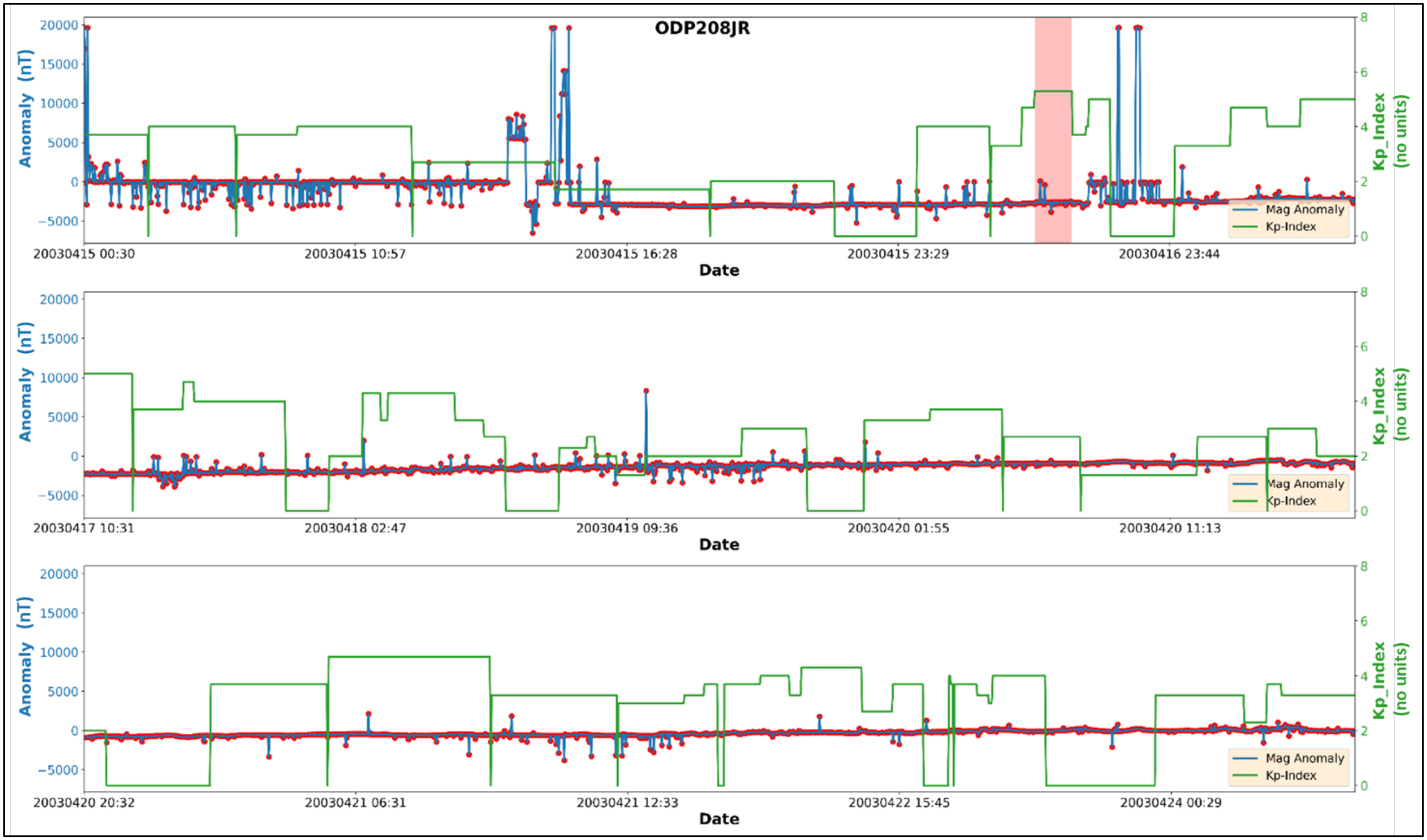

Figure 3.7 – Examples of data with outliers and noise. Data is from NCEI cruise ODP208JR. Blue line is the anomaly profile whereas red points are individual data points. Green profile is Kp index, plotted along survey. Red region shows the occurrence of a geomagnetic storm. The horizontal axis is the survey date. There are two vertical axes, left = anomaly (nT); right = Kp_index

After the magnetic coordinates are calculated, the Earth's main field originating within the core is subtracted from the total field by using the latest 13th generation International Geomagnetic Reference Field (IGRF-13; Alken et al.,2021). This version of the IGRF is valid for all dates in the data set. The Earth's magnetic field at a location also varies diurnally, on the order of a few tens of nT over the course of the day. This variation mainly arises due to solar radiation interacting with the Earth's magnetosphere and is a function of latitude and time. Magnetic data are usually corrected for this variation by having a magnetic base station in the study area to monitor this variation, which is subtracted from the data. However, since having a base station in oceans is not practical, we relied on the data recorded at onshore INTERMAGNET observatories (www.intermagnet.com) close to the study areas for this correction.

For the surveys over WR, the magnetic observatory at Tsumeb, Namibia (ID: TSU; 17.58°E, 19.20°S) was used, which is ~1300 km away from Valdivia Bank. The magnetic observatory in Vassouras, Brazil (ID: VSS; 43.65°W, 22.40°S), ~1200 km from RGR Massif was used for the surveys over RGR. These observatories record the total field strength at the station and to obtain the diurnal variation, the base station background magnetic field (Fbase) must be subtracted from the recorded magnetic field. Fbase of the magnetic observatories were calculated by averaging the field values during nighttime (between 10:00 PM and 4:00 AM local time) on international quiet days (World Data Center for Geomagnetism, Kyoto) for a particular survey month. The resulting Fbase is used to calculate the diurnal variation for the station (Figure 3.8) and the values are time corrected for longitudinal differences between the survey area and station. Finally, these values are subtracted from the IGRF-corrected field to get diurnal-corrected magnetic anomalies. Most of the diurnal corrections done were in the range of ± 25 nT.

For final quality control step, data are checked to see if they are affected by magnetic storms, which are large disturbances in the Earth's magnetic field caused by solar particles. These disturbances have a field strength in order of 100 - 1000 of nT and if the survey is badly affected, the data can be rendered useless. To monitor the magnetic storms, we obtained the Kp-indices from NCEI database. The Kp-index is a scale for measuring the magnitude of geomagnetic disturbances. It is a measure of solar flux and has a higher value when solar activity is high (Dessler and Fejer, 1963). A Kp-index value of > 5 indicates a potential magnetic storm. We plotted the magnetic anomaly data against the Kp-index values and looked for all the survey dates that could have been corrupted by the magnetic storms, inspected the values based on character and COE, and deleted the bad data (Figure 3.9).

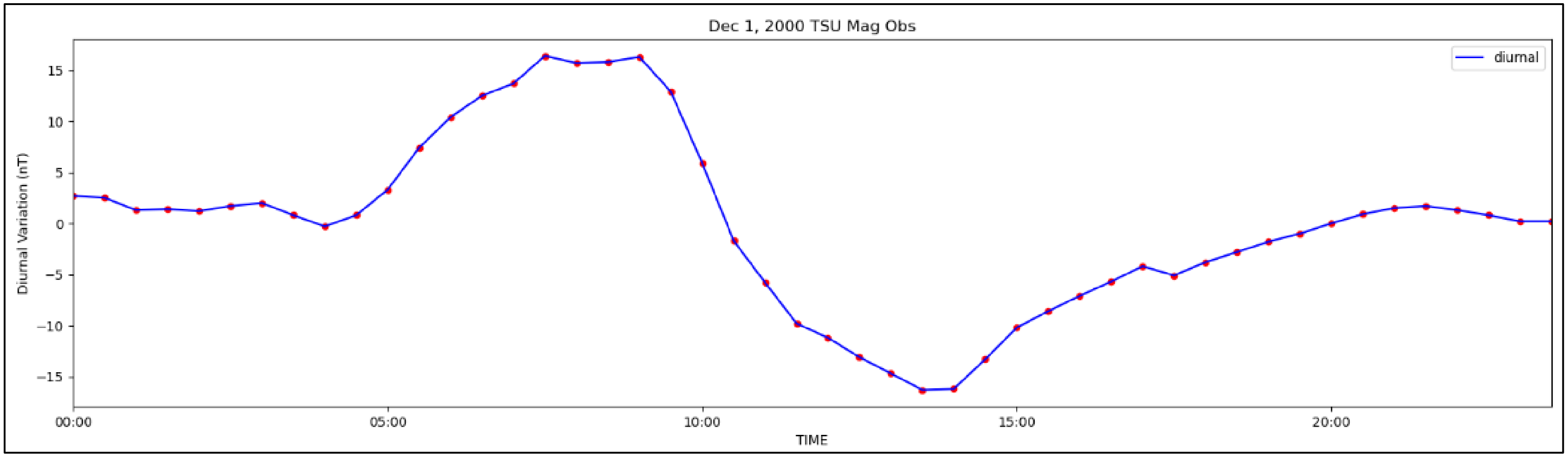

Figure 3.8 – Example of the diurnal curve for one day generated for Tsumeb magnetic observatory on December 1, 2000. Horizontal axis is time (in hours) and vertical axis is diurnal variation in nanoTeslas (nT)

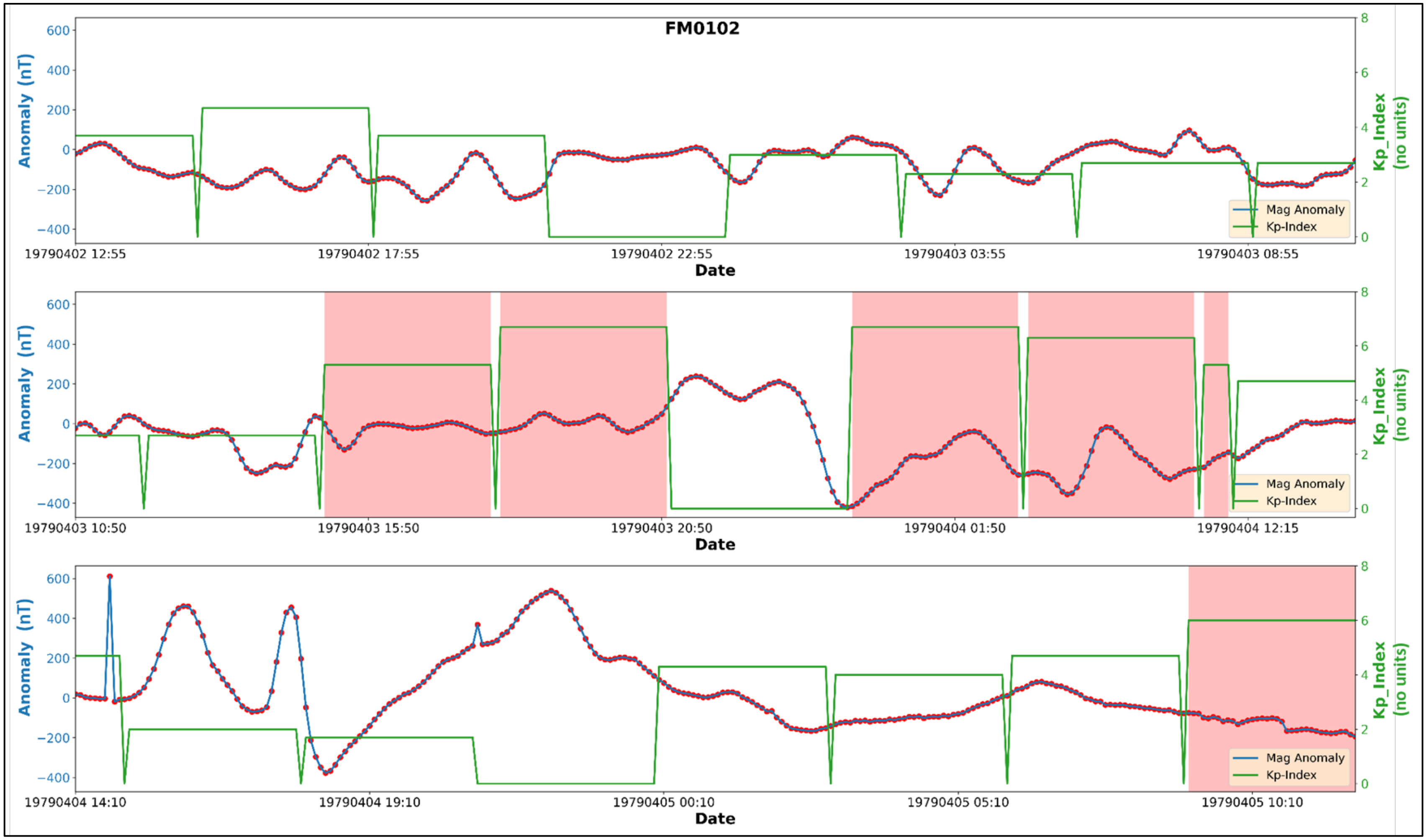

Figure 3.9 – Examples of data possibly affected by geomagnetic storms. Data is from NCEI cruise FM0102. Blue line is the anomaly profile while red points are individual data points. The green profile is the Kp index plotted along the survey. Red region shows dates of geomagnetic storm occurrence. Horizontal axis is survey date. There are two vertical axes, left = anomaly (nT); right = Kp_index. Red areas show Kp index >5 and are possibly affected by magnetic storms. However, inspection indicated no rapid shifts as might be expected from a storm, so these data were retained

COE analysis is the final step in the magnetic data processing and is done to minimize misfits between different surveys to improve overall data consistency. These misfits are often a result of less accurate navigation systems used in the surveys prior to the introduction of GPS navigation. Our dataset spans several decades and contains both well-positioned data (GPS) and poorly positioned data (pre-GPS). Older surveys with the pre-GPS era navigation systems had limited position fixes and relied on dead reckoning in between the fixes, leading to positions being off by few hundreds of meters to a few kilometers. In contrast, the newer surveys using GPS systems have highly accurate and regular positions. To solve for the misfits, we followed the "backbone analysis" method laid out in Huang et al. (2021). First a "backbone" is generated by merging all GPS navigated data. Older surveys with less accurate navigation were iteratively merged into the backbone by shifting the anomalies of each survey segment by a constant offset, which is the mean COE of that survey versus the "backbone". As more and more surveys were corrected, the backbone grew. All the COE analysis was done using x2sys package of GMT software (Wessel et al., 2019).

Anomaly maps were generated by gridding the processed magnetic anomalies using GMT. Prior to gridding, the magnetic anomalies are averaged within 2 x 2 arc minute cells using the GMT routine *blockmean* to avoid spatial aliasing and average out redundant data. Subsequently, the anomalies were gridded using the GMT routine *surface,* which uses tension splines to grid the data. Gridding used grid spacing of 2 arc minutes and a tension factor of 0.25.

3.3.3 Tectonic Reconstruction of Magnetic Maps

Although several tectonic models (Nurnberg and Müller, 1991; Müller et al., 1993; Torsvik et al., 2009; Perez-Diaz and Eagles, 2014; Bird and Hall, 2016) have been proposed for the opening of Atlantic, our study area is limited to chrons C34n-C30n and do not impact our study. To understand the tectonic evolution of WR and RGR, the generated magnetic anomaly maps were reconstructed to their past configurations using total reconstruction poles from the Matthews et al. (2016) global plate model. For the South Atlantic, total reconstruction poles are available for chrons C34n (83.6 Ma) and C30n (66.4 Ma). For reconstruction to all other chrons, the total poles were converted to stage poles using GMT routine *rotconverter*, and the stage poles were used to interpolate between C34n and C30n. For all reconstructions, the African plate was fixed, and the South American plate was rotated to the African plate. All reconstructions were done using GMT routines *grdrotater* and *backtracker*.

Late Cretaceous reconstructions using the poles for the South Atlantic seem to work for only the chrons with calculated total reconstruction poles (C34n and C30n). For other chrons, the closing angles are off by ~1-2° and the reconstructions do not completely close the gap between the two plates. This turned out to be an issue with the South Atlantic reconstructions that have not been scrutinized or revised in detail for decades (Dietmar Müller, personal communication, 2021). To deal with this, we tweaked the closing angle for chrons with inaccurate reconstructions and choose an angle that gave the best fit between anomalies picks from South American and African plates to the north and south of the tectonically anomalous region. These updated angles were then incorporated into the rotation model and the maps were reconstructed using this updated model.

3.4 Results

The MAR reorganization between WR and RGR is restricted to the region between the Rio Grande-Florianopolis FZ (22°S at the MAR) on the north and the 35.5°S FZ (at the MAR) on the south (Figure 2.1) and between magnetic chrons C34 (83.5 Ma) and C30 (66.4 Ma) (Thoram et al., 2019; Sager et al., 2021), which is the focus of this study. To the north and south of these FZs, seafloor spreading is normal as evident from the magnetic anomaly widths complete reconstructions. However, in the region in between, spacing between anomalies is uneven between WR and RGR, with no prior picks existing over Centaurus Basin (Figure 3.2). In this region, there are large asymmetries in crustal accretion as previously noted by Müller et al., (2008), who attributed it to be a product of hotspot-ridge interaction, probably involving lithosphere transfer between the plates. The anomaly patterns become regular by anomaly C30 (66.4 Ma), when the MAR reorganization ended, and normal spreading was restored. To aid description, the study area is divided into 4 spreading corridors A-D (Figures 3.10, 3.12) and the magnetic anomaly maps for WR and RGR are discussed below. Following the convention established in Chapter 2, all magnetic anomaly picks (isochrons or "chrons") correspond to the young end of the normal polarity block anomaly, except for anomaly C33r, which corresponds to the young end of the reversed block anomaly. In scenarios where the entire polarity block was not completely preserved on a plate (e.g., part of the block is transferred to the conjugate plate or the anomaly is split into multiple blocks), we still interpret the young end of the preserved block as the isochron, although in such cases the picks no longer correlate with anomaly age. Using Ogg (2012), the ages for the anomalies discussed in the text are C34n (83.6 Ma), C33r (79.9 Ma), C33n (74.2 Ma), C32n.1n (71.4 Ma), C30n (66.4 Ma).

3.4.1 Walvis Ridge

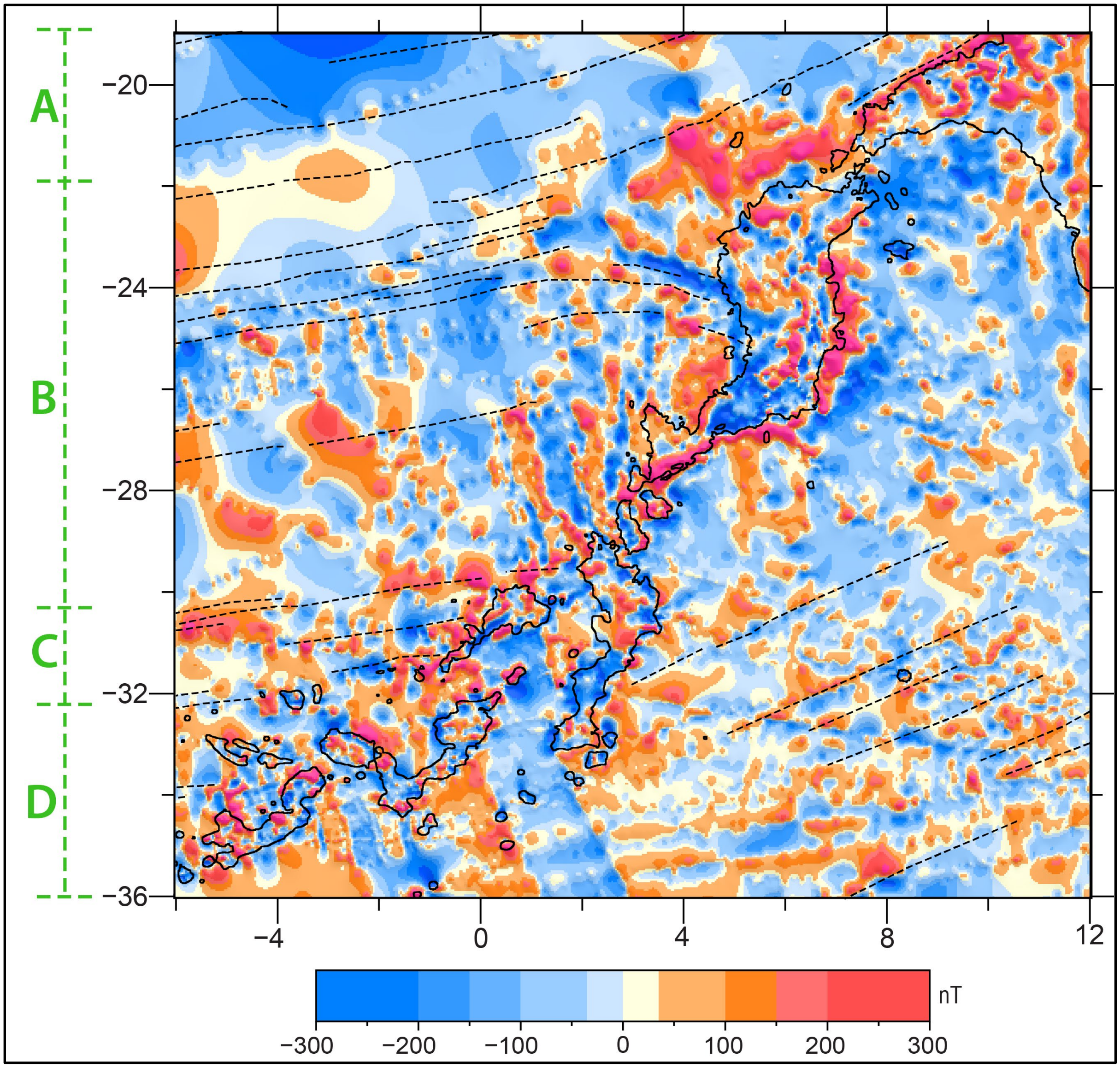

Figure 3.10 –Magnetic anomaly map for WR. Black dashed lines shows fracture zones (from Sager et al., 2021). Red (blue) zones show areas of positive (negative) magnetic anomaly. Thin black line is the 3000 m bathymetry contour. Green dashed lines on the left show the spreading corridors (A-D) which are discussed in the text.

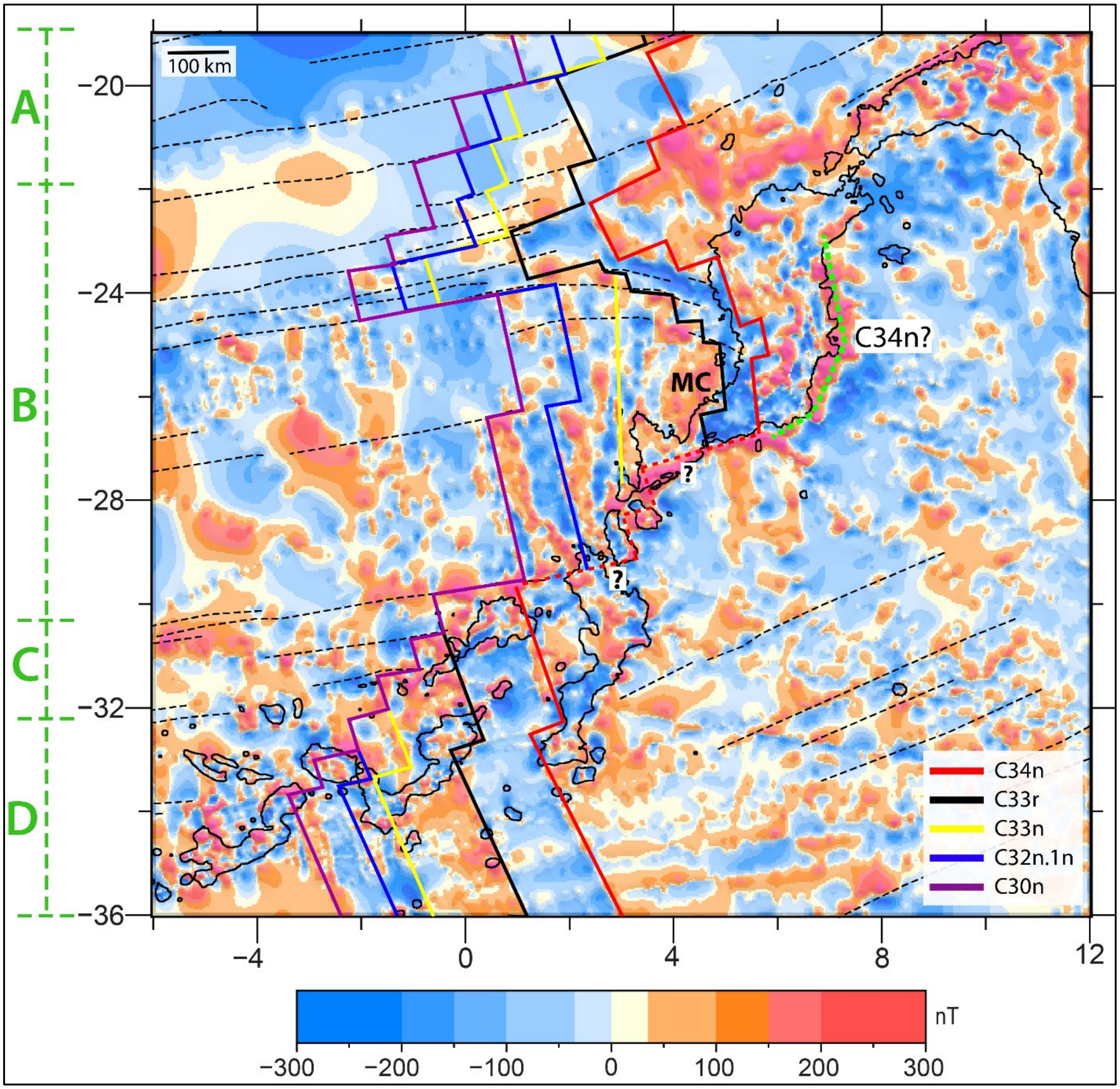

Figure 3.11 – Interpretation of magnetic anomaly map over WR. Thin black line is the 3000 m bathymetry contour. Only interpretation for anomalies C34n – C30n are shown. Black dashed lines show fracture zones (from Sager et al., 2021). Red (blue) zones show areas of positive (negative) magnetic anomaly. Green dashed lines on the left show the spreading corridors (A-D), which are discussed in the text. Red dashed line is an interpretation of C34n, where the anomaly pattern is not clear. MC=Microplate Core

This section builds upon the anomaly patterns described in Chapter 2, by reinterpreting and updating anomaly picks based on magnetic maps generated using the data. The anomaly map for WR covers the area between 19-36°S, 6-12°E, with a total of 55 tracks (Figure 3.3). The anomaly patterns are clearly defined in regions with good data coverage, while in regions with poor data coverage, the patterns are not clear, and the gridding algorithm produced rounded anomalies. The map has been divided into 4 spreading Corridors A-D, bounded by fracture zones (Figure 3.10). Corridor C and D are the most well surveyed regions of WR where the track density is the highest and the magnetic anomalies in these regions are linear and clearly defined. The track coverage in Corridor B, has been significantly improved over VB and Central WR, owing to the new magnetic surveys conducted for this study. However, in the region east of VB, over the area of 26-29°S, 1-6°E, the coverage is poor and only few tracks traverse the area, resulting in poorly defined anomalies. Even though anomaly picks exist in Corridor A from Cande et al., (1988), we were unable to locate any tracks in the NCEI database, thus the picks were retained as published.

In Corridors A and D, the magnetic anomalies are normal and display regular spreading, which is evident from the width of the anomalies (Figure 3.11). All the anomalies in these corridors trend ~N26°W. However, the patterns in Corridor A cannot be reproduced since no tracks were available and the interpretation is based on the picks from Cande et al., (1988). In Corridor D, the anomaly patterns are well defined and anomalies C30n-C34n can easily be traced between 33°S to 36°S. Anomaly C33r is readily identified and as a distinct wide negative band (0.5°E/34°S), outboard (relative to the MAR) of the wide positive band of anomaly C33n (0°E/35°S) wide positive band of anomaly C33n (0°E/35°S). Anomalies C32n.1n (0.5°W/35.5°S) and C30n (2.5°W/35°S) are two narrow positive bands located to the west of anomaly C33n. The negative band of anomaly C33r is located to the left of anomaly C34n (2.5°E/35°S), which is the young end of the Cretaceous Quiet Zone. Anomalies C30n-C34n have all been accounted for in this corridor and the anomaly bands seem to terminate at the south end of the Tristan seamount chain. However, the continuous anomaly bands are disrupted by the Central and Gough seamount chains (Figure 3.11). These chains were formed in an intraplate setting (O'Connor and Jokat, 2015b) and therefore have a different magnetization than the surrounding seafloor, causing this disturbance. We updated the interpretation of anomalies C33r and C34n in this corridor, and unlike previous studies (see Chapter 2; Seton et al., 2012; Muller et al., 2016), where these anomalies have been interpreted as having a trend oblique to South American–African plate spreading, they have been re-interpreted trending parallel to the spreading and offset by a ~50 km transform fault.

There is an age discontinuity of ~15 Ma across the Tristan chain, where anomalies younger than C30n are identified to the north of this chain, while older anomalies (C32n.1n-C34n) exist to the south. In Corridor C, over the north flank of Tristan seamount chain, in a triangular region bounded approximately by 29°S-36°S, 3°W-4°W, anomalies C32n-C33r are missing and only anomalies C30n and younger could be found (Figure 3.11). Here, anomaly C34n, previously not picked, has been interpreted as the east edge of the positive anomaly near the head of Tristan seamount chain (0.5°E/33°S). This anomaly follows a similar trend as corridor D and has been extended all the way to the 30°S FZ.

The anomaly patterns in Corridor B, which spans the area between 22°S FZ and 30°S FZ and comprising of Valdivia Bank and central WR, are complex, with oblique and curved lineations (Figure 3.11). The most striking anomaly here is the curved negative band along eastern flank of Valdivia Bank, which has been interpreted as C33r. This negative band narrows to the north and south of VB indicating that the anomaly is not completely preserved in this section. To the north, this anomaly narrows with width reaching almost zero at 4°E/24.5°S, beyond which the complete widths of C33r are observed.

To the south of VB, another linear negative anomaly trends NE over the SE flank of VB where it is coincident with a rift valley. The cause for the bifurcated chron C33r is not clear. The intervening positive anomaly could be a bit of Cretaceous Quiet Zone inserted by a westward ridge jump. Alternatively, the positive crust could have been remagnetized during a normal polarity period owing to Eocene volcanism that has affected VB (Homrighausen et al., 2019). Anomaly C34n is interpreted as the edge of the positive anomaly adjacent to C33r to the east, though this might not be the actual edge of Cretaceous Quiet Zone. Interestingly, a strong linear positive anomaly (7°E/26°S) can be observed trending along the eastern flank of Valdivia Bank. This anomaly trends ~N-S parallel to the bathymetry contours from 23°S to 29°S, which then bends by ~110° and trends southwest between 7°E to 4°E. This anomaly also trends parallel to the rift valley on eastern VB, suggesting that the anomaly is a spreading related feature. This high amplitude positive anomaly at the east edge of VB could be anomaly C34n that was abandoned as a result of a ridge jump.

C30n and C32n.1n anomalies can also be easily traced in this corridor and are two narrow bands of positive anomalies separated by a narrow negative band, all located to the west of Valdivia Bank (Figure 3.11). These bands trend ~N15°W perpendicular to spreading between the 30°S FZ and the curved FZs over west VB and are offset by a ~75 km long transform offset at the 27.5°S FZ. To the north of 24°S, the data control is poor and anomalies C30n-C33n are estimated based on width expected from normal spreading.

No anomaly identifications could be made to the east of anomaly C32n.1n at 28–30°S. There is an abrupt break in the anomaly sequence across WR at this latitude (Figure 3.11). The entirety of positive anomaly C33n and negative anomaly C33o seem to be missing in the region. Similarly, the correlations are complex east of anomaly C32n.1n between 25–28°S. Here only about half of anomaly C33n seems to be preserved, which is the positive anomaly (4°E/27°S) located near the south end of VB. This anomaly continues north with a trend of ~N15°E, oblique to the direction expected for South American-African plate spreading, and terminates where anomaly C33r curves into eastern flank of VB. Two more unidentified anomalies to the east of this C33n, a narrow negative (4°E/26°S) and a wide positive anomaly (5°E/26°S), also trend obliquely to spreading and seem end at anomaly C33r. Coincidently, curved FZs are observed in the region where these oblique lineations end.

3.4.2 Rio Grande Rise

Even with the addition of new surveys, there are large gaps in track coverage especially over the eastern flank and southern flanks of RGR Massif and parts of Centaurus Basin (CB), where only a few tracks exist (Figure 3.4). Due to sparse data points in this region, the gridding algorithm produced rounded anomalies and magnetic lineations are not clear. Furthermore, in the regions where we have sparse data control near RGR, the interpretations were based on extra anomalies observed where none were expected because they were missing on the African plate. Our rationale for following this procedure is that the amount of crust generated at the MAR, is dependent on the opening angle, and is always conserved. If a certain amount of anomaly is missing on one plate, it should be located on the conjugate plate, probably transferred due to ridge jump.

The anomaly map for RGR covers the area between 23-45°S, 24-45°W, with a total of 53 tracks (Figure 3.12). This region has been divided into four spreading corridors, which are the counterparts of those on the African plate discussed in the previous section. The western end of the RGR massif is the most surveyed region, but unfortunately this area formed during the CNS and does not show any linear anomaly pattern. This region is covered by high frequency anomalies with no evident pattern. Coincidentally, a linear negative anomaly is observed to coincide with the Cruzeiro do Sul rift (CdS). These anomalies and the CdS rift are probably a result of Eocene volcanism that is known to have occurred over RGR Massif (Gamboa and Rabinowitz, 1984). There exist only a couple of small marine surveys in the entire Centaurus Basin, including eastern RGR Massif and E-RGR. In these regions, most of the anomaly patterns come from the NRL aeromagnetic survey (Figure 3.4).

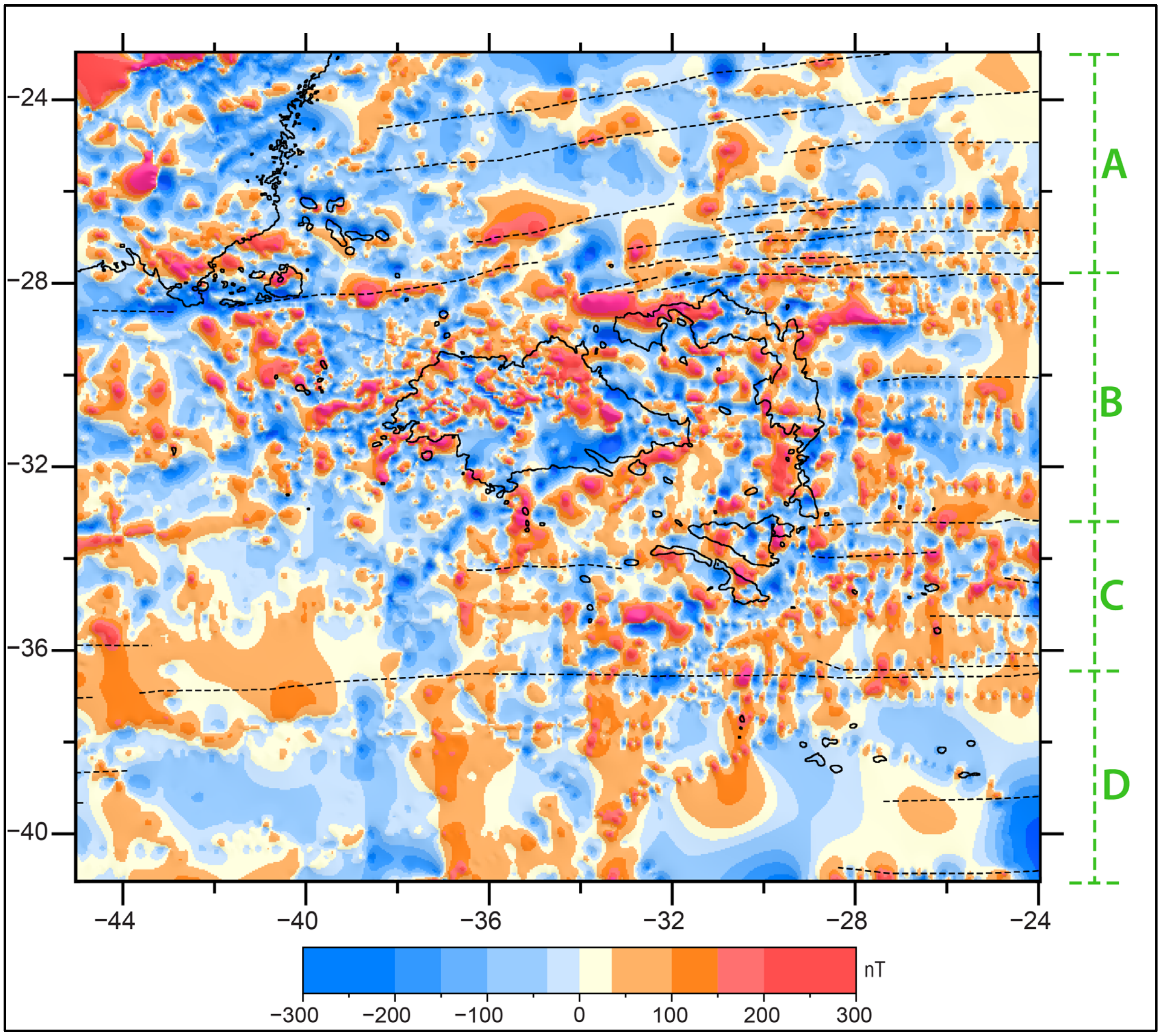

Figure 3.12 – Magnetic anomaly map for RGR and environs. Black dashed lines show fracture zones (from Sager et al., 2021). Red (blue) zones show areas of positive (negative) magnetic anomaly. Thin black lines show the 3000 m bathymetry contour. Green dashed lines on the right show the extents of spreading corridors (A-D) which are discussed in the text. The spreading corridors here correspond to the WR corridors in Fig 3.10.

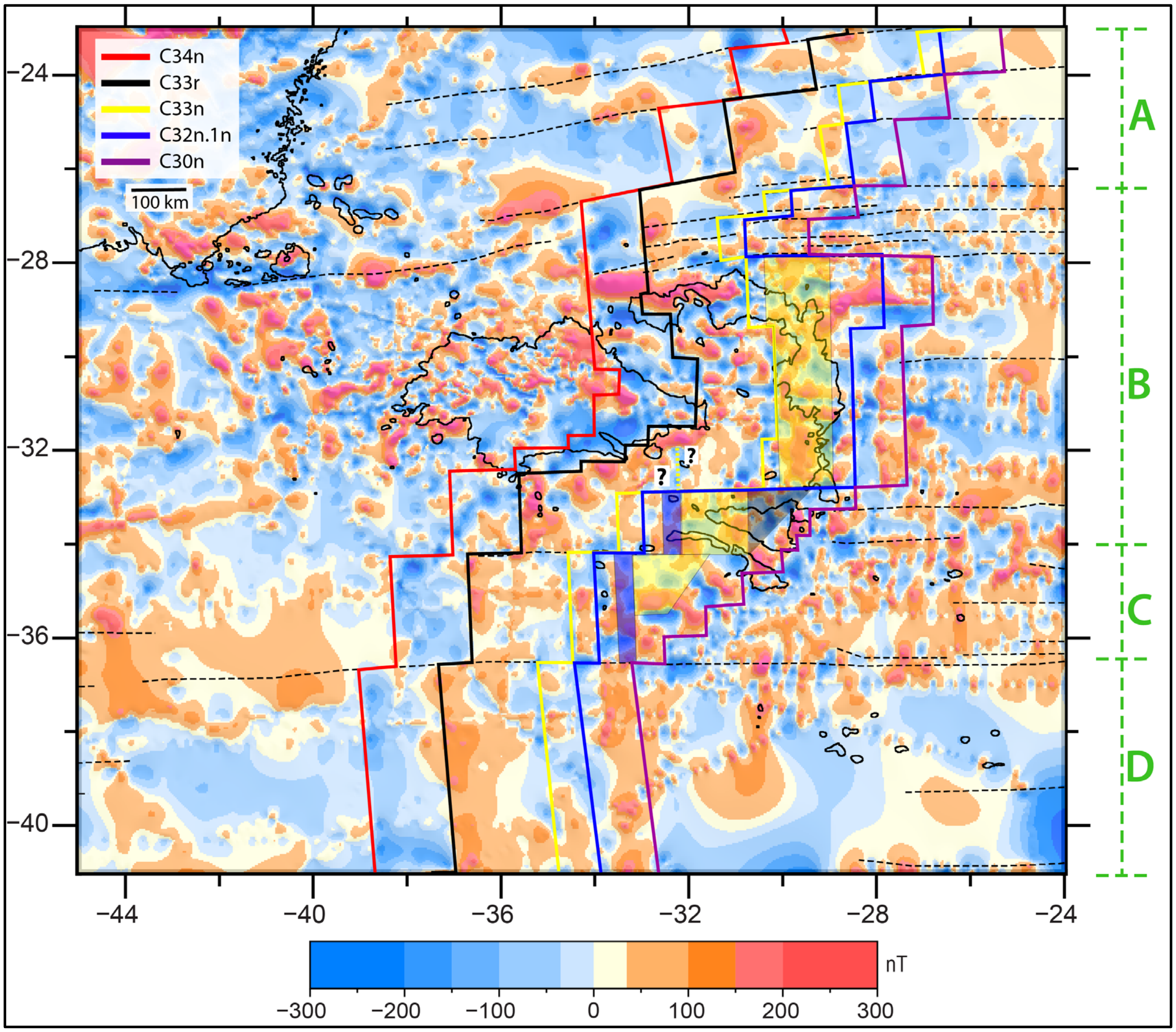

Figure 3.13 – Interpretation of magnetic anomalies over RGR. Only interpretation for anomalies C34n – C30n are shown. Black dashed lines show fracture zones (from Sager et al., 2021). Red (blue) zones show areas of positive (negative) magnetic anomaly. Thin black line shows the 3000 m bathymetry contours Green dashed lines on the right show the extents of spreading corridors (A-D) which are discussed in the text.

In corridors A and D, data coverage is good, and the anomaly patterns are clear. Here, anomalies C34n-C30n can easily be traced and have widths consistent with normal spreading. Anomalies in these corridors trend ~N6°W. In corridor A, all anomalies two large offsets at 25°S and 26°S FZs. Here, most of the anomaly patterns agree with the picks from Cande et al., (1988). Based on the anomaly maps, we refined the interpretation of lineations by making them more rectilinear and orthogonal.

In corridor C, anomalies C34n-C32n.1n can easily be traced and the widths are consistent with normal spreading. However, there appears to be a duplication of anomalies to the east of anomaly C32n.1n. This duplication of anomalies is restricted to a triangular region, bounded approximately by 35-38°W, 31-33°S. Anomaly C32n.1n is the first anomaly that is repeated in this corridor and magnetic anomaly profiles, reveal this anomaly to be mirroring the nearby anomaly C32n.1n farther west in this corridor. Similarly, moving further east past C32n.1n, anomaly C33n seems to be repeated and mirroring anomaly C33n already traced in this corridor. However, this duplication of anomaly C33n starts at ~36.2°S, where only half of the width is repeated and this width continuously increases north to ~34°S, where the entire anomaly C33n width is repeated. This duplication zone is bounded to the east by anomaly C30n, where a ~400 km long offset in this anomaly across this corridor is split into several smaller offsets. Further east, anomalies younger than C30n have been identified by Cande et al., (1988) and they seem to follow normal spreading.

Corridor B has a complex anomaly pattern and has been divided into two smaller regions for convenience. B1 is the region between 28-33°S and B2 is the region between 33-34°S. Corridor B2 is north of corridor C and appears to extend the duplication of anomalies further north. Anomalies C34n-C32n.1n are evident and widths are consistent with normal spreading.

Like corridor C, there is a duplication of anomalies east of C32n.1n, in a roughly triangular region, bounded approximately by 29-32°W, 33-34°S. In addition to duplications of anomalies C32n.1n and C33n, negative anomaly C33r is also repeated in this corridor and occurs as an inverted triangular region over SE-RGR. This duplication zone is bounded by anomaly C30 to the east and similar to corridor C, the C30n seems to offset by several small offsets.

Corridor B1 encompasses most of Centaurus Basin and eastern RGR Massif, where data coverage is poor, and most the anomalies are derived from the NRL aeromagnetic survey. In this corridor, anomaly C33r is the easiest anomaly to trace, as wide negative anomaly running through eastern flank of RGR Massif. The east end of this negative anomaly has been picked as a C33r and the west end has been picked as C34n. Anomalies C32n.1n (29°W/32.5°S) and C30n (32°W/28.5°S) are the other set of anomalies that can be identified in this corridor, which are two narrow positive bands separated by a negative band, running parallel to E-RGR over the east side of the ridge. There are two wide positive anomalies separated by a narrow negative anomaly covering most of the Centaurus Basin and E-RGR. Due to poor data control in this region, the anomaly interpretation here is based on the missing anomalies in the conjugate corridor on the African plate. The width of the wide positive anomalies observed in this corridor over the Centaurus Basin, is ~2x the normal spreading width of anomaly C33n, which is also missing from the conjugate corridor on African plate. The positive anomaly to the east of RGR Massif has been interpreted as C33n on South American plate, whereas the positive anomaly on the west of E-RGR has been interpreted as C33n from African plate, probably transferred by a ridge jump. The negative anomaly in between these two wide positive anomalies is interpreted as anomaly C33r. Normal spreading occurs in the corridor north of the 28°S FZ, where there is no repetition of any patterns and anomalies C34n-C30n are all accounted for, however several FZ appear to offset the anomaly pattern. There is a large positive anomaly (33°W/29°S) near the northwestern tip of E-RGR, which is a result of a suspected artifact in the NRL aeromagnetic dataset. The abnormally high positive value of the artifact forced the negative anomalies in the region to appear as positive, disrupting the negative band of C33r. This artifact removal will be addressed in future versions of the magnetic map.

3.5 Discussion

A major reorganization occurred in the South Atlantic prior to chron C34n (83.6 Ma), ending around chron C30n (66.4 Ma). This reorganization may have been triggered when the MAR jumped eastward during the Cretaceous Quiet Zone period, resulting in asymmetric accretion in the South Atlantic (Müller et al., 2008; Pérez-Díaz & Eagles, 2014). Vema Trough (VT), which is a ~N-S trending bathymetric valley west of RGR, has been proposed to be the abandoned ridge left behind by this ~400 km eastward ridge jump (Pérez-Díaz & Eagles, 2014; Sager et al., 2021). This reorganization broke up ~400 km long transform offset in anomaly C34n at the RGR/FFZ, located north of WR and RGR (Sager et al., 2021) into smaller FZs. As the new spreading ridge restructured, this long-offset transform propagated southward and split into multiple smaller transform offsets by anomaly C30n (Sager et al., 2021). During this propagation, the destruction of this transform offset was initiated and overlapping spreading centers were developed on both the sides of the fault (Gerya et al., 2012). This resulted in the formation of a microplate between the overlapping spreading centers that was eventually incorporated into the South American plate via a ridge jump. Based on crustal thickness mapping of South Atlantic crust, Craça et al. (2019), suggested that three eastward ridge jumps, one before the Vema Trough, one in the center of Centaurus Basin (CB), and one on the east side of the E-RGR, were involved in this ridge reorganization. However, they do not propose the timings for these ridge jumps. Based on tectonic and magnetic anomalies (Sager et al., 2021; Thoram et al., 2019) proposed that a microplate existed during the Late Cretaceous, and the older parts of WR and RGR formed at the boundaries of this microplate, further complicating this ridge reorganization. Based on the extra width between anomalies, these studies proposed that a microplate was eventually incorporated into the Centaurus Basin via an eastward jump. All these studies were based on the limited resolution magnetic models at the time and which are insufficient to study the detailed reorganization of this ridge.

The newly acquired data significantly improved spatial data coverage over WR. Incorporating the digitized NRL aeromagnetic data into the magnetic maps of RGR, revealed distinct patterns in Centaurus Basin, which was lacking in all prior magnetic models. The magnetic maps aided in confirming anomaly picks in GSFML database (Seton et al., 2014) and allow for the definition of new isochrons where none previously existed. This allows us to refine earlier interpretations of isochrons around WR and RGR in order to better comprehend their Late Cretaceous genesis.

From the recent R/V Thomas G. Thompson cruises (TN373, TN374) over WR, we have better data control over WR evolution. Despite the addition of new magnetic data over RGR, there remain large data gaps, particularly over the eastern RGR Massif and Centaurus Basin, where gridding algorithms have likely filled gaps with spurious anomaly patterns, making interpretation more difficult. For interpretation of patterns in regions with sparse data control over RGR, we have relied on the anomaly patterns near WR within the same spreading regime. The widths and variations of anomaly bands on both sides of the Atlantic were compared to expected widths based on the opening rate to arrive at this interpretation. For instance, if certain anomalies are missing on African plate, they should be located on the conjugate South American plate, probably transferred via a ridge jump.

Reconstructing the newly interpreted magnetic lineations to C34n time (83.56 Ma) reveals a wide positive anomaly bounded by the two 34n isochrons (Figure 3.14). This suggests that there is some extra crust from the Cretaceous Quiet Zone that is present between the two isochrons, preventing the isochrons from closing. This extra crust lies between the two isochrons, implying that the picked anomalies formed on different ridges on the boundaries of a microplate. This positive anomaly is interpreted as the core of the microplate and is located west of VB (Figure 3.11). Although there are several possible interpretations of this positive anomaly, this interpretation was favored over others because all the other anomalies have been successfully accounted for. This differs from the previous interpretations (Thoram et al., 2019; Sager et al., 2021), who suggested the core of the microplate is in Centaurus Basin. During this time, reconstructions show VB and RGR Massif forming together near the boundaries of the microplate (Figure 3.14).

Reconstruction reveals that a microplate existed through chron C33r, which shows two negative bands of anomaly 33r forming around a positive core. This interpretation is based on the fact that the reconstructions for the South Atlantic to chron C33r do not close between VB and RGR, suggesting presence of extra crust that belongs to the Cretaceous Quiet Zone. Additionally, anomaly C33r over VB seem to be offset by several small transform offset which coincide with the location of the curved FZs. A microplate formation is often accompanied by rotation and curved fracture zone formation along the edges, because of differential spreading across the two boundaries (Bird and Naar, 1994; Naar and Hey, 1991; Lonsdale et al., 1988). These curved fabrics can clearly be observed around microplate at fast spreading ridges due to faster spreading rates (e.g., Bird et al., 1998), where the center often rotates forming oblique and anomalous fabric. This microplate seems to have rotated ~10° clockwise while forming C33r.

However, around chron C33n time, the magnetic anomaly pattern indicates the east spreading ridge became extinct and anomaly 33n was formed only at the western ridge (Figure 3.14). During this time, volcanism at this spreading center resulted in forming the E-RGR on African plate and Centaurus Basin on the South American plate. The magnetic anomaly patterns imply that a major eastward ridge jump occurred in Centaurus Basin around C32n.1n, incorporating E-RGR into the South American plate. This ridge jump was proposed because anomaly C33n could not be identified to the west of VB. Estep et al., (2020) found significant extensional deformation in seismic data over E-RGR, further supporting the idea that E-RGR formed at the spreading ridge. After this ridge jump, normal spreading was restored in the South Atlantic and the hotspot drifted under the African plate, ceasing evolution of RGR while WR formed three seamount chains.

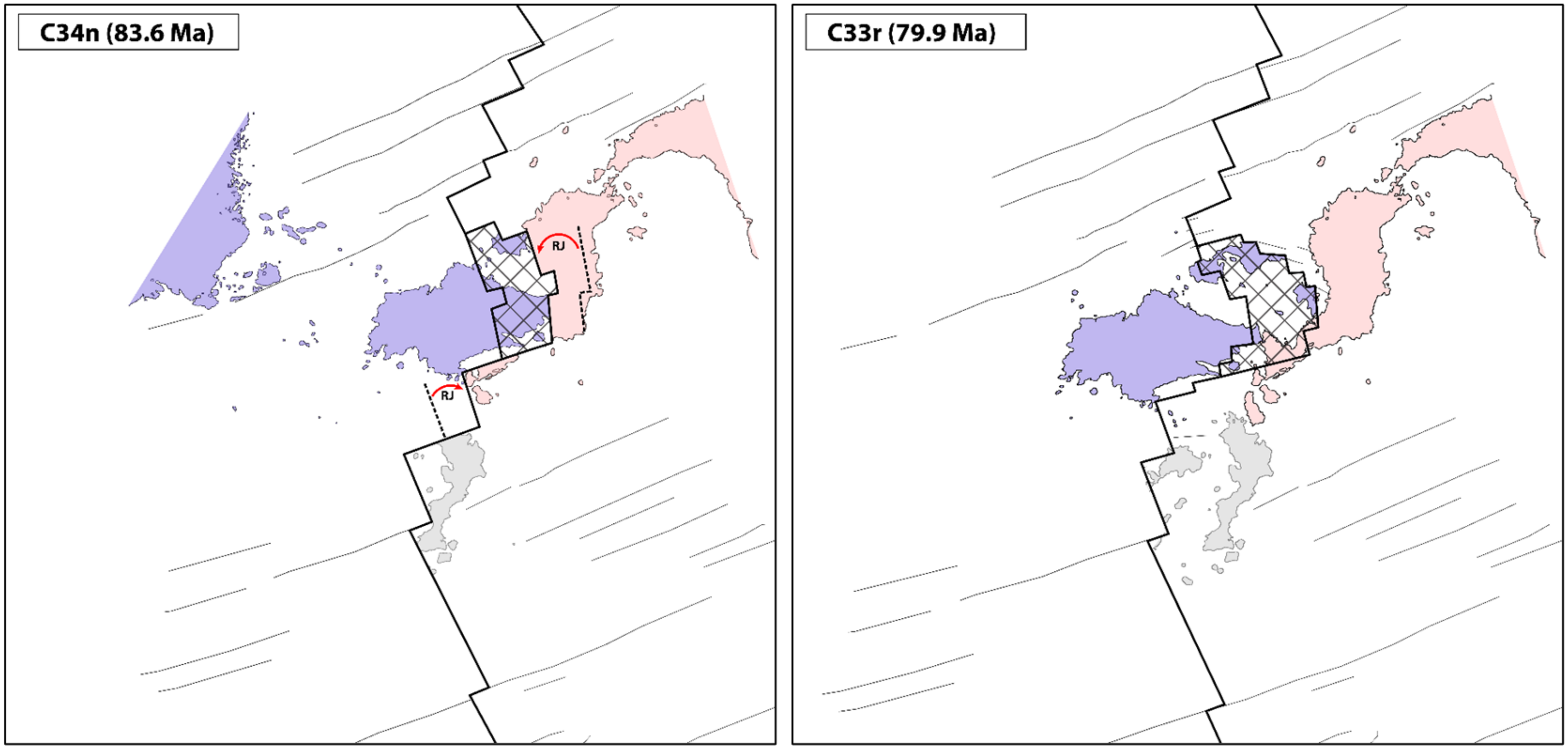

Figure 3.14 –Tectonic sketch of the MAR reorganization and microplate formation. The age of each panel and correspondence with magnetic isochron (if any) is given in the upper left corner. Purple polygons represent RGR above 3000 m depth and pink represents WR above 3000 m. Heavy lines denote active spreading ridges and transform faults.

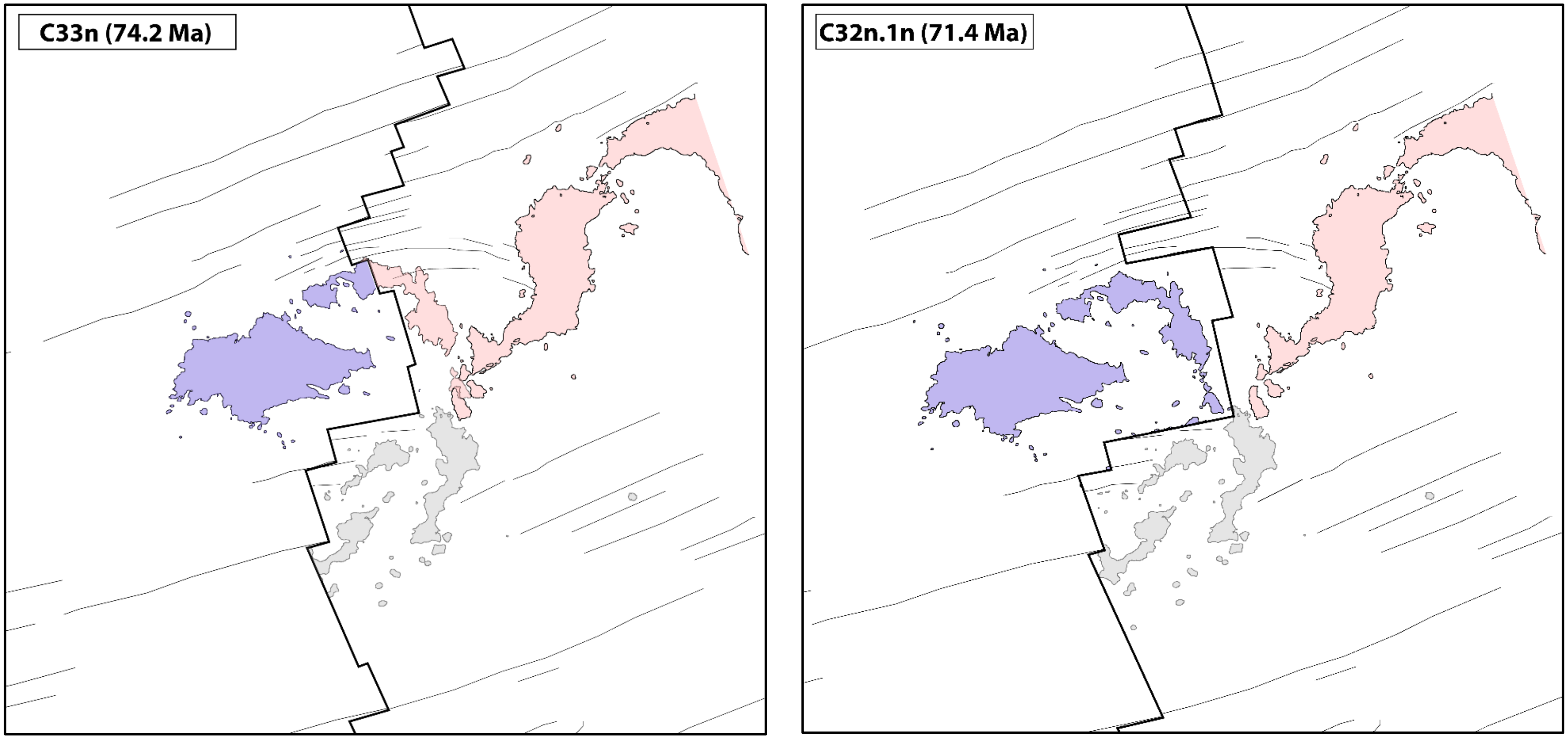

Figure 3.14 (continued)

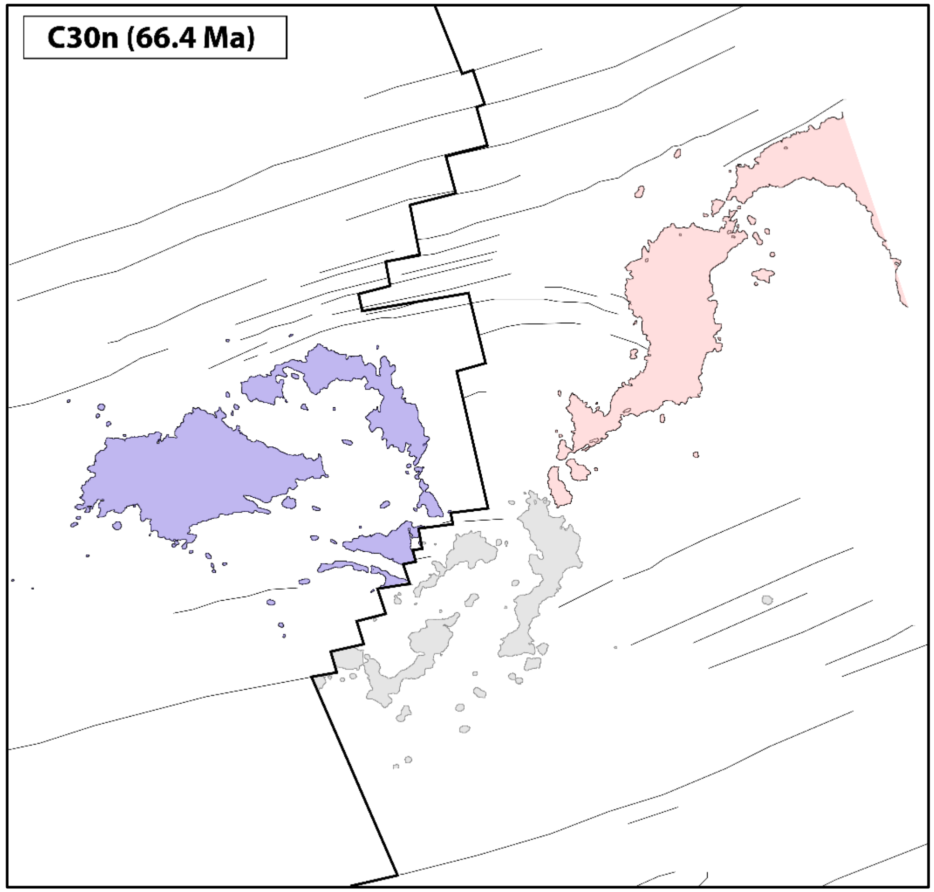

Figure 3.14 (continued)

3.6 Conclusions

This study used a large and diverse magnetic dataset, combining newly acquired and existing surveys over WR and RGR, spanning over six decades, to compile a gridded dataset of magnetic anomalies. After removing the contribution from internal and external magnetic fields and performing crossover analysis to correct for navigational errors, we generated a high-resolution magnetic anomaly map for WR and RGR. These maps were used to improve the interpretation of magnetic anomalies over and around WR and RGR, as well as to investigate their tectonic history in the Late Cretaceous.

A major MAR reorganization occurred in South Atlantic during the Late Cretaceous between chrons C34n (83.6 Ma) and C30n (66.4 Ma). This reorganization was triggered by a shift in plate motions near the end of the Cretaceous Quiet Period, which caused a long-offset transform fault at the RG/FFZ to extend. This long-transform propagated southward, splitting split into smaller-offset transform faults by chron C30n (66.4 Ma) and normal spreading was restored in the South Atlantic. The updated magnetic anomaly patterns indicate that during this reorganization, a microplate was formed and between WR and RGR, prior to chron C34n and remained active for ~15 Myr until the end of chron C33n.

While the microplate was active, reconstructions show VB and RGR Massif forming simultaneously near the edges of the microplate. Around chron C33n, the eastern boundary of the microplate became extinct and full spreading started occurring at the western ridge, during which most of Centaurus Basin and E-RGR formed simultaneously on the South American and African plates respectively. At around C32n.1n, an eastward ridge jump occurred, incorporating E-RGR into the South American plate and regular spreading was resumed in the South Atlantic. This ridge jump has been mapped further south extending all the way to the 37°S FZ and transferred lithosphere formed during C34n-C33n from African plate to the South American plate. During anomaly C32n.1n, the long-offset transform located at an unnamed FZ located at 33°S, which after the ridge jump, split into several smaller-offset transforms in anomaly C30n.

This microplate and ridge reorganization hypothesis also explains other enigmatic tectonic features observed around WR and RGR such as curved fracture zones north of VB and age discontinuities across seamount chains in Guyot province. While the microplate was active, it experienced ~10° clockwise rotation due to differential spreading across the boundaries from ridge propagation, forming a V-shaped anomaly pattern and curved fracture zones to the west of Valdivia Bank. Spreading-parallel ridges found to the south of VB, formed as the ridge jumped westward during the late Cretaceous transferring lithosphere to RGR. The age discontinuity across the Tristan seamount chain, is a result of ridge propagation during this reorganization.

3.7 Bibliography

Alken, P., Thébault, E., Beggan, C. D., Amit, H., Aubert, J., Baerenzung, J. (2021). International geomagnetic reference field: the thirteenth generation. Earth, Planets and Space, 73(1), 1–25.

Bird, R. T., Naar, D. F., Larson, R. L., Searle, R. C., & Scotese, C. R. (1998). Plate tectonic reconstructions of the Juan Fernandez microplate: Transformation from internal shear to rigid rotation. Journal of Geophysical Research: Solid Earth, 103(B4), 7049–7067.

Bird, D. E., & Hall, S. A. (2010). South Atlantic kinematics and the evolution of Tristan da Cuhna hotspot tracks. 72nd EAGE Conference and Exhibition incorporating SPE EUROPEC 2010, cp-161. European Association of Geoscientists & Engineers.

Bird, D. E., & Hall, S. A. (2016). Early seafloor spreading in the South Atlantic: new evidence for M-series magnetochrons north of the Rio Grande Fracture Zone. Geophysical Journal International, 206(2), 835–844.

Camboa, L. A. P., & Rabinowitz, P. D. (1984). The evolution of the Rio Grande Rise in the southwest Atlantic Ocean. Marine Geology, 58(1–2), 35–58.

Cande, S. C., LaBrecque, J. L., & Haxby, W. F. (1988). Plate kinematics of the South Atlantic: Chron C34 to present. Journal of Geophysical Research: Solid Earth, 93(B11), 13479–13492.

Coffin, M. F., & Eldholm, O. (1994). Large igneous provinces: crustal structure, dimensions, and external consequences. Reviews of Geophysics, 32(1), 1–36.

Dessler, A. J., & Fejer, J. A. (1963). Interpretation of Kp index and M-region geomagnetic storms. Planetary and Space Science, 11(5), 505–511.

Estep, J., Reece, R., Kardell, D. A., Perez, N. D., Christeson, G. L., & Carlson, R. L. (2020). Intraplate deformation of oceanic crust near the Rio Grande Rise in the South Atlantic. Tectonophysics, 790, 228543.

Foulger, G. R. (2007). The “Plate” model for the genesis of melting anomalies. Special Papers-Geological Society of America, 430, 1.

Gamboa, L. A. P., & Rabinowitz, P. D. (1981). The Rio Grande fracture zone in the western South Atlantic and its tectonic implications. Earth and Planetary Science Letters, 52(2), 410–418.

Gee, J. S., & Kent, D. V. (2007). Source of oceanic magnetic anomalies and the geomagnetic polarity time scale.

Gerya, T. (2012). Origin and models of oceanic transform faults. Tectonophysics, 522, 34–54.

Graça, M. C., Kusznir, N., & Stanton, N. S. G. (2019). Crustal thickness mapping of the central South Atlantic and the geodynamic development of the Rio Grande Rise and Walvis Ridge. Marine and Petroleum Geology, 101, 230–242.

Hall, S. A., Bird, D. E., McLean, D. J., Towle, P. J., Grant, J. V., & Danque, H. A. (2018). New constraints on the age of the opening of the South Atlantic basin. Marine and Petroleum Geology, 95, 50–66.

Heirtzler, J. R., Dickson, G. O., Herron, E. M., pitman, W. C., III, & Le Pichon, X. (1968). Marine magnetic anomalies, geomagnetic field reversals, and motions of the ocean floor and continents. Journal of Geophysical Research, 73(6), 2119–2136.

Huang, Y., Sager, W. W., Zhang, J., Tominaga, M., Greene, J., & Nakanishi, M. (2021). Magnetic anomaly map of Shatsky Rise and its implications for oceanic plateau formation. Journal of Geophysical Research: Solid Earth, 126(2), e2019JB019116.

Jokat, W., & Reents, S. (2017). Hotspot volcanism in the southern South Atlantic: Geophysical constraints on the evolution of the southern Walvis Ridge and the Discovery Seamounts. Tectonophysics, 716, 77–89.

Koppers, A. A. P., Becker, T. W., Jackson, M. G., Konrad, K., Müller, R. D., Romanowicz, B., Whittaker, J. M. (2021). Mantle plumes and their role in Earth processes. Nature Reviews Earth & Environment, 2(6), 382–401.

Lonsdale, P. (1988). Structural pattern of the Galapagos microplate and evolution of the Galapagos triple junctions. Journal of Geophysical Research: Solid Earth, 93(B11), 13551–13574.

Matthews, K. J., Maloney, K. T., Zahirovic, S., Williams, S. E., Seton, M., & Mueller, R. D. (2016). Global plate boundary evolution and kinematics since the late Paleozoic. Global and Planetary Change, 146, 226–250.

Meyer, B., Chulliat, A., & Saltus, R. (2017). Derivation and error analysis of the earth magnetic anomaly grid at 2 arc min resolution version 3 (EMAG2v3). Geochemistry, Geophysics, Geosystems, 18(12), 4522–4537.

Mohriak, W. U., Nóbrega, M., Odegard, M. E., Gomes, B. S., & Dickson, W. G. (2010). Geological and geophysical interpretation of the Rio Grande Rise, south-eastern Brazilian margin: extensional tectonics and rifting of continental and oceanic crusts. Petroleum Geoscience, 16(3), 231–245.

Morgan, W. J. (1971). Convection plumes in the lower mantle. Nature, 230(5288), 42–43.

Müller, R. D., Seton, M., Zahirovic, S., Williams, S. E., Matthews, K. J., Wright, N. M. (2016). Ocean basin evolution and global-scale plate reorganization events since Pangea breakup. Annual Review of Earth and Planetary Sciences, 44, 107–138.

Naar, D. F., & Hey, R. N. (1991). Tectonic evolution of the Easter microplate. Journal of Geophysical Research: Solid Earth, 96(B5), 7961–7993.

O'Connor, J. M., & Duncan, R. A. (1990). Evolution of the Walvis Ridge-Rio Grande Rise hotspot system: Implications for African and South American plate motions over plumes. Journal of Geophysical Research: Solid Earth, 95(B11), 17475–17502.

O'Connor, J. M., & Jokat, W. (2015a). Age distribution of Ocean Drill sites across the Central Walvis Ridge indicates plate boundary control of plume volcanism in the South Atlantic. Earth and Planetary Science Letters, 424, 179–190.

O'Connor, J. M., & Jokat, W. (2015b). Tracking the Tristan-Gough mantle plume using discrete chais of intraplate volcanic centers buried in the Walvis Ridge. Geology, 43(8), 715–718.

Ogg, J. G. (2012). Geomagnetic polarity time scale. In F. M. Gradstein, J. G. Ogg, M. Schmitz, G. Ogg (Eds.), The geologic time scale 2012 (pp. 85–113).

Pérez-Díaz, L., & Eagles, G. (2017). A new high-resolution seafloor age grid for the S outh A tlantic. Geochemistry, Geophysics, Geosystems, 18(1), 457–470.

Richards, M. A., Duncan, R. A., & Courtillot, V. E. (1989). Flood basalts and hot-spot tracks: plume heads and tails. Science, 246(4926), 103–107.

Sager, W. W., Huang, Y., Tominaga, M., Greene, J. A., Nakanishi, M., & Zhang, J. (2019). Oceanic plateau formation by seafloor spreading implied by Tamu Massif magnetic anomalies. Nature Geoscience, 12(8), 661–666.

Sager, W. W., Thoram, S., Engfer, D. W., Koppers, A. A. P., & Class, C. (2021). Late Cretaceous Ridge Reorganization, Microplate Formation, and the Evolution of the Rio Grande Rise-Walvis Ridge Hotspot Twins, South Atlantic Ocean. Geochemistry, Geophysics, Geosystems, 22(3), e2020GC009390.

Saunders, A. D., England, R. W., Reichow, M. K., & White, R. V. (2005). A mantle plume origin for the Siberian traps: uplift and extension in the West Siberian Basin, Russia. Lithos, 79(3–4), 407–424.

Seton, M., Müller, R. D., Zahirovic, S., Gaina, C., Torsvik, T., Shephard, G. (2012). Global continental and ocean basin reconstructions since 200 Ma. Earth-Science Reviews, 113(3–4), 212–270.

Seton, M., Whittaker, J. M., Wessel, P., Müller, R. D., DeMets, C., Merkouriev, S. (2014). Community infrastructure and repository for marine magnetic identifications. Geochemistry, Geophysics, Geosystems, 15(4), 1629–1641.

Thoram, S., Sager, W. W., & Jokat, W. (2019). Implications of updated magnetic anomalies for the Late Cretaceous tectonic evolution of Walvis Ridge. Geophysical Research Letters, 46(16), 9474–9482.

Tozer, B., Sandwell, D. T., Smith, W. H. F., Olson, C., Beale, J. R., & Wessel, P. (2019a). Global bathymetry and topography at 15 arc sec: SRTM15+. Earth and Space Science, 6(10), 1847–1864.

Wessel, P., Luis, J. F., Uieda, L., Scharroo, R., Wobbe, F., Smith, W. H. F., & Tian, D. (2019). The generic mapping tools version 6. Geochemistry, Geophysics, Geosystems, 20(11), 5556–5564.

Whittaker, J. M., Afonso, J. C., Masterton, S., Müller, R. D., Wessel, P., Williams, S. E., & Seton, M. (2015). Long-term interaction between mid-ocean ridges and mantle plumes. Nature Geoscience, 8(6), 479–483.

Wilson, J. T. (1973). Mantle plumes and plate motions. Tectonophysics, 19(2), 149–164.

CHAPTER 4

IMPROVED HIGH-RESOLUTION BATHYMETRY MAP OF TAMU MASSIF AND SOUTHERN SHATSKY RISE AND ITS GEOLOGICAL IMPLICATIONS

4.1 Introduction

Oceanic plateaus are large basaltic constructions found in all major ocean basins and make up ~5% of the seafloor (Harris, 2014; Sager et al, 2011). Most of these Large Igneous Provinces (LIPs) are massive crustal emplacements believed to have formed by large scale mantle melting (Coffin and Eldholm, 1994), but the mechanism underlying their formation is not well understood. The Mantle Plume hypothesis has been widely used to explain plateau formation, attributing melting to the surfacing of a deep mantle thermal plume (Richards et al., 1989; Duncan and Richards, 1991; Campbell, 2005). An alternative idea explains the massive eruptions through decompression melting of fertile (low melting point) upper mantle material (Anderson et al. 1992; Saunders 2005; Foulger, 2007). Some researchers have noted that oceanic plateaus commonly form at spreading ridges and triple junctions, suggesting a strong link between ridge volcanism and plume volcanism (Whittaker et al., 2015; Sager, 2007; Sager et al., 2019).

Whatever mechanism led to the formation of oceanic plateaus; their subsequent evolution is not completely understood. At its simplest incarnation, these plateaus of excess material should cool and subside with the lithosphere while being buried by a drape of pelagic sedimentation. Because their summits often rise above the Carbonate Compensation Depth (CCD), thick carbonate sediment caps may accumulate (e.g., Sliter and Brown, 1993). Plateaus can also come back to life, volcanically speaking, rejuvenated with small-volume volcanism after tens of millions of years quiescence (Lonsdale et al., 1993; Pietsh et al., 2015; Hanyu et al., 2017; Hirano et al., 2017; Homrighausen et al., 2019; O'Connor et al., 2015). Since these oceanic plateaus are usually large and present in remote locations, most such inferences about plateau formation and evolution are based on scant data and not completely accurate.

The geomorphology of oceanic plateaus reflects their formation processes, but most of the available bathymetric data is rudimentary owing to the difficulty of surveying large undersea features, which results in a sparse distribution of high-resolution data. Multibeam echosounder (MBES) data have become more widespread and provide several orders of magnitude improvement in horizontal topographic resolution and therefore have the potential to provide important clues about plateau formation.

Shatsky Rise is an oceanic plateau located ~1600 km east of Japan in northwest Pacific (Figure 4.1). Tamu Massif is the largest mountain of this plateau and makes up most of the southern part of the plateau. An extensive multibeam bathymetry survey was conducted over Tamu Massif onboard R/V Falkor during our research expedition (FK151005) in 2015. In addition, 7 previously unavailable cruises' data were acquired from the Japan Agency for Marine-Earth Science and Technology (JAMSTEC). By merging the new data with the existing MBES data and SRTM15+ global bathymetry model (Tozer et al., 2019), a new high-resolution bathymetry map of Tamu Massif and environs was generated to reveal important geological clues about its formation and evolution. The high-resolution bathymetry reveals that the Tamu Massif flanks are segmented, with the main plateau flanked by four lower rises separated by subdued troughs. In addition, the map reveals new clues about the evolution of the sediment cover and secondary volcanism.

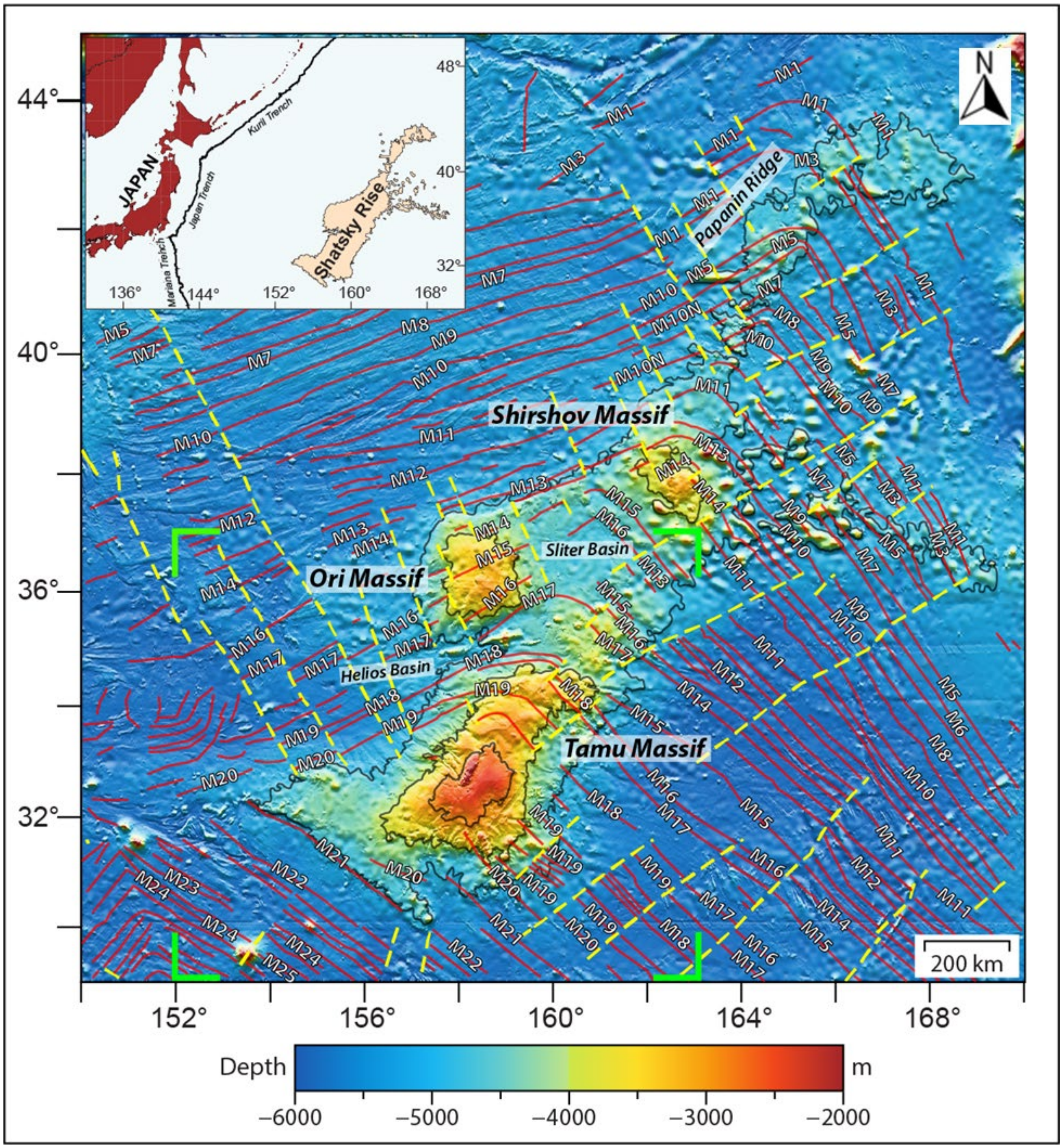

Figure 4.1 – Shatsky Rise bathymetry and feature names. Red lines are magnetic lineations and yellow dashed lines are fracture zones (Nakanishi et al., 1999). Background is SRTM15+ predicted bathymetry (Tozer et al., 2019). Contours are drawn at 1000 m intervals, but only 3000 m – 5000 m depth contours are shown. Inset shows Shatsky Rise location relative to Japan and western Pacific trenches. Green corner marks show the extent of the study area.

4.1.1 Development of Shatsky Rise Bathymetry Maps

The interpretation of Shatsky Rise morphology has evolved on bathymetry maps with improvements in sounding techniques. Although it is a feature covering a large area, it did not appear on the earliest bathymetry maps because soundings were few and far between. The first edition GEBCO map (1903) had a mountain in nearly the same location as Tamu Massif, but this appears to have been based on a vigia (a navigational hazard whose existence and position is uncertain). This feature appears to be the location of Ganges Island, a phantom island which appeared on 19th century nautical charts. This misinterpretation was bolstered by slightly shallower soundings along a track of the HMS Challenger that trended E-W across northern Shatsky Rise at the latitude of central Japan. This feature was retained on several bathymetry compilations of the late 19th and early 20th century, including the Summary of the Challenger Expedition (Quackenbos and Dall, 1887; Supan, 1899; Murray, 1995; 1899; Groll, 1912). But Ganges Island was removed from the 2nd edition GEBCO map (1912).

The actual Shatsky Rise appeared as an elongated elevation with a trend of ~N45°E on bathymetric charts prepared by the International Hydrographic Bureau and US Navy Hydrographic Office in 1939. This appearance was the result of US Navy sounding lines collected by newly deployed electronic echo sounders. Although Menard's (1959) review of Pacific geology did not show the feature, it appeared a few years later on the bathymetry map in his book *Marine Geology of the Pacific* (Menard, 1964). At the same time, Udintsev et al. (1960; 1964) published a bathymetry chart in the Soviet Union with greater detail based on cruises 25, 26, 28, and 30 of the R/V *Vityaz* along with other public data. In the 1964 version, Udtinsev et al. named Shatsky Rise after Russian geologist Nicolay Sergeyevich Shatsky (1895-1960).

Resolution of morphology improved with greater numbers of scientific cruises. All major bathymetric features were recognized in the Mammerickx and Smith (1984) bathymetry map. The acme of single-beam echosounder maps was the compilation of Sager et al. (1999), which also published the first MBES data, but only in small, selected areas where limited-area surveys were done. MBES data were included in updates of the Smith and Sandwell (1997) satellite altimetry-predicted bathymetry data sets, but at low resolution owing to 1-min grid size. Zhang et al. (2016) developed the first large-scale multibeam map of Shatsky Rise by merging MBES data with predicted bathymetry to fill gaps. High resolution provided by Multibeam-echosounder data showed many small features that were not resolved by prior mapping.

4.1.2 Geologic Setting

Shatsky Rise is a large oceanic plateau in the northwest Pacific Ocean ~450 km in width and 1650 km in length (Figure 4.1; Sager et al., 1999). It is situated on Jurassic-Early Cretaceous abyssal seafloor ~5000-6000 m deep. Shatsky Rise is comprised of three primary volcanic mountains – Tamu Massif, Ori Massif, and Shirshov Massif (Sager et al, 1999). At the southwest end of the Shatsky Rise lies the Tamu Massif, the largest and the oldest edifice with an area of ~315,000 km^2, roughly the size of U.S. state of New Mexico or the British Isles. Shatsky Rise continues to the N and NE with Ori and Shirshov Massifs. Ori Massif is separated from Tamu Massif by narrow, rectangular Helios basin (~100 km wide). Ori Massif is a subrounded mountain that is smaller than Tamu Massif with a diameter of ~250-300 km. Shirshov Massif is a somewhat smaller mountain, elongated NW-SE, with long axis of ~250 km, located northeast of Ori Massif with Sliter Basin (~160-220 km wide) separating it from Tamu and Ori Massifs. Low, linear Papanin Ridge extends ~700 km northeast from Shirshov Massif. Ojin Rise seamounts are located in eastern Sliter Basin and extend east of Shirshov Massif into the abyssal plain between Shatsky Rise and the Emperor Seamounts (Sager et al., 1999; Tejada et al., 2016).

All the main edifices have a flat domal shapes with low slopes. Tamu Massif is a rounded dome elongated SW-NE, with gentle flank slopes mostly <1° (Sager et al., 1999; 2013). The main summit is near ~32.6°N, 158.6°E and is ~2500 m in depth at the top of a Cretaceous sediment pile ~1.2 km in thickness (Sager et al, 1999; Clark et al., 2018). It reaches a shallowest depth of ~1950 m atop a steep-sided summit ridge, Toronto Ridge (Zhang et al., 2016). Ori Massif summit is near ~36°N, 158.5°E and has a minimum depth slightly above 3000 m at which the sediment thickness is variable but reaches a maximum of ~800 m (Klaus and Sager 2002; Zhang et al. 2015). Shirshov Massif has its summit near 38°N, 162.5°E with a minimum depth slightly <3000 m. It is covered by a pelagic sediment cap which reaches a maximum thickness of ~1 km (Sager et al., 1999). On all massifs, sediment caps thin outward from the center and are typically of variable thickness up to a few hundred meters on the flanks (Clark et al., 2018).

4.1.3 Geologic History and Evolution

Shatsky Rise mostly formed during Late Jurassic and Early Cretaceous time near the equator and the center of the Panthalassa basin (Sager et al., 2015; Seaton et al., 2012; Torsvik et al., 2019). It is surrounded by two sets of nearly perpendicular magnetic lineations with anomalies ranging from M21 (~149 Ma) to M1 (~126 Ma) (time scale of Ogg (2012) is used here for anomaly ages). The Japanese lineations trend SW-NE whereas the Hawaiian lineations trend NW-SE, indicating that two ridges met at the Pacific-Farallon-Izanagi triple junction (Larson and Chase, 1972; Hilde et al., 1976; Sager et al., 1988; Nakanishi et al., 1989; 1999). Prior to M21, the triple junction moved northwest relative to the Pacific plate, but around chron M22, it jumped ~800 km eastward to the location of Tamu Massif and started moving northeastward

(Sager et al. 1988; Nakanishi et al., 2015). Based on irregularities in the magnetic anomaly pattern, the triple junction jumped northeast at least 9 more times (Nakanishi et al.,1999; 2015) as Shatsky Rise formed along its path.

After initial formation, Tamu Massif was mostly quiescent except for the formation of secondary cones. Toronto Ridge, the largest such feature, is ~1 km in height (Sager et al., 1999) and formed ~17 Myr after the main edifice (Heaton and Koppers, 2014). After volcanism stopped, Tamu Massif drifted northward ~35° with the Pacific plate (Sager et al., 2015). It collected a thick cap of mainly tropical pelagic carbonate sediments, up to ~1.2 km thick (Sager et al., 1999; Clark et al, 2018), as it drifted from the equator into the central gyre. Reliable $^{40}Ar/^{39}Ar$ radiometric dates have been determined from basalt samples cored at two sites on Tamu Massif: 144.6 ± 0.8 Ma for Site 1213 on the south flank and ~143-145 Ma for Site U1347 on the southeast upper flank (Geldmacher et al., 2014; Heaton and Koppers, 2014). These ages coincide with the age of anomaly M19 (~145 Ma), which bounds the north side of Tamu Massif. This coincidence implies that Tamu Massif formed during a short period near the ridge crest (Heaton and Koppers, 2014). In contrast, secondary volcanism may have extended over millions of years after the main Tamu Massif formation. Many secondary cones are found on the flanks of Tamu Massif and they imply later volcanism (Zhang et al., 2016), although only Toronto Ridge has been dated, so their timing is unknown.

Seismic reflection lines over Tamu Massif show parallel intrabasement reflectors conformal to the surface with no major secondary source other than the main summit suggesting that Tamu Massif is a large, single volcano (Sager et al.,2013). Sager et al. (2019) traced linear magnetic anomalies, which are a signature of ridge formation, within Tamu Massif implying that Tamu Massif formed via seafloor spreading.

4.2 Data and Methods

We combined newly acquired MBES data with previously available MBES data over southern Shatsky Rise and merged them with the SRTM15+ global bathymetry model (Tozer et. al, 2019) to generate an updated bathymetry map of Tamu Massif and environs (Figure 4.2). This combination is necessary despite the large number of MBES cruises available because wide gaps still remain between high resolution data in many places.

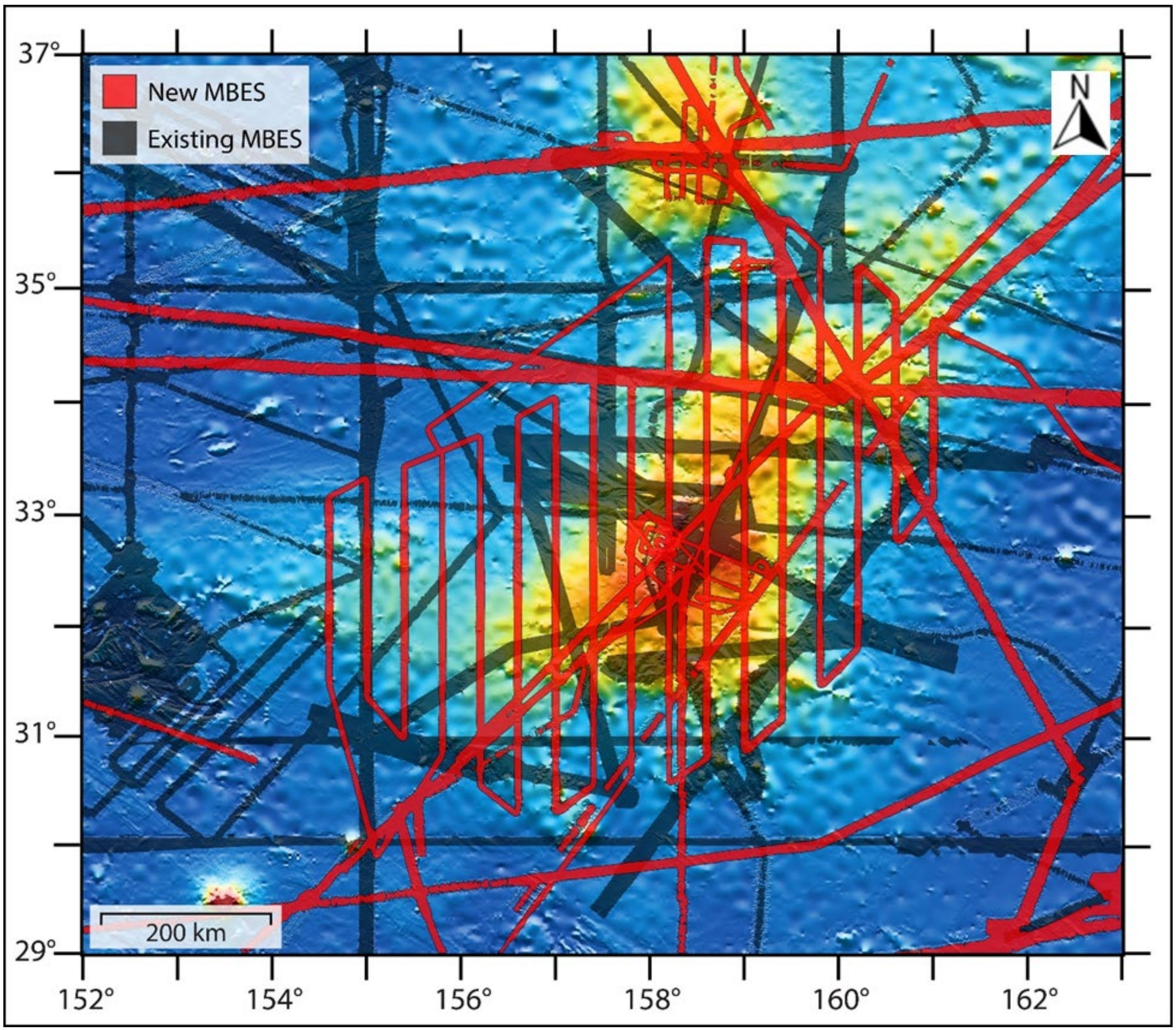

Figure 4.2 – MBES coverage in the study area. Red swaths represent newly added MBES data. Dark gray swaths represent prior MBES data. Background is SRTM15+ predicted bathymetry (Tozer et al., 2019). List of cruises given in Table 2.1.

Table 4.1 – MBES surveys over southern Shatsky Rise used in this study

Cruise ID	Ship	Year	Institution
TN037[¶]	*Thomas G. Thompson*	1994	Texas A&M University
MR98-K01	*Mirai*	1998	JAMSTEC
MR99-K04	*Mirai*	1999	JAMSTEC
MR00-K01	*Mirai*	2000	JAMSTEC
MR00-K08	*Mirai*	2000	JAMSTEC
EW0204[¶]	*Maurice Ewing*	2002	Lamont-Doherty Earth Observatory
MR01-K03	*Mirai*	2001	JAMSTEC
MR02-K01	*Mirai*	2002	JAMSTEC
MR02-K06 Leg 34	*Mirai*	2002	JAMSTEC
MR03-K01	*Mirai*	2003	JAMSTEC
KR03-10	*Kairie*	2003	JAMSTEC
KH-03-1 Leg1	*Hakuho Maru*	2003	The University of Tokyo
MR04-02	*Mirai*	2004	JAMSTEC
MR04-04	*Mirai*	2004	JAMSTEC
MR04-06	*Mirai*	2004	JAMSTEC
MR04-07	*Mirai*	2004	JAMSTEC
MR05-01	*Mirai*	2005	JAMSTEC
KH-05-4*	*Hakuho Maru*	2005	The University of Tokyo
MR06-03 Leg2*	*Mirai*	2006	JAMSTEC
MR07-01	*Mirai*	2007	JAMSTEC
MR07-05	*Mirai*	2007	JAMSTEC
KR07-06	*Kairie*	2007	JAMSTEC
MR08-06 Leg1*	*Mirai*	2008	JAMSTEC
YK08-09	*Yokosuka*	2008	The University of Tokyo
MGL1004[¶]	*Marcus G. Langseth*	2010	Lamont-Doherty Earth Observatory
KR11-10	*Kairie*	2011	JAMSTEC
MGL1206	*Marcus G. Langseth*	2012	Lamont-Doherty Earth Observatory
MV1305[¶]	*Melville*	2013	Scripps Institution of Oceanography
KR14-06*	*Kairie*	2014	JAMSTEC
KR14-07*	*Kairie*	2014	JAMSTEC
KR1410*	*Kairie*	2014	JAMSTEC
FK151005*	*Falkor*	2015	Schmidt Ocean Institute

*Cruises not used in SRTM15+ (Tozer et al., 2019). [¶]Denotes data from NCEI archive. NCEI=National Center for Environmental Information; JAMSTEC=Japan Agency for Marine-Earth Science and Technology.

A total of ~6 x 10^6 new depth soundings were collected over Tamu Massif during 2015 by R/V *Falkor* cruise FK151005. These data were collected using a hull mounted Kongsberg EM302 Multibeam-echosounder, which operates at 30 kHz frequency. During FK151005, we achieved a swath width between 8-10 km most of the time. In addition, we acquired another ~17 x 10^6 soundings from 6 JAMSTEC MBES cruises that were previously unavailable. With the addition of these new MBES data, ~64% of Tamu Massif above 4000 m contour is covered. This is the densest coverage over Shatsky Rise (Figure 4.2). The rest of the map area is covered ~38 % by MBES data. Although these new soundings significantly improve the coverage over Tamu Massif, there are still large gaps between MBES swaths, especially over the Shatsky Rise flanks and adjacent abyssal plains. Data gaps were filled using the SRTM15+ v2.1 (released in February 2020) global bathymetry model. SRTM15+ is a 15-arc sec resolution bathymetry grid generated by merging predicted bathymetry from satellite altimetry-derived gravity calibrated with ship soundings.

Although archived high resolution (100 m- 250 m) MB data were incorporated into the SRTM15+ model, much of the resolution is lost owing to the 15-arc sec grid size. Moreover, some archival tracks (e.g., EW0204, MR05-01) appear to have incorrect velocity corrections, creating along track artifacts in the bathymetry map. Errors in sound velocity profiles used to correct the data can cause the outer beams to bend up near the swath edge. Some of the older MBES cruises used in the SRTM15+ model appear to have roll or heave artifacts due to errors in acquisition or processing. To address the resolution issue, a higher resolution depth grid was created to replace SRTM15+ data wherever MB data were available. To address processing issues, we examined and reprocessed existing MBES data wherever possible.

In total, 32 MB cruises spanning >25 years (Table 4.1) with >70 x10^6 soundings were used in our compilation (7 of the cruises were not used in the SRTM15+ model). We were able to acquire raw data for 8 prior MBES cruises from the National Centers for Environmental Information (NCEI) database. These data along with the newly acquired data from the FK15005 cruise were processed using Caris HIPS and SIPS software. Raw data were imported into the HIPS and SIPS software and a sound velocity correction was performed. For cruises where sound velocity profiles were available, we applied those profiles. Otherwise, a constant water sound velocity of 1500 ms^{-1} was applied to the soundings. Erroneous soundings were removed using the HIPS and SIPS swath and subset editor. Soundings were rejected based on departure from apparent geological surfaces, for example, sharp spikes or isolated discordant soundings and clean depth soundings were exported. For the remaining 17 cruises (Table 4.1), we could not reprocess the data because the necessary raw data were not available.

To generate a 100 m resolution merged bathymetry grid, a remove-interpolate-restore gridding method similar to that used in generating the SRTM models (Becker et al., 2009; Tozer et al., 2019) was followed. A deviation from this process is the way we handled MBES soundings. SRTM15+ contains a merger of all MBES soundings with no differentiation between good and poor-quality data. When combining soundings from different cruises, artifacts from one cruise can affect better data in regions where multiple tracks overlap. Even one bad swath will corrupt the intersecting good data swaths. This is especially true for the MBES cruises that have artifacts but could not be reprocessed. To solve this issue, wherever better data swaths crossed problematic data, the poor data were removed. This procedure resulted in fewer artifacts.

Gridding was done using GMT software (Wessel et al., 2019). The gridding process started with resampling the SRTM15+ model onto a 100 m pixel registered grid using the GMT routine *grdsample*. MBES soundings were averaged at 100 m intervals and then gridded using GMT routines *blockmedian* and *surface*. Subsequently SRTM15+ depth points were replaced with the MBES depths at grid nodes where the data sets coincide. This was done by subtracting the resampled SRTM15+ depth grid from the MBES depth grid to produce a residual depth grid. This residual grid was then added to 100 m sampled SRTM15+ grid get the final depth grid.

At the edges of MBES swaths, where MBES and SRTM15+ depth values are adjacent, sometimes these values do not agree. This is caused by the fact that the SRTM15+ data are a model estimation where there are no bathymetry data. This difference creates an abrupt offset at some edges of the MBES swaths. To reduce this effect, a smoothing function was applied at the edges of the MBES data by creating a 10 km buffer with no data around the MBES data and allowing the gridding algorithm to smooth the transition to the SRTM15+ data.

In addition to bathymetry data, we also used 2D seismic reflection data collected over Tamu Massif during cruises TN037 (Klaus et al., 2002), MGL1004, and MGL1206 (Zhang et al., 2015) to aid in the morphological interpretation. These seismic data were examined using IHS Kingdom software and interpreted using standard seismic stratigraphy techniques (Mitchum et al. 1977).

4.3 Results

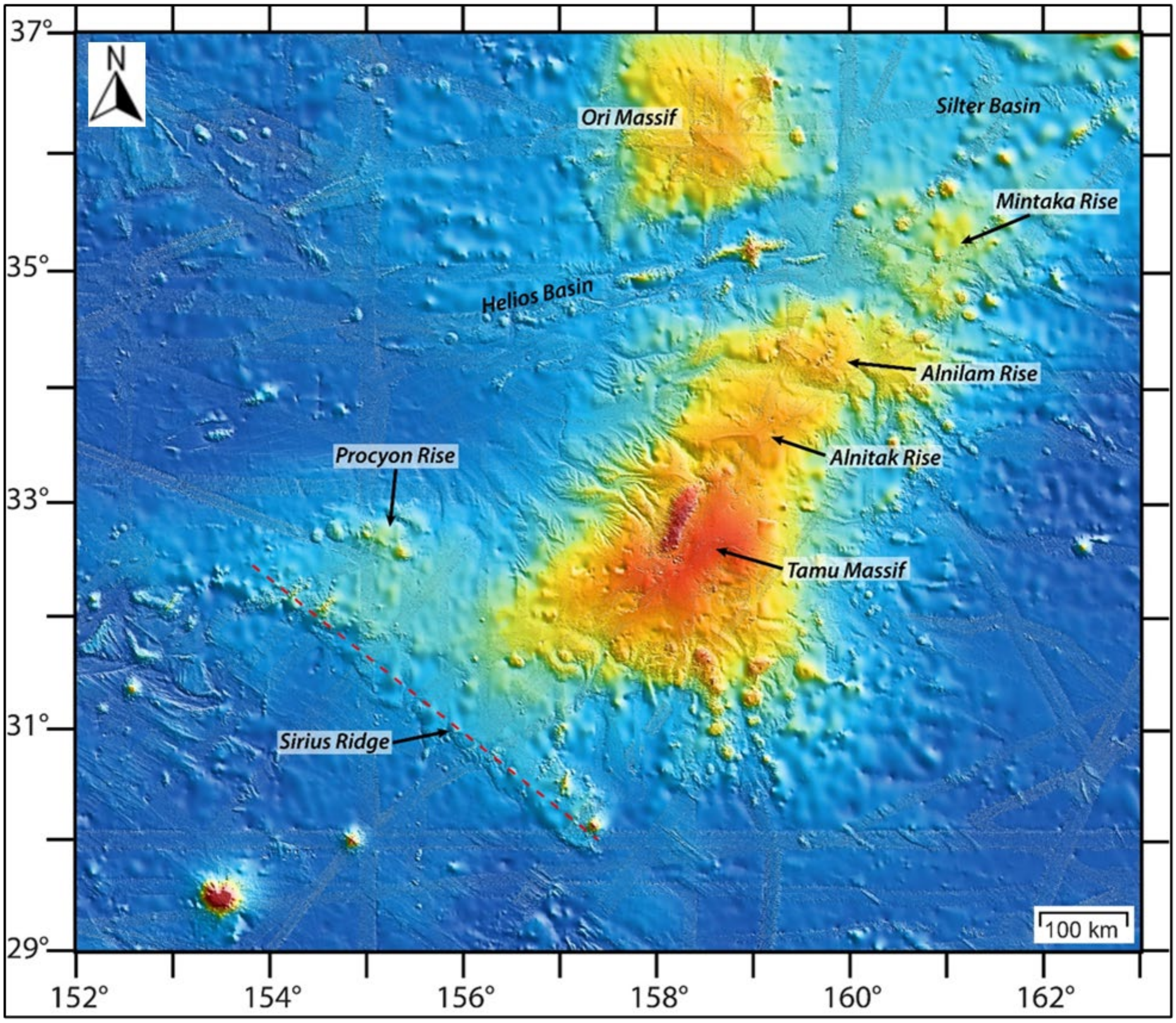

Figure 4.3 – Shaded bathymetry map of southern Shatsky Rise. Labels give feature names. Red dashed line shows the trend and lateral extent of Sirius Ridge. Color scale same as Figure 4.1.

The updated map shows the broad bathymetric swells of Tamu and Ori Massif over southern Shatsky Rise separated by the narrow Helios basin (Figure 4.3). Tamu Massif is a large subrounded dome, elongated along a SW-NE axis and is ~800 km long with width (at the 5000 m depth contour), narrowing from ~400 km at its SW end to ~100 km at its NE end. It has a broad domal summit reaching a depth of ~2500 m. Ori Massif is a small, rounded dome to the north of Tamu Massif, ~240 km in diameter with summit reaching a depth of ~3000 m. Helios

Basin is a narrow rectangular basin ~100 km wide separating Ori from Tamu Massif and has an average depth of ~5000 m.

In addition to confirming the large-scale structure of southern Shatsky Rise, increased coverage with MBES data revealed many small-scale geomorphic features that are categorized into three groups – volcanic features (e.g., volcanic edifices, cones, ridges), tectonic features (e.g., faults), and sedimentary features (e.g., submarine canyons, slope failures). All these features have been discussed in subsequent sections.

4.3.1 Volcanic Features

The central dome of Tamu Massif is flanked by a linear ridge and a low rise to the west and southwest and three low rises over the northeast flank, separated by shallow valleys or troughs. These subdued troughs appear to segment the main massif into 5 smaller edifices – Sirius Ridge and Procyon Rise on the southwest end and Alnitak Rise, Alnilam Rise, and Mintaka Rise on the northeast end (Figure 4.3).

Sirius Ridge is a linear ridge ~440 km long and ~60 km wide trending ~N52°E. It has a top depth of ~4800 m and is bounded by a steep escarpment with a relief of ~600 m in places along its southwest margin. A bathymetric valley with a similar trend occurs on its north side. It separates the ridge from Procyon Rise at its northwest end. On its southeast end, this valley causes a deep re-entrant (~5500 m) in the south flank of Tamu Massif. At its middle, the ridge is connected to the main massif with no clear division. A seismic line across the ridge at this location shows no division between the ridge and the massif. Magnetic anomalies show M21 (~149 Ma) running along the length of the ridge, suggesting it to be a spreading related feature.

Procyon Rise is a small edifice southwest of Tamu Massif (Figure 4.3). It appears to be triangular in plain view with two somewhat linear zones of higher bathymetry. It has an area of ~ 3000 km^2 with the summit reaching a depth of ~3800 m. A broad valley, ~90 km wide and ~600 m deep, trending along ~N45°E separates the rise from Tamu Massif. Magnetic anomalies (Sager et al., 2019) over the rise show a positive anomaly, interpreted as M20, bounded by negative anomalies to the north and south, separating it from another broad positive anomaly M20 over center of Tamu Massif. This change in magnetic character and intervening valley suggest that Procyon Rise is a separate edifice disconnected from the main massif.

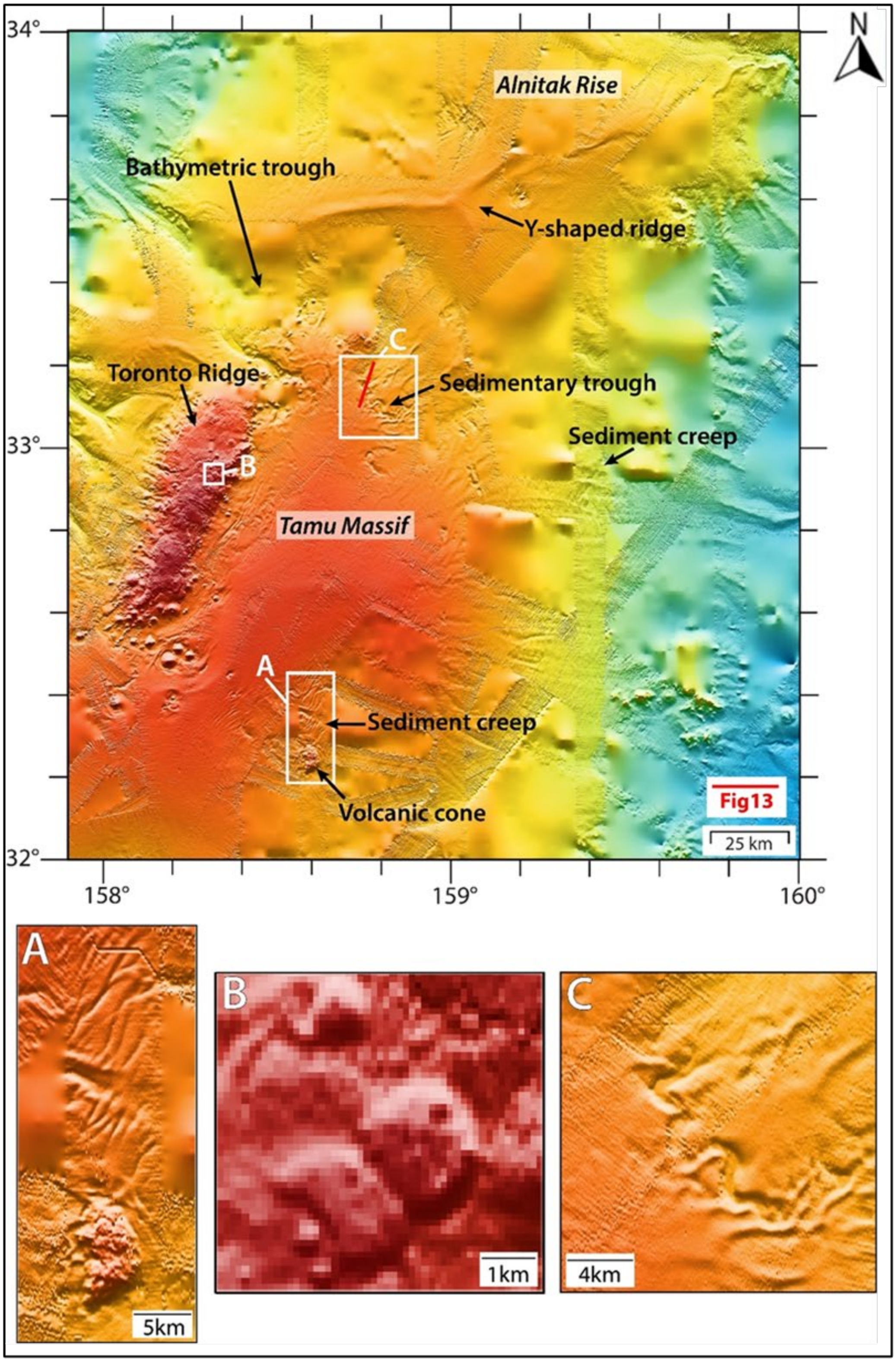

Figure 4.4 – Shaded relief bathymetry map for central Tamu Massif. (A-C) show details of features discussed in text. (A) Sediment creep folds. (B) Volcanic mounds atop Toronto Ridge. (C) Sinuous sedimentary trough. Locations shown in main figure. Color scale same as in Figure 4.1. Red line represents the seismic section shown in Figure 4.13.

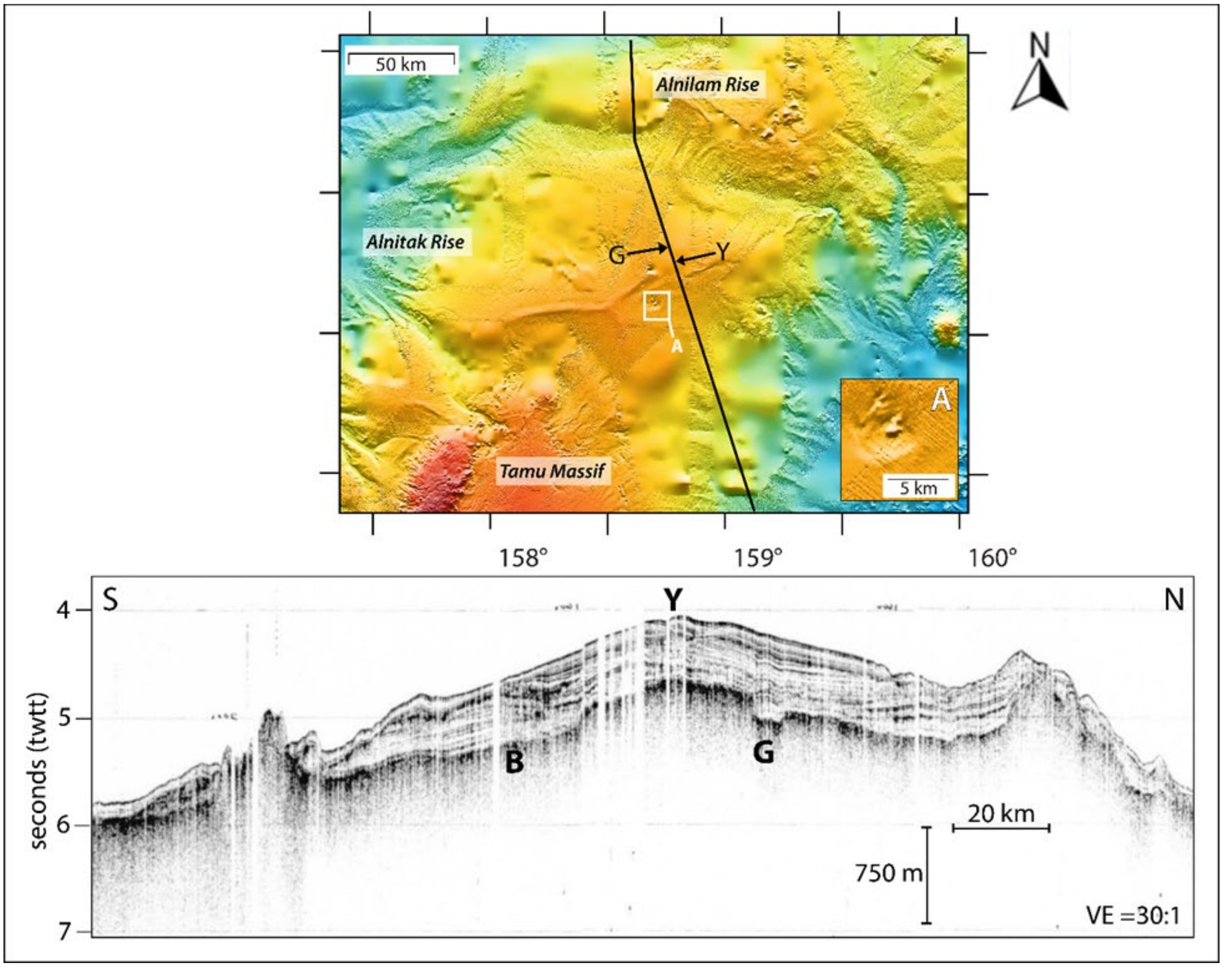

Figure 4.5 – Single-channel seismic profile showing basement structure under the north arm of the Y-ridge. Seismic section displays two-way travel-time in seconds (vertical axis) versus distance in km (horizontal axis). Heavy black lines on location map (top) shows profile location. Abbreviations: G, graben; Y, ridge; VE, vertical exaggeration. Seismic profile collected during cruise RC1008. (A) shows a sedimentary moat discussed in text.

Three more rises further segment the Tamu Massif northeast flank: Alnitak Rise, Alnilam Rise, and Mintaka Rise (Figure 4.3). Alnitak Rise is the southernmost of all and adjacent to the main Tamu Massif edifice. It has a trapezoidal shape with an area of ~14,725 km^2 and is separated from Tamu Massif by a subdued trough ~25 km wide and ~400 m deep. The trough has an inverted V-shape with the left trough trending ~N75°E and the right trough trending ~N45°W. This trough contains undulations at its center perhaps because of sediment erosion by currents. A distinct Y-shaped ridge (159.0°E, 33.6°N; Figure 4.4) is located at the Alnitak Rise summit where it reaches a shallowest depth of ~2900 m. Seismic data (Figure 4.5) reveals that the Y-ridge is sedimentary (discussed in the next section). To the NE, another inverted V-shaped trough ~480 m deep and ~17 km wide with arms trending N84°E (west) and N67°W (east) separates Alnitak Rise from Alnilam Rise, located farther north. Alnilam Rise has an ellipsoidal shape elongated along N72°W and has an area of ~16,465 km^2. Alnilam Rise is bounded on the northwest by Helios Basin, which trends ~N78°E and separates Alnilam Rise from Ori Massif. To the northeast, Alnilam Rise is separated from Mintaka Rise by a bathymetric trough trending ~N61°W. This trough is ~30 km wide and ~570 m deep. This trough forms an inverted-V shape with Helios Basin (Fig. 3). Mintaka Rise is a rounded dome ~180 km in diameter and forms the southeastern boundary of Helios Basin. It has an area of ~19,430 km^2 and the summit reaches a depth of ~3400 m.

High-resolution bathymetry shows a region of anomalous, curved seafloor fabric (153.5°E,31.5°N; Figure 4.3) west of Sirius Ridge. This feature was reported by Nakanishi et al. (2015), who interpreted it has having formed by reorganization of the Pacific-Izanagi-Farallon triple junction just prior to its jump to the northeast Tamu Massif.

Beside the large-scale volcanic features above, smaller features such as volcanic ridges, cones, and domes are found on all large edifices. At the western summit of Tamu Massif lies Toronto Ridge (Figure 4.4), a ~N20°E trending linear ridge ~75 km long and ~20 km wide. The ridge is ~1 km tall and has average slope of ~5°, which is steeper than the main edifice (Zhang et al., 2016).

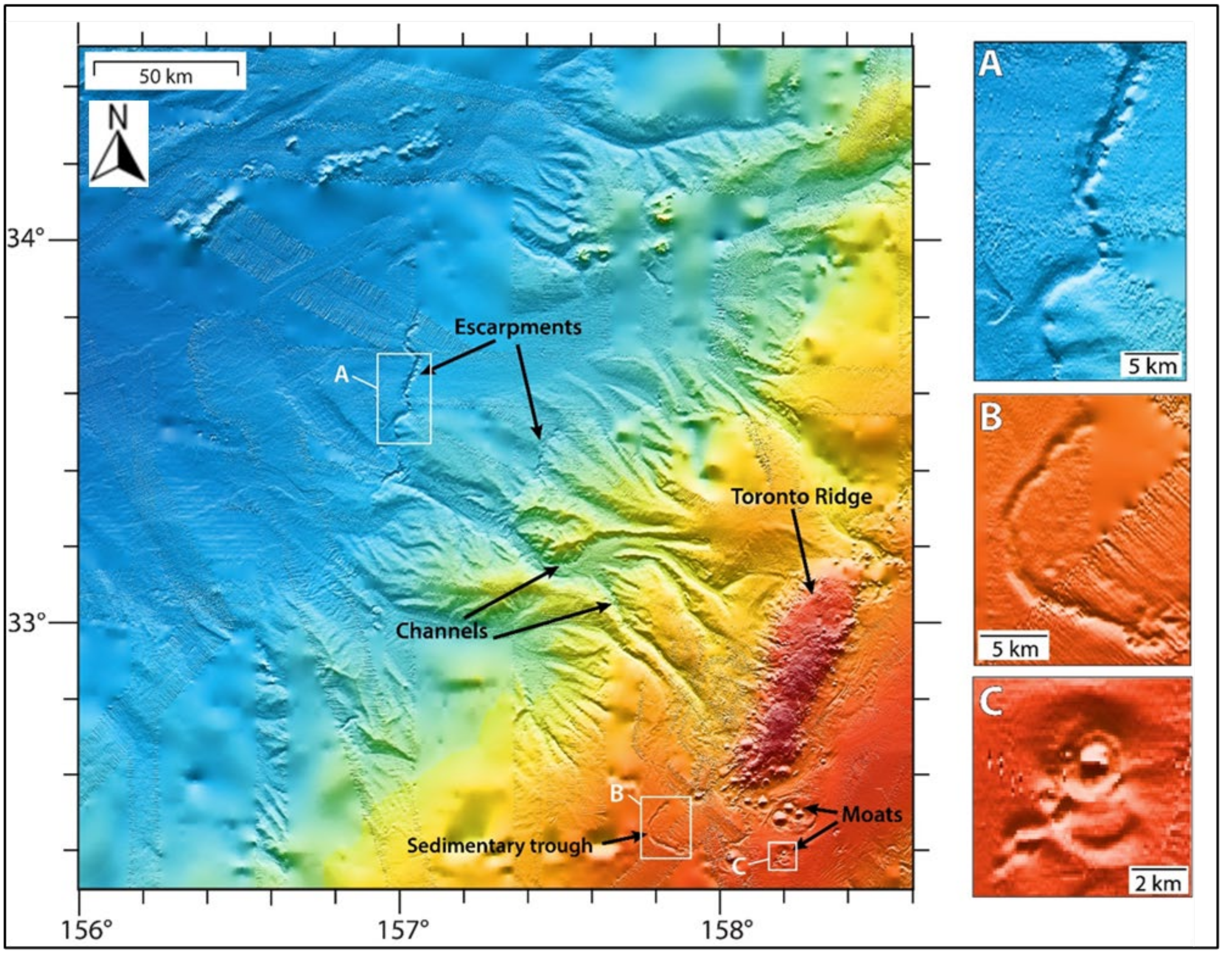

Figure 4.6 – Shaded relief bathymetry map of northwest Tamu Massif. (A-C) Details of features discussed in text. (A) Escarpment. (B) Curved sedimentary trough. (C) Cone summit with surrounding moat. Locations shown in main figure. Color scale is same as Figure 4.1.

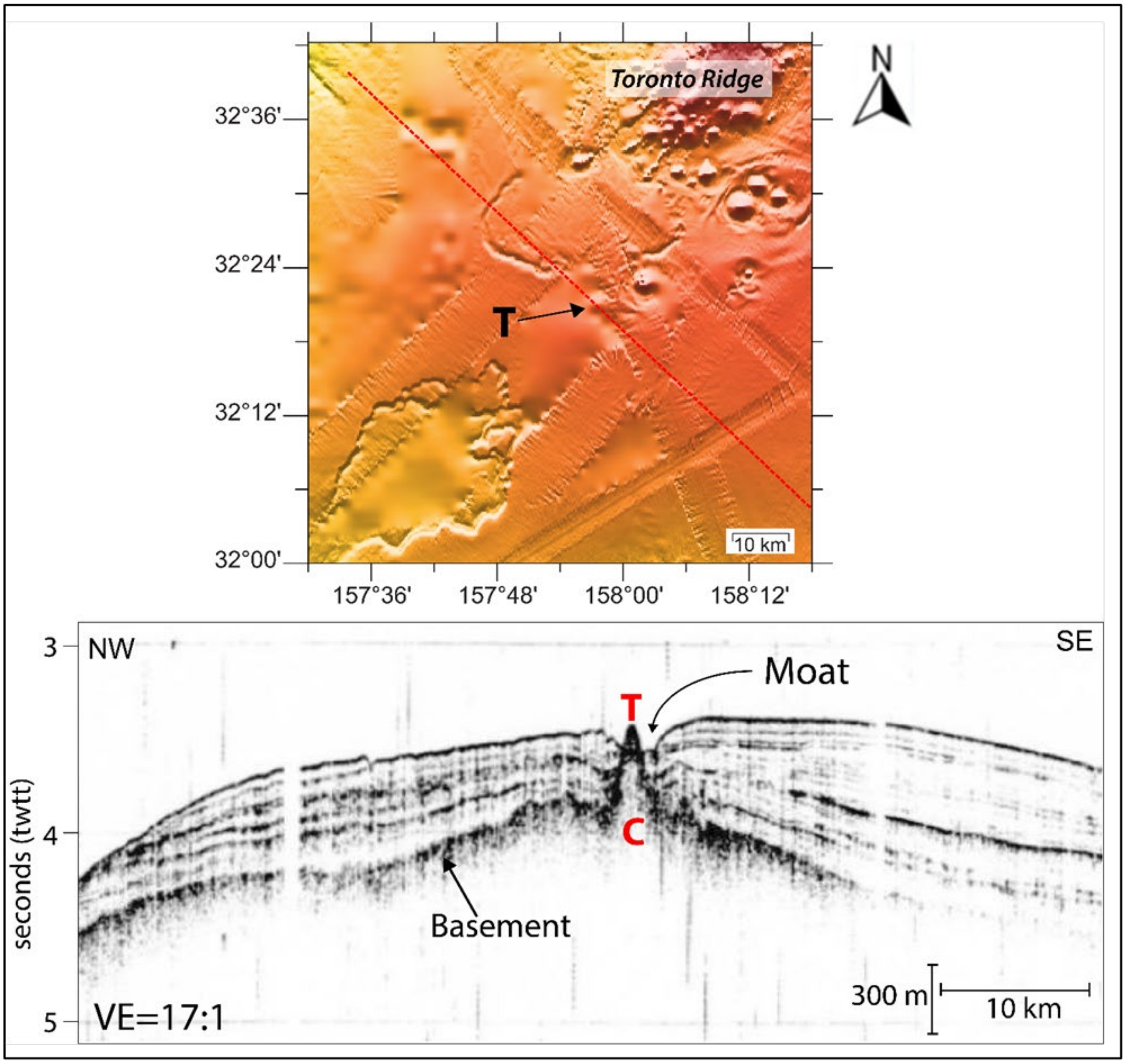

Figure 4.7 –Single-channel seismic profile over a secondary cone to the south of Toronto Ridge. Also shows is the moat around the cone. Seismic section displays two-way travel-time in seconds (vertical axis) versus distance in km (horizontal axis). Red dashed line on the map shows profile location. Abbreviations: T, exposed cone tip; C, cone; VE, vertical exaggeration. Seismic profile collected during cruise RC1007.

The top of Toronto Ridge has a hummocky texture characterized by many small mounds (Figure 4.4B) ~1-2 km in width and ~100 m in height. Many of these domes have shapes similar to pillow stacks mapped in seafloor eruptions over the Galapagos spreading center using near-bottom sonar systems (McClinton et al., 2013). In contrast, multiple pointed cones (e.g., 158.2°E, 32.5°N; Figures 4.4 & 4.6) are observed on the flanks and the surrounding region.

These cones are ~1-3 km in diameter and ~100-500 m in height above the sediment cap. The largest of these cones is ~5 km wide and ~650 m high and is part of a three-cone cluster located at the southeast perimeter of the ridge. A subcircular depression ("moats" Figure 4.6C) is observed in the sediments adjacent to some of these cones. A seismic profile over one of these cones (Figure 4.7) reveal the cone to be an exposed tip of a larger, partly buried volcanic cone emanating from the basement. The moats around the cones are described in the section on sedimentary features. Figures 4.4 and 4.5 of Clark et al. (2018) show two buried cones ~600 m and ~350 m in height near Toronto Ridge. These buried cones are probably part of the field of cones southeast of Toronto Ridge with summits that are not exposed.

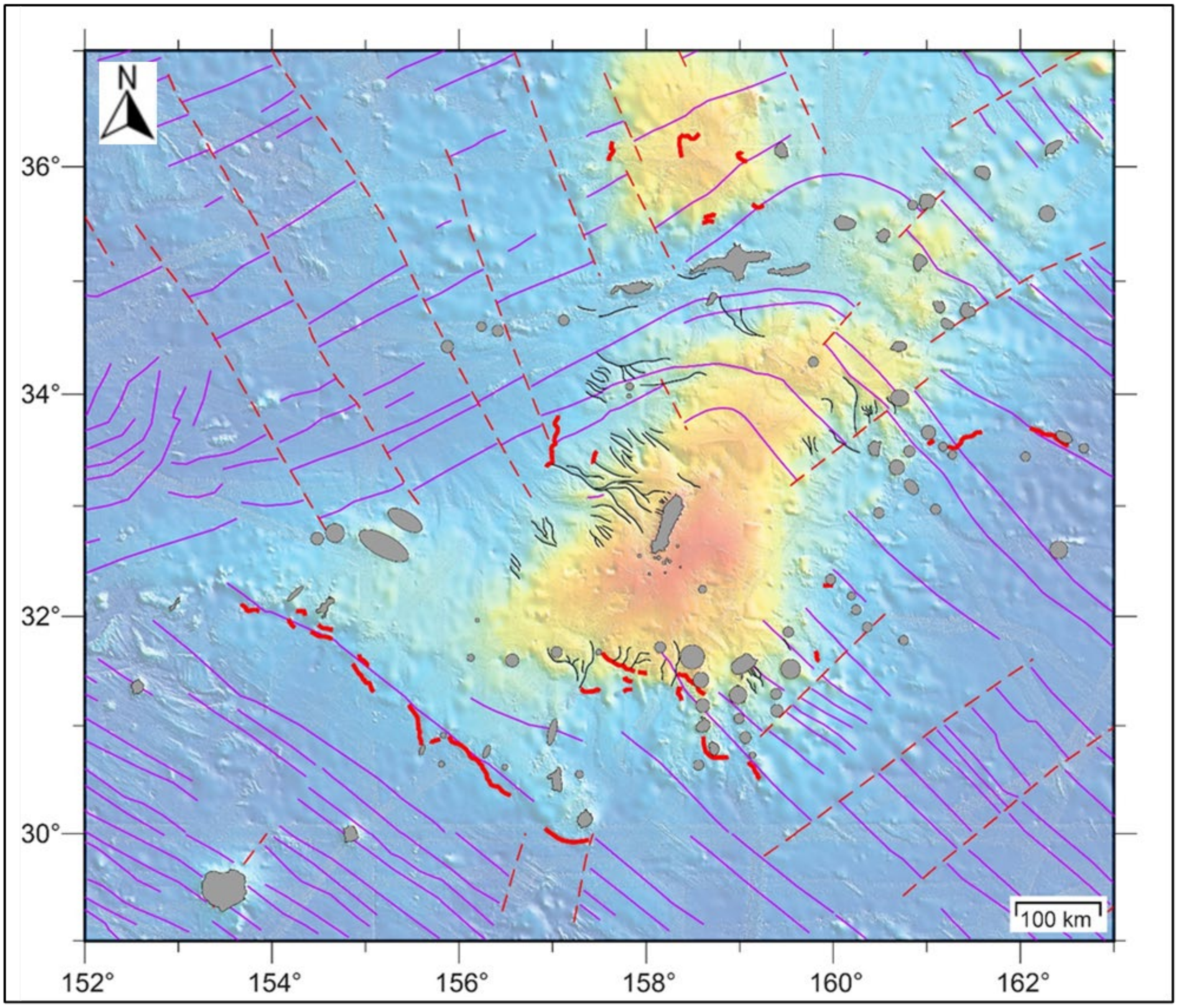

Figure 4.8 – Map showing distribution of features discussed in the text. Thick red lines are escarpments. Thin black lines denote submarine channels. Grey regions represent volcanic cones and seamounts. Purple lines are magnetic lineations and red dashed lines are fracture zones (Nakanishi et al., 1999). Background is the bathymetry map. Color scale is same as Figure 4.1.

In addition to Toronto Ridge and cones surrounding it, a total of 75 volcanic cones (height > 300 m) are observed in the bathymetry on the flanks of Tamu Massif (Figure 4.8). These cones have widths ranging between ~5-20 km and exhibit variety textures such as pointed cones, hummocky mounds, cratered tops or rounded, and nearly domes (Zhang et al., 2016). These cones are unevenly distributed across Tamu Massif with 54 of them found on the eastern and the southern flanks, while only a few cones were mapped on the west and north flanks.

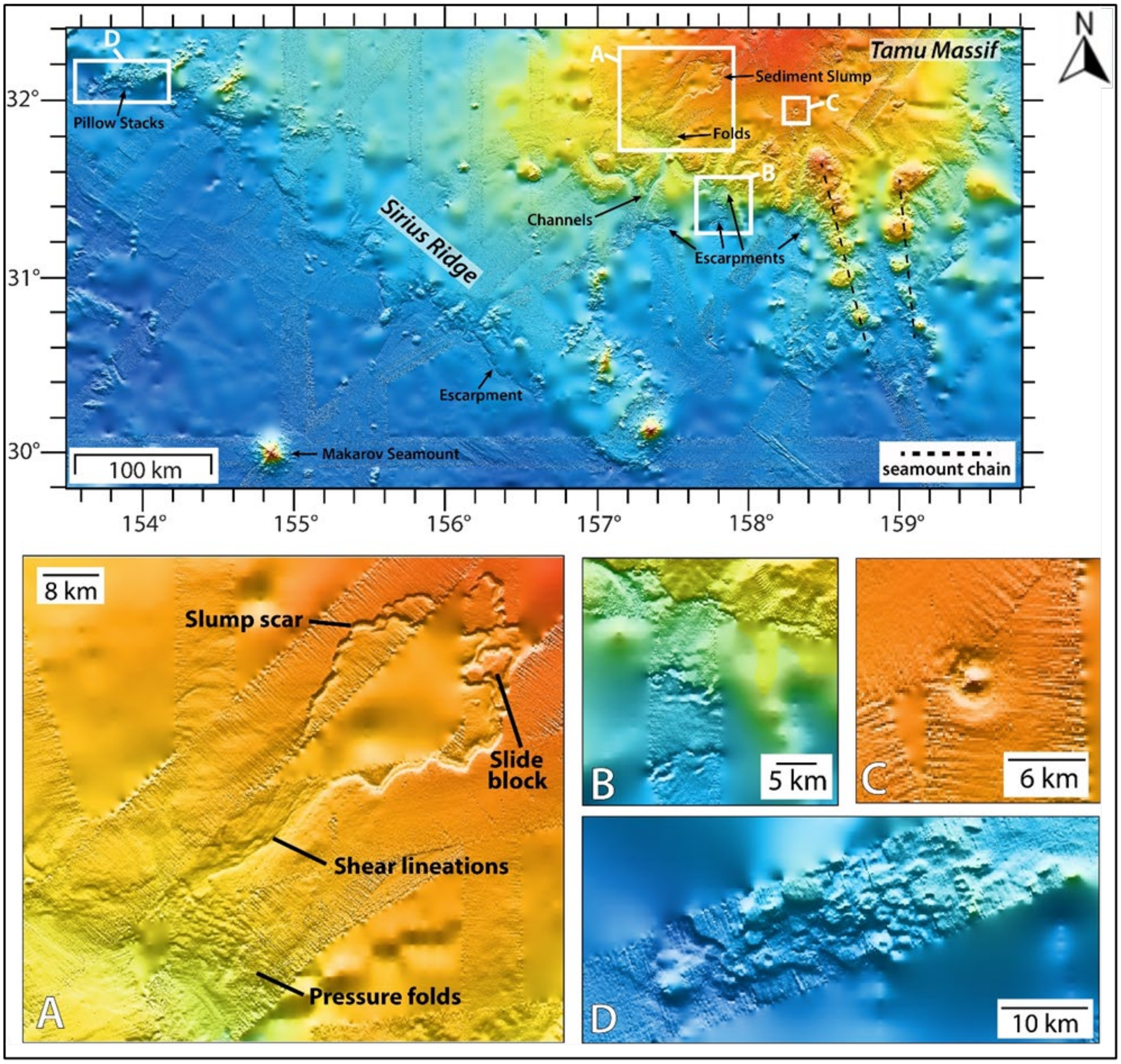

Figure 4.9 – Shaded relief bathymetry map of southern Tamu Massif. (A-C) Details of features discussed in text. (A) Sediment slide. (B) Sinuous parallel escarpments. (C) Cone clusters. Locations shown in main figure. Color scale is same as Figure 4.1.

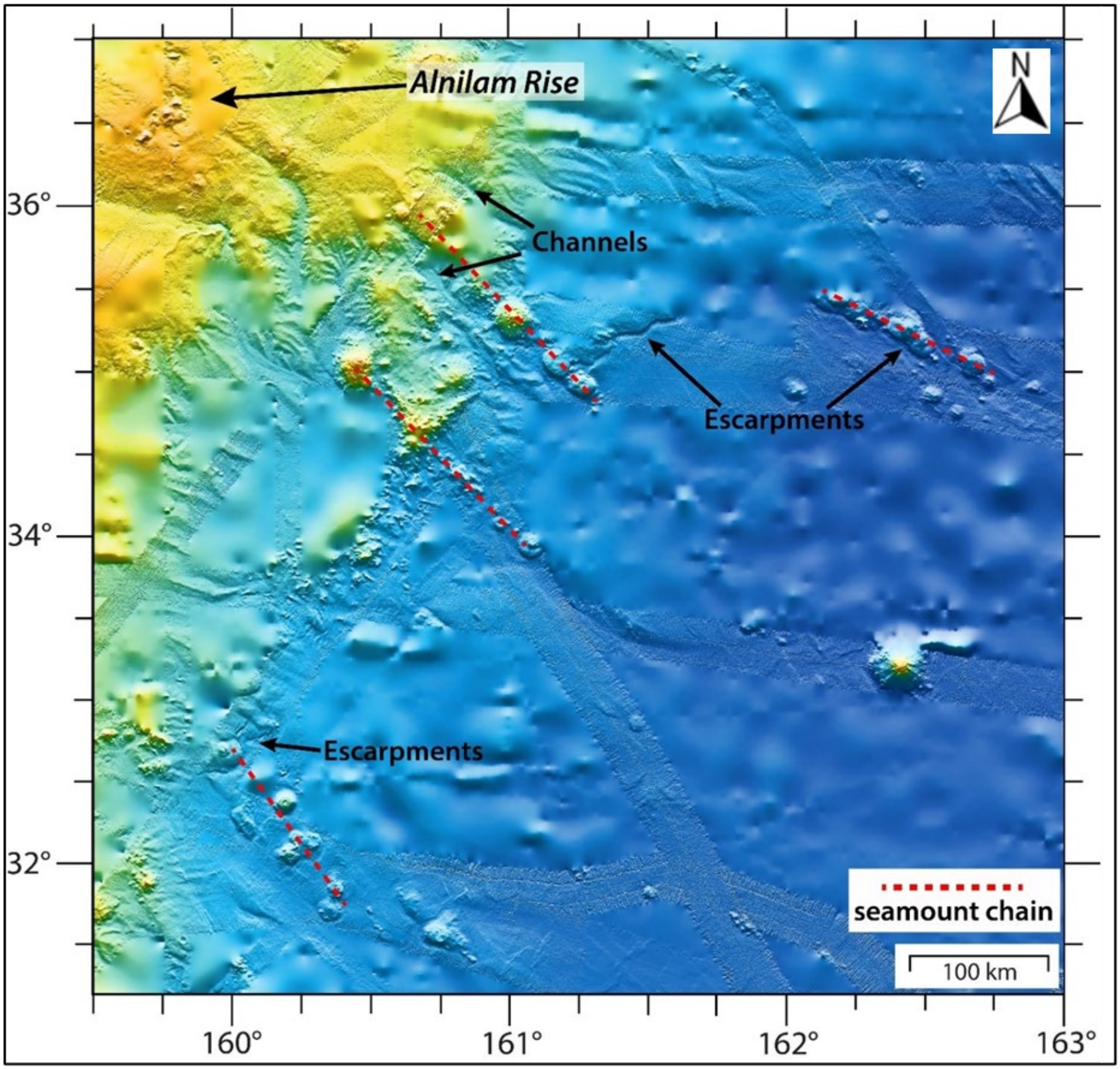

Figure 4.10 – Shaded relief bathymetry map for eastern Tamu Massif. Color scale is same as Figure 4.1.

Of the 54 cones occurring on the south and the east flanks, 28 cones occur in the form of 6 linear or curvilinear seamount chains. Two prominent seamount chains are located on the southeastern flank of Tamu Massif (158.7°-159.3°E, 30.5°-31.7°N; Figure 4.9). These chains trend ~N-S and have 6 seamounts within each chain. The size of the seamounts within each of these chains decreases basin ward by roughly by a factor of 5. The summit shape also changes, with seamounts on the north end having a flat domal summit with smaller, pointed peaks while those farther south have a domal summit with a well-defined conical crater. These chains trend

~N42°W, oblique to the magnetic lineations in the area. Four chains of small seamounts are observed at the base of the eastern flank (Figure 4.10). These chains trend ~N42°E and have ~4 seamounts in each, their size decreasing with increasing distance from Tamu Massif. These seamounts are parallel to surrounding magnetic lineations that have the same trend, suggesting a connection to spreading ridge tectonics.

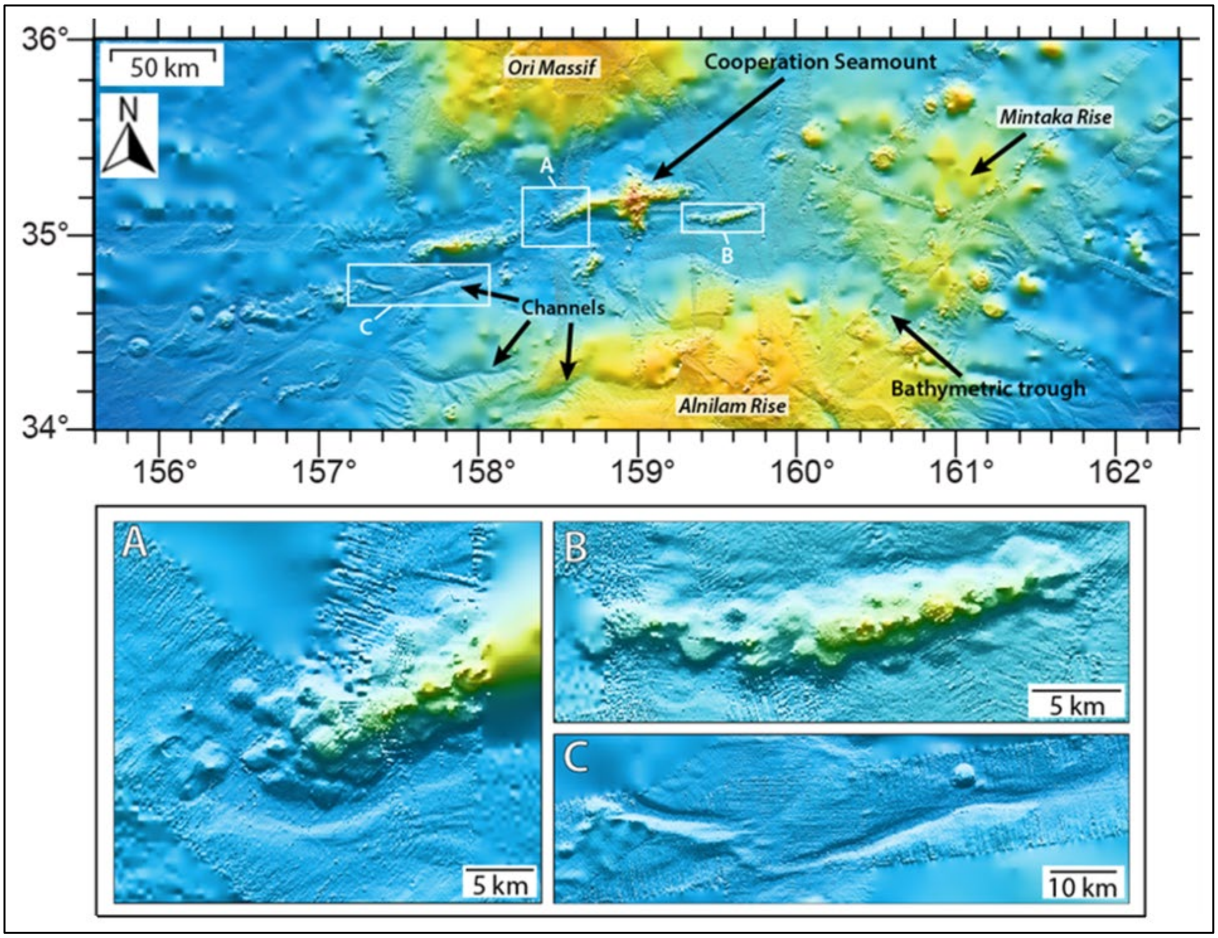

Figure 4.11 – Shaded relief bathymetry map of Helios basin and northern Tamu Massif. (A-C) Details of features discussed in text. (A) Pillow lava stack. (B) Linear ridge. (C) Abyssal channel. Locations shown in main figure. Color scale is same as Figure 4.1.

A chain of nearly E-W trending linear volcanic ridges (Figure 4.11) sits at the center of Helios Basin running along the length of the basin. Cooperation Seamount (Figure 4.11), which rises to ~2400 m depth, is a large volcanic edifice incorporated into the longest of these ridges (Sager et al., 1999), which is ~85 km long. This ridge is flanked by two others. That on the west is ~60 km in length and colinear. The eastern ridge (Figure 4.11B) is ~40 km in length but offset to the south. These volcanic ridges are oriented parallel to the magnetic lineations in the basin (Nakanishi et al., 1999), implying that the linear ridges are formed along spreading ridges (Zhang et al., 2016). The magnetic anomaly sequence in the region indicates the basin to have formed by normal spreading between two eruptions that formed Tamu and Ori Massifs (Zhang et al., 2016).

Seamounts also occur as isolated cones on all flanks of Tamu Massif. A distinct isolated volcanic cone (158.6°E, 32.2°N; Figure 4.4A) sits at the edge of south summit of Tamu Massif. This cone is ~5 km wide and ~315 m high and has a flat top. It is the source of dredged corals, suggesting that it was near sea level after eruption (Sager et al., 1999). In addition, several small sharp volcanic cones, mounds, cone clusters, and linear seamounts are scattered on top of Sirius Ridge, giving it a rough, bumpy texture. The bathymetry displays 4 linear seamounts (e.g., 154.6°E, 32.1°N and 157.0°E,30.5°N; Figure 4.9) ~15-20 km in length and ~1000-1300 m in height. Small, pointed cones overprint these linear seamounts. The two linear seamounts on the northwest end of Sirius Ridge trend ~N45°E-N50°E, are parallel to the Pacific magnetic lineations that trend ~N60°E while those on the southeast end trend ~ N5°E-N10°E, and are almost orthogonal to the adjacent Hawaiian lineations. A dense cluster of ~20 volcanic mounds (Figure 4.9D) ~1.5-2 km in diameter is exposed on a section on the northwest end of the ridge, but the extent of this cluster is unclear due to limited data coverage.

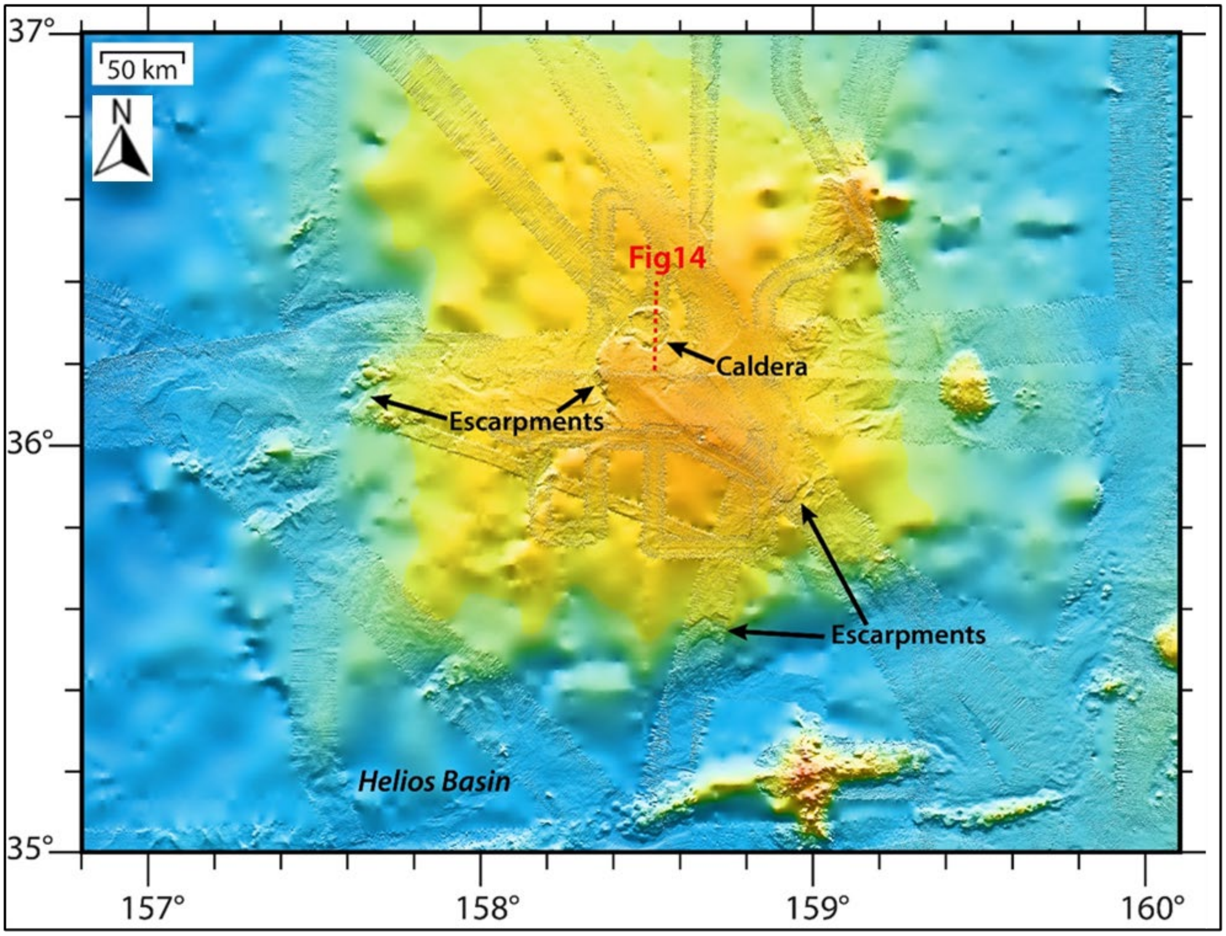

Figure 4.12 – Shaded relief bathymetry map of Ori Massif. Red dashed line represents the seismic section shown in Fig 13. Color scale same as Figure 4.1.

A volcanic dome (159.8°E, 34.3°N; Figure 4.5) ~9 km in diameter and ~600 m tall sits on the center of Alnilam Rise where it reaches the shallowest depth of ~2700 m. Other smaller pointed volcanic cones are scattered around the summit of this rise. Multiple flat top seamounts (many with cratered tops) are also observed scattered on the flanks of Mintaka Rise (Figure 4.11). These seamounts are ~10-20 km in width and ~700-1000 m in height. In contrast to Tamu Massif, only one large seamount (159.5°E, 36.1°N; Figure 4.12) can be observed on Ori Massif. This seamount is ~18 km wide and ~825 m high and is located on the eastern flank of Ori Massif.

4.3.2 Tectonic Features

Table 4.2 – List of all escarpments mapped around Tamu and Ori massifs

ID	Location (Lon, Lat)	Trend	Length (km)	Offset (m)	Region
E1¶	157°E, 33.5°N	N10°E	60	200	West flank, Tamu
E2¶	157.4°E, 33.4°N	N18°E	24	190	West flank, Tamu
E3*	153.7°E, 32°N	N97°E	22	120	South flank, Tamu
E4*	154.2°E, 31.9°N	N97°E	9	100	South flank, Tamu
E5*	154.2°E, 32°N	N97°E	11	142	South flank, Tamu
E6*	154.3°E, 32°N	N63°W	14	247	South flank, Tamu
E7*	154.6°E, 31.9°N	N78°W	17	592	South flank, Tamu
E8*	155°E, 31.6°N	N59°W	21	160	South flank, Tamu
E9*	154.9°E, 31.4°N	N47°W	35	308	South flank, Tamu
E10¶	155.6°E, 30.9°N	N7°W	32	304	South flank, Tamu
E11	155.7°E, 30.8°N	N31°E	15	190	South flank, Tamu
E12*¶	156.3°E, 30.6°N	N136°E	94	325	South flank, Tamu
E13*	157.2°E, 29.9°N	N107°E	35	671	South flank, Tamu
E14*¶	157.2°E, 31.2°N	N80°E	12	198	South flank, Tamu
E15*	157.5°E, 31.2°N	N73°E	9	208	South flank, Tamu
E16*¶	157.4°E, 31.3°N	E-W	17	206	South flank, Tamu
E17*	157.8°E, 31.3°N	N100°W	11	215	South flank, Tamu
E18*	157.8°E, 31.4°N	N69°W	10	356	South flank, Tamu
E19	157.8°E, 31.5°N	N72°W	51	272	South flank, Tamu
E20	158.2°E, 31.3°N	N70°W	23	447	South flank, Tamu
E21¶	158.3°E, 31.2°N	N23°W	24	367	South flank, Tamu
E22*	158.5°E, 31.3°N	N67°W	44	557	South flank, Tamu
E23	158.6°E, 30.7°N	N40°W	29	649	South flank, Tamu
E24*	159.1°E, 30.6°N	N30°W	26	622	South flank, Tamu
E25	159.8°E, 31.6°N	N114°E	13	129	East flank, Tamu
E26	159.8°E, 31.7°N	N71°E	9	170	East flank, Tamu
E27¶	160°E, 32.3°N	N29°E	32	323	East flank, Tamu
E28	160.8°E, 33.4°N	N50°E	20	213	East flank, Tamu
E29	161°E, 33.6°N	N29°E	19	139	East flank, Tamu
E30	161°E, 33.8°N	N29°E	17	284	East flank, Tamu
E31¶	161.5°E, 33.6°N	N65°E	42	272	East flank, Tamu
E32*	162.3°E,33.6°N	N30°W	46	414	East flank, Tamu
E33¶	158.5°E, 36.2°N	N80°E	30	217	Summit, Ori
E34	158.3°E, 36.1°N	N5°W	21	261	Summit, Ori
E35	157.6, 36.1°N	N9°E	22	243	West flank, Ori
E36	157.7°E, 36.1°N	N9°E	17	152	West flank, Ori
E37*	158.6°E, 35.5°N	N72°E	19	214	South flank, Ori
E38*	158.6°E, 35.6°N	N72°E	13	111	South flank, Ori

*scarps which are parallel to adjacent magnetic lineations; ¶scarps with plunge pools at the base

The bathymetry reveals 38 sinuous scarps (Table 4.2) of various lengths located on the flanks of Tamu Massif and Ori Massif. Some of these scarps (E1, E2, E8, E10; Table 4.2) have been previously mapped on the west and south flanks of Tamu Massif (Zhang et al., 2016), who interpreted them as normal faults based on seismic data. We find several similar features on the west, south, and east flanks of Tamu Massif and Ori Massif. Due to gaps in MBES data coverage, only sections of these scarps are revealed, and the true extent of these features is unclear. These scarps are ~9-94 km long and have vertical offsets ~100-670 m. Many of these scarps trend parallel to the regional bathymetric contours and are concentric around the massif centers. In addition, ~50% of these exposed scarps are also parallel to the adjacent magnetic lineations (Table 4.2), suggesting that these scarps are related to spreading ridge tectonics. Some of these scarps have a sedimentary trough ("plunge pools", Table 4.2) at the base that are ~40-120 m deeper than surrounding seafloor and run along the length of the scarps.

4.3.3 Sedimentary Features

Sediments accumulate over oceanic plateaus during their life cycle and are subjected to post-depositional processes such as current movements and mass wasting, which result in redistribution of the sediments. The surface of Tamu Massif is mostly smooth over the summit as it is covered by a lens-shape pelagic sediment dome that is ~1.2 km thick (Sager et al., 1999; Clark et al, 2018). Topography becomes rough on the flanks in all directions, being cut by submarine channels, sinuous escarpments, and secondary cones. The sediment cover over Ori Massif is variable and ranges from 0-~800 m in thickness. Like Tamu Massif, Helios Basin has a sediment thickness of ~1-2 km, thicker than the sediment cover in the abyssal plains (<1 km) surrounding Tamu Massif (Zhang et al., 2016).

Major channels with different characteristics, ranging from short linear channels to long branching channels and with varying depths, are observed descending Tamu Massif flanks. The channels are particularly well-imaged over the northwest flank (Figure 4.6) of the massif, where ten channels with widths varying from of ~1-10 km, depths ranging from 50-200 m, and trends of N75°E to N85°E are observed. The deeper and longer channels originate at the western edge of Toronto Ridge (158.2°E, 32.9°N; Figure 4.6), where multiple canyons ~3 km long, ~1 km wide, and ~200 m deep are incised. These channels dissect flank sediments and gradually disappear into the surrounding abyssal seafloor, where they terminate against a major escarpment near the base of the mountain (Figure 4.6A). The longest channel (157.4°E, 33.2°N; Figure 4.6) in this region is ~120 km in length and extends from the summit to the base of Tamu Massif. However, no large canyons or channels are observed to originate over the eastern edge of Toronto Ridge, which is adjacent to the thick sediment cap.

Similar channels also extend down the southern flank (Figure 4.9), where five channels of varying lengths up to ~50 km and depths up to ~400 m are observed. These channels also terminate against a series of parallel escarpments (Figure 4.9B) that trend ~N85° E. One difference on the south flank is the presence of secondary cones (157.48°E, 31.66°N; Figure 4.9) that affect channel paths in some places.

Less prominent channels are observed on the eastern and northern flanks. Channels are better defined on the north end of the eastern flank (Figure 4.8 & 4.10), where six such features rundown the flank of Alnilam Rise and end against a small escarpment. The longest channel (160.1°E, 34.1°N; Figure 4.10) here is ~70 km long, ~3 km wide, and ~200 m deep, originating at the summit of Alnilam Rise and running down the length of the flank. A prominent channel is observed on the northern flank of Alnilam Rise and branches into Helios Basin (158.9°E, 34.8°N; Figure 4.11). This channel is ~60 km long, ~10 km wide, and ~140 m deep and trends ~N42°W. In addition, four distinct abyssal channels (e.g., Figure 4.11C) trending ~E-W are observed at the center of Helios Basin. Two of these abyssal channels run along the southern base of the linear ridges located at the center of Helios Basin. The longest such channel is ~50 km long, ~3 km wide, and ~110 m deep and is located ~15 km south of the western ridge in Helios Basin.

MBES data also reveal downslope mass transport processes that have modified the sedimentary cover. A large submarine slide is mapped on the southwest flank of Tamu Massif, where the local slope is ~1° (157.7°E, 32.2°N; Figure 4.9A). The slide moved ~N134°W downslope, which is evident from the remanent headwall scarp left behind by the slump and accumulation of sediments at the base of the slump. The morphology changes along the slide from the headwall scarp on the northeast side to a sediment pile at the base on the southwest side. At the top of the headwall scarp (157.8°E, 32.2°N; Figure 4.9A), two isolated slide blocks are observed (157.8°E, 32.3°N and 157.8°E, 32.2°N; Figure 4.9A). The headwall scarp has a length of ~86 km and a relief of ~200 m. The slide has a width of ~11 km at the main headwall but widens to a maximum of ~25 km before narrowing down to ~7 km at the base. The slide mobilized ~165 km^3 of sediments ~60 km downslope, depositing the sediments into folds of wavelength of ~2 km and amplitude of ~40 m at the base of the slide.

In addition to large mass movements, small folds in sediments are also observed at multiple locations over the massif. This is particularly striking on the southeast upper flank, where multiple sediment folds (Figure 4.4A) can be observed in the bathymetry and seismic profile. These folds have wavelengths of ~1 km and heights of ~10-20 m. Similar folds can also be seen farther downslope on the eastern flank (159.0°E, 32.4°N; Figure 4.4), which might be an extension of the fold field from up the flank but is unclear because of a data gap.

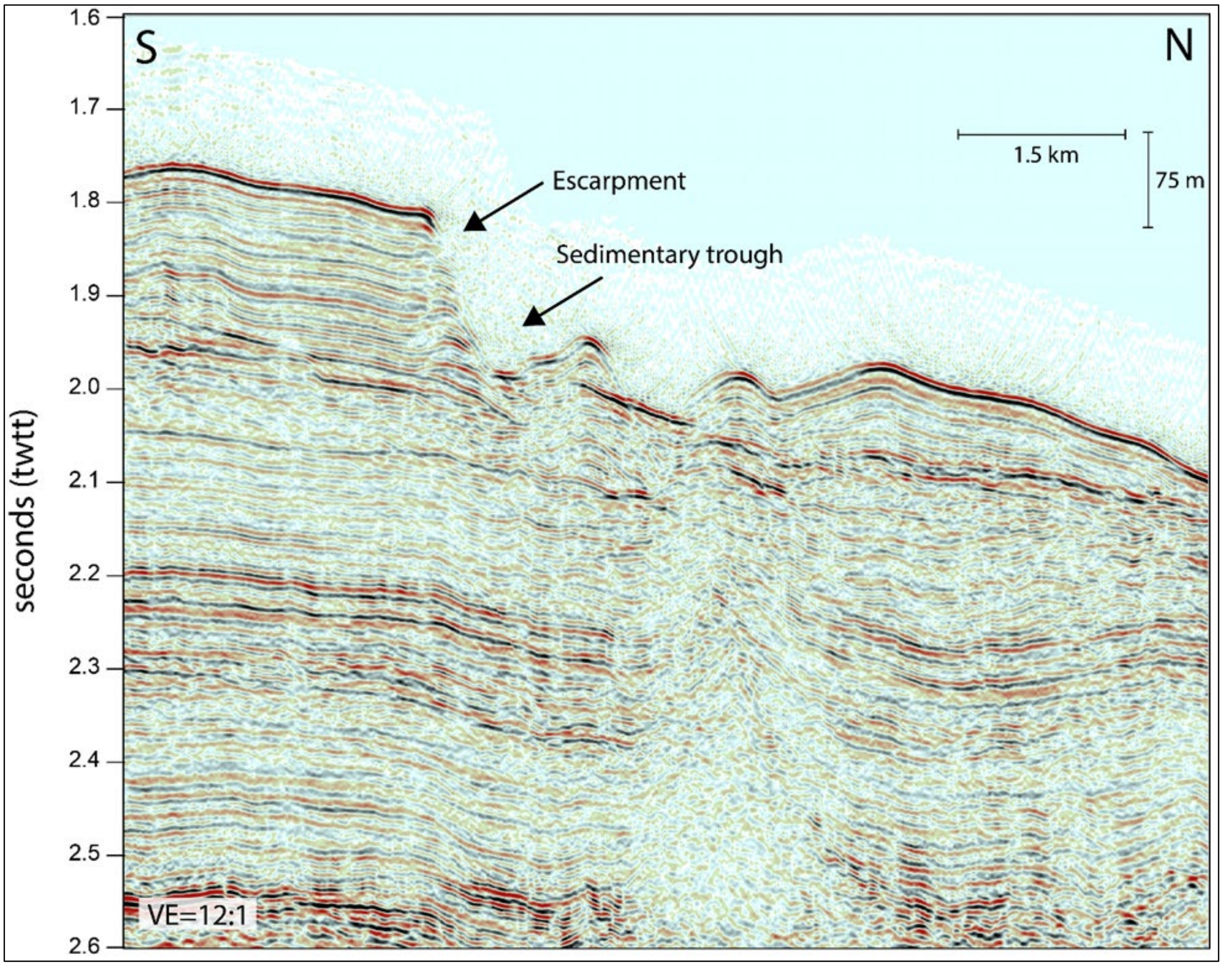

Figure 4.13 – Low-fold multichannel seismic section showing the structure of the sedimentary trough over the northern summit of Tamu Massif. Seismic section displays two-way travel-time in seconds (vertical axis) versus distance in km (horizontal axis). Profile location is shown in Fig 4.12. Abbreviations: VE, vertical exaggeration. Seismic profile is a section of line 14a of Klaus and Sager (2002).

Two curved sinuous sedimentary troughs are observed near the northern and southwestern edges of the Tamu Massif summit sediment cap. The sedimentary trough on the north (Figure 4.4) trends ~N141°E and undulates along its length. It is ~25 km long, ~75 m deep, and ~1-2 km wide. A seismic profile over the trough shows a depression surrounded by two sedimentary escarpments (Figure 4.13). The sedimentary trough on the southwestern summit, near Toronto Ridge, consists of two arcuate depressions facing each other (Figure 4.6), roughly forming a semi-circle. The arcuate depression to the left (Figure 4.6B) is ~22 km long, ~1.2 km wide, and ~50 m deep, whereas the arcuate depression to the right ~16 km long, ~1 km wide, and ~97 m deep. The overall N-S trend of these troughs is roughly parallel to the bathymetric contours and these troughs are located near the edge of the summit where the thick sediment cap begins to slope downhill, thinning on the flanks.

Some of the volcanic cones (Figure 4.6C) located to the south of Toronto Ridge are surrounded by small, mostly circular depressions (moats) in the sediment. These moats are also observed around two other cones, one on the south summit of Tamu Massif (158.1°E, 31.9°N; Figure 4.9C) and the other on the summit of Alnitak Rise (159.2°E, 33.6°N; Figure 4.5A), but are absent around cones elsewhere. These moats are usually symmetric around the cone with a width of ~1-1.5 km and a depth of ~80-120 m. Seismic data (Figure 4.7) over one such cone reveals it to be a tip of a larger basement cone buried under a thick layer of sediment.

A unique Y-shaped ridge was mapped on the summit of Alnitak Rise (Figure 4.4). The three arms have lengths, maximum heights, and average trends of ~60 km, ~150 m, and N100°W for the western ridge, ~50 km, ~140 m, and N57°E for the northern ridge, and ~25 km, ~140 m, and N154°E for the southeast ridge. The west and the southeast ridges are subparallel to the bathymetric troughs separating Tamu Massif from Alnitak Rise. Although a seismic profile over the northeast ridge (Figure 4.5) reveals the ridge to be a surface sediment feature, there is a clear basement structure ~400 m in height below. In addition, magnetic lineations (Sager et al., 2019) in the vicinity display magnetic bights (bent lineations) over the Y-ridge. The west ridge is quasi-parallel to the Pacific lineations, which trend ~N102° W, and the southeast ridge is parallel to the Hawaiian lineations, which trend ~N53°E.

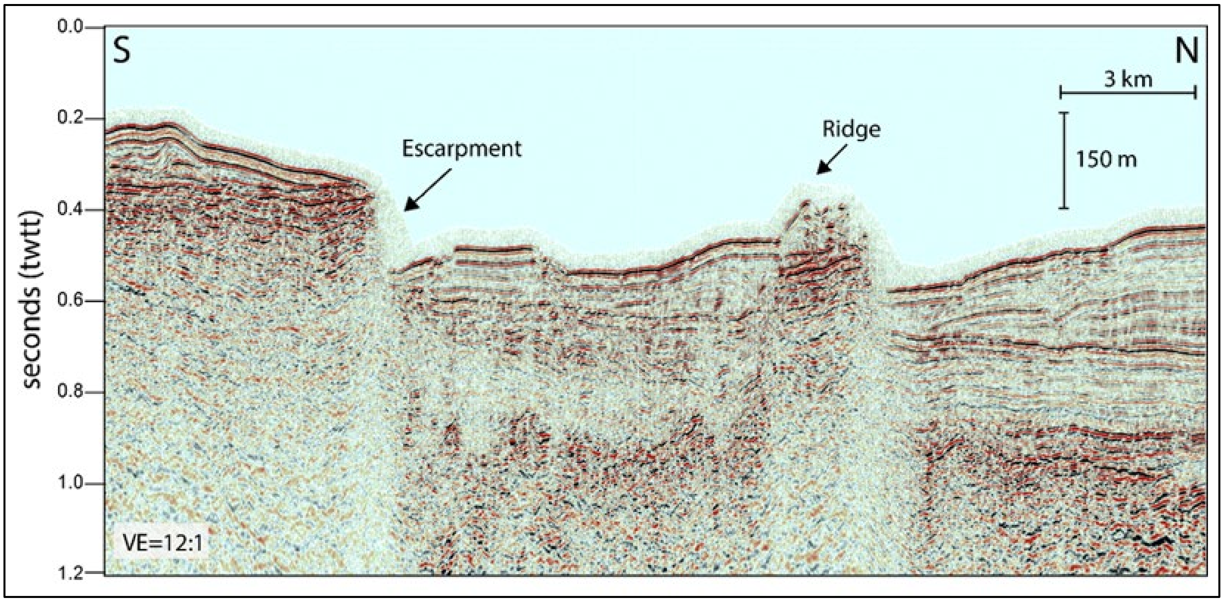

Figure 4.14 – Low-fold multichannel seismic profile showing the basement structure over the circular depression at the Ori Massif summit. Seismic section displays two-way travel-time in seconds (vertical axis) versus distance in km (horizontal axis). Profile location is shown in Figure 4.12. Abbreviations: VE, vertical exaggeration. Seismic profile is section of line 11b from Klaus and Sager (2002).

The improved bathymetry data reveals a distinct circular depression at the summit of Ori Massif (Figure 4.12). This depression is ~10 km wide and ~170 m deep and is bounded by a steep curved escarpment on the west. This curved escarpment is ~25 km long with a relief of ~220 m. A seismic profile (Figure 4.14) shows the circular depression to be bounded by a normal fault on the south perimeter and a volcanic ridge on the north.

4.4 Discussion

During their life cycle, oceanic plateaus go through three major evolutionary stages: shield forming, post-shield secondary volcanism, and quiescence with sedimentation and erosion. During the shield forming stage, massive eruptions occur at mid-oceanic ridges and multiple subsequent eruptions build the oceanic plateau. Due to weakening lithosphere from the upwelling hotspot and large amounts of lava being dumped on the seafloor, the plateau subsides the most at this stage. Eventually, due to seafloor spreading tectonics, the plateau migrates away from the hotspot and enters the post-shield stage of volcanism. During this phase, eruptions occur in random places and might be alternated with long periods of erosion. This secondary volcanism has a slow eruption rate and can take millions of years to develop (Clague and Sharrod, 2014). Subsequently, there is a period of quiescence and sedimentation as the plateau tops sink below productive waters and into the mid-gyre, while gravity leads to slope instability that gradually carves up the sediment cap. The improved bathymetry map (Figure 4.3) reveals previously obscured structures that have implications in each of the above stages of the evolution of southern Shatsky Rise.

4.4.1 Shield Building Stage

Segmentation of Tamu Massif

The new bathymetry map shows several subdued bathymetric troughs that cut across Tamu Massif, segmenting it further into 5 smaller edifices (Figure 4.3). The central dome of Tamu Massif is still the largest and the main edifice. Sirius Ridge and Procyon Rise flank the Tamu Massif to the south and southwest while Alnitak Rise, Alnilam Rise, and Mintaka Rise flank it to the northeast. These bathymetric troughs are roughly parallel to the surrounding magnetic lineations (Figure 4.1), implying that they are ridge-related features. In this study, these bathymetric troughs are explained as ridge jumps.

When a ridge jump happens, it leaves some remnant features behind and they can be observed in bathymetry and magnetic data. Studies on northeastern Pacific Rise (Klitgord and Mammerickx, 1982) have observed a bathymetric trough flanked by ridges between the jump locations. Similar ridge jump-bathymetric trough correlations have been identified at Azores plateau in North Atlantic (Honsho et al., 1996) and Rodriguez Triple Junction in Indian Ocean (Navarro et al., 2009).

Though initial evidence suggested Tamu Massif to be a large single volcano (Sager et al., 2013; Zhang et al.,2015), magnetic lineations were subsequently discovered inside the massif by Sager et al., (2019), who suggested that Tamu Massif formed from ridge-centered eruptions. Based on magnetic lineation data, Nakanishi et al. (1999) claimed that the triple junction jumped ~9 times along its way of forming Shatsky Rise. The locations of these ridge jumps are not well documented.

The location of these rises suggest that they were emplaced along SW-NE direction and the bathymetry reveals the size of these rises to decrease towards the NE (Figure 4.3). These bathymetric troughs suggest that the smaller edifices within Tamu Massif might have formed individually at or near the triple junction before the triple junction jumped to another location leaving behind a bathymetric trough and initiating the formation of a new edifice.

Around chron M22, the triple junction (TJ) that formed Shatsky Rise jumped ~800 km eastward to the location of Tamu Massif edifice and started moving northeastward forming Shatsky Rise (Nakanishi et al., 1999; 2015). Initially volcanism erupted at the TJ forming Sirius Ridge and Procyon Rise (Figures 4.3, 4.9). The TJ then jumped NE to the location of Tamu Massif, forming the central dome, leaving a trough in between the edifices. This process repeated and the TJ kept jumping further NE forming Alnitak Rise, Alnilam Rise, and Mintaka Rise along the way (Figures 4.3, 4.4, 4,5, 4.11). Coincidently, the new magnetic anomaly map of Tamu Massif (Sager et al., 2019) shows the magnetic anomalies to be bent near the summit of Alnitak Rise. These lineations are parallel to the Pacific plate magnetic lineations and represent the past location of the TJ that formed Tamu Massif. Furthermore, Huang et al., (2018) has noted another set of bent anomalies NW of Ori Massif and suggested that there might have been two

TJ involved in the formation of Shatsky Rise. However, owing of poor magnetic data and ridge jumps, the course of the TJ NE of Tamu Massif is unclear (Nakanishi 1999).

Escarpments

The bathymetry reveals numerous sinuous escarpments over the flanks of Tamu Massif and Ori Massif (Figure 4.8). Previously, only the two escarpments over the western flank of Tamu Massif were identified by Zhang et al. (2017). They were interpreted as down-to-basin normal faults based on seismic data. Due to improved coverage in multibeam bathymetry, we identified numerous similar escarpments on all flanks of Tamu Massif and Ori Massif. A total of 38 escarpments (Figure 4.8; Table 4.2) can be newly identified in bathymetry. All of these escarpments are concentrically located around the massifs and trend parallel to the bathymetry contours. The fact that these escarpments are mostly concentric around the massifs suggests that they formed due to differential subsidence, concentrated at the massif centers. Due to magmatic underplating, the flanks of the oceanic plateaus subside relatively faster than the centers, resulting in normal faults along the margins of the plateaus (Ito and Clift, 1998).

4.4.2 Post-shield Secondary Volcanism

In this study, plentiful evidence of secondary volcanism in the form of volcanic ridges, cones, and seamount chains was found all around the southern Shatsky Rise (Figure 4.8). Basalt has been recovered from dredged rocks from Toronto Ridge and few other seamounts (Tejada et al., 1995), suggesting a volcanic origin to these cones (Sager et al., 1999). However, the only available age for such features is one for Toronto Ridge (~122 Ma), indicating this ridge was emplaced ~17 Myr after the formation of Tamu Massif (Heaton and Koppers 2014). The timing of other secondary cones is unknown.

Secondary volcanic cones were previously identified in bathymetry by Zhang et al. (2017), who noted the cone distribution over Tamu Massif to be random. In contrast, the improved bathymetry coverage reveals the distribution to be non-uniform over Tamu Massif, with ~72% of the secondary cones on the southern and eastern flanks (Figures 4.9, 4.10). Some of seamounts over the eastern and southeastern flanks occur in the form of short seamount chains (Figure 4.10). The chains on the eastern flank trend parallel to the surrounding magnetic lineations, suggesting a spreading-ridge formation (Figure 4.10). In addition, these seamount chains appear to extend all the way north to the Ojin Rise seamounts, which have similar morphology.

Sano et al. (2020) proposed that the Ojin Rise seamounts developed via near-ridge hotspot volcanism based on petrography and trace element analyses of dredged rocks from the seamounts. Based on gravity and bathymetric modelling of the Ojin Rise seamounts, Shimuzu et al. (2020) suggested that the secondary volcanism over Shatsky Rise might have occurred on or near the Pacific-Farallon Ridge. This suggests that the hotspot forming Shatsky Rise was probably closer to the Pacific-Farallon plate, resulting in selective secondary volcanism along the eastern flanks. The seamount chains over the eastern flank might have formed by interactions of the hotspot with the Pacific-Farallon Ridge.

Although the seamount chains on the southeastern flank have similar morphology to those on the east flank, they trend oblique to the magnetic lineations (Figure 4.1, 4.9). Sager et al. (2019) suggested that complex tectonics involving ~90º anticlockwise rotation of a segment of the Pacific-Farallon Ridge led to the formation of Tamu Massif. The southeastern flank seamount chains are located at the border of this reorganization zone, and thus may be a result of hotspot eruptions at a reorganizing ridge. A chain of E-W trending linear volcanic ridges (Figure

4.11) lies near the center of Helios Basin and is nearly parallel to the adjacent magnetic lineations, probably formed when magma escaped through volcanic fissures. The pattern of the seamount chains in the region suggests that majority of the secondary volcanism probably occurs along volcanic rift zones, where sources of magma are available (e.g., MacDonald et al., 1983).

The high-resolution of multibeam bathymetry also reveals minute details such as the texture of Toronto Ridge (Figure 4.4). The summit of this ridge has a rough, hummocky texture with many small volcanic domes scattered across it (Figure 4.4B). Similar volcanic domes have been identified atop Galapagos Ridge, where the lava flow morphology shows the mounds to have formed from piling of pillow lava basalts (McClinton et al., 2013). A similar stacking of pillow lava layers probably resulted in forming the flat mounds at the Toronto Ridge summit and the escarpments are probably caused by coalesced pillow flows. Like Toronto Ridge, the linear ridges to the center of Helios basin exhibit a similar hummocky texture with a rough, lumpy surface (Figure 4.11B). These linear ridges are overprinted by small volcanic cones, especially near their edges (Figures 4.11A), which are probably stacks of small pillow lava cones that erupt near eruptive fissures.

4.4.3 Sedimentation and Erosion

Barring other processes, simple pelagic sedimentation would produce a thick cap that thins on the flanks and is minimum over adjacent abyssal plains (e.g., Karig et al., 1970; Shipley et al., 1983; Clark et al., 2018). This sediment morphology is caused by the summit elevated above the Calcite Compensation Depth (CCD) and shallower than the flanks, resulting in greater accumulation rates at the summit than the flanks (Berger et al., 1976; Rea et al., 2005).

Post-deposition sedimentary processes have occurred that modify this picture. The bathymetry reveals numerous erosional and mass wasting features such as channels, sediment slumps, slides, and creep folds on Tamu Massif, Ori Massif, and in Helios Basin. Furthermore, there is a local variability in sediment thickness, probably a result of bottom currents interacting with topographic features, a process poorly understood (Clark et al., 2018). Initial sediment layers have been reworked by the bottom currents, stripping the surface of sediments in some areas and depositing them as lenses elsewhere.

Sediment Redistribution

Submarine channels are observed trending downslope of all the flanks of Tamu Massif. These channels are usually formed due to turbidity or gravity currents triggered by mobilization of sediments on a slope (Hampton et al. 1996). The channels are distributed unevenly across the Tamu Massif's flanks (Figure 4.8). Longer and deeper channels are selectively located on the western and southern flanks whereas those on the eastern and northern flanks are relatively shorter and shallower (Figure 4.8). Because many of the larger channels on the northwest flank originate near Toronto Ridge (Figure 4.6), this structure may be controlling the channel distribution in this area (Zhang et al., 2017). Seamounts have a large impact on circulation patterns and bottom currents, impacting sediment distribution of the surrounding seafloor (Batiza, 2001; Rogers, 2013). Similar interactions between Toronto Ridge and bottom currents might have destabilized the NW side of the sediment cap, steering the sediments down the NW Tamu Massif flank and carving these long deep channels.

In contrast to the western flank, the channels on the southern flank are shorter and wider (Figure 4.8). Those on the southwest flank are deeper and wider whereas the channels to the southeast are less prominent. Channel morphology on the southern flank is influenced by mass wasting events and secondary cones. A large submarine slide is located on the southern flank of the Tamu Massif (Figure 4.9A). Though not common, slumps can occur in the low slope environment typical of Tamu Massif and are often attributed to high pore fluid pressure in the sediments (Urlaub et al., 2015). This mechanism is probably responsible for causing the mass slide on this flank. This slide mobilized a large amount of sediment downhill, causing the sediment to fold and form pressure ridges at the base of the slide. The sediment flow from the slide was probably steered along these channels on the southwest flank, resulting in deeper and wider channels. Some secondary cones and escarpments located on this flank have affected the orientation of channels (Figures 4.8, 4.9).

Less prominent channels are observed over the eastern and northern flanks of Alnilam Rise (Figures 4.10, 4.11). The channels over the northern flank terminate towards the base of linear seamounts in the Helios basin. Several E-W trending abyssal floor channels can be observed following the base of the linear volcanic ridges in this basin (Figures 4.11). The turbidity currents originating over the northern flank seem to interact with the seamount topography and are steered laterally to carve these abyssal channels.

In addition to large scale massive sediment flows like the ones in submarine channels and sediment slides, the high-resolution bathymetry also reveals very slow sediment flows and sediment failures. Indications of sediment creep can be observed atop eastern flank in bathymetry and in seismic data (Figure 4.4A). Creep is a result of a very slow motion of gravity-driven sediment down the flank. Sedimentary troughs can be observed over the northeastern summit of Tamu Massif and at the southern base of Toronto Ridge (Figures 4.4C, 4.6B). These troughs are located on the edges of the thick sediment cap, where it starts to slope downhill on the flanks. Seismic data reveals these troughs to be sedimentary grabens bounded by two escarpments (Figure 4.13). These features might be creep ruptures that result from sediment loading on sloped surfaces and might to precursors of major slope failures.

Moats

Most of the secondary cones near south end of Toronto Ridge have a prominent depression (moat) surrounding them (Figures 4.5A, 4.6C, 4.9C). The secondary cones are too small to form moats via lithospheric flexure (Watts, 1982). Furthermore, moats are only seen around a few volcanic cones, implying that they are not generated as a result of bottom current interactions, in which case, all volcanic moats would have formed moats around them. Seismic data reveal the moats to be depressions in the sediment around the protruding tip of a buried cone (Figure 4.7). Similar moats are observed around equatorial Pacific seamounts (Beckins et al., 2007) and their origin has been linked to retrograde dissolution of carbonate sediments. When carbonate-saturated ocean water penetrates the crust through fissures, it becomes undersaturated as the temperature rises. This undersaturated carbonate water re-enters the ocean via the seamounts, where it interacts with cold ocean water, causing the breakdown of carbonate deposits around the seamounts and resulting in moat formation (Beckins et al., 2007; Pockalny et al., 2007). The moats observed around the seamounts over Tamu Massif may be formed by a similar dissolution process.

4.5 Conclusions

A multibeam bathymetry survey was conducted onboard R/V Falkor (FK151005), acquiring large amount of data over Tamu Massif. Data from several additional multibeam cruises, previously unavailable, were also acquired. Merging the new data with previously available multibeam data, we generated a new improved bathymetry map for southern Shatsky

Rise. Gaps in the multibeam data coverage were filled with the global SRTM15+ bathymetry model.

The map reveals Tamu Massif to be segmented by subdued bathymetric troughs that divide it into 5 smaller edifices. The correlation of the bathymetric troughs with magnetic lineations suggests that Tamu Massif was built up by a series of eruptions along a northeast-jumping TJ, forming small edifices enroute. We mapped numerous escarpments encircling Tamu Massif and Ori Massif, attributed to differential subsidence of Shatsky Rise massifs. Multibeam data reveals extensive secondary volcanism over Tamu Massif. The secondary volcanism is more prevalent over the eastern flanks and southeastern flanks due to selective interaction of hotspot with the Pacific-Farallon Ridge.

Sediment distribution over the massifs is highly variable in places exposing igneous basement, contrary to that expected from pelagic sediment covering the massifs. We found evidence of significant downslope sediment movement caused by erosional processes reworking the sediment caps of Tamu Massif and Ori Massif. Prominent submarine channels and a large sediment slide, which transported large amounts of sediments downslope into surrounding abyssal plains, were mapped. Smaller sediment movements such as sediment creep and creep ruptures were also captured in the multibeam. Hydrothermal activity also probably occurred around secondary volcanoes near Toronto Ridge, forming sedimentary moats by retrograde dissolution of carbonate sediments.

4.6 Bibliography

Anderson, D. L., & Natland, J. H. (2014). Mantle updrafts and mechanisms of oceanic volcanism. Proceedings of the National Academy of Sciences, 111(41), E4298–E4304.

Batiza, R. (2001). Seamounts and Off-ridge Volcanism. In J. H. Steele (Red), Encyclopedia of Ocean Sciences (bll 2696–2708).

Becker, J. J., Sandwell, D. T., Smith, W. H. F., Braud, J., Binder, B., Depner, J. L. (2009). Global bathymetry and elevation data at 30 arc seconds resolution: SRTM30_PLUS. Marine Geodesy, 32(4), 355–371.

Bekins, B. A., Spivack, A. J., Davis, E. E., & Mayer, L. A. (2007). Dissolution of biogenic ooze over basement edifices in the equatorial Pacific with implications for hydrothermal ventilation of the oceanic crust. Geology, 35(8), 679–682.

Berger, W. H., Adelseck, C. G., Jr, & Mayer, L. A. (1976). Distribution of carbonate in surface sediments of the Pacific Ocean. Journal of Geophysical Research, 81(15), 2617–2627.

Campbell, I. H. (2005). Large igneous provinces and the mantle plume hypothesis. Elements, 1(5), 265–269.

Clague, D. A., & Sherrod, D. R. (2014). Growth and degradation of Hawaiian volcanoes. US Geological Survey.

Clark, R. W., Sager, W. W., & Zhang, J. (2018). Seismic stratigraphy of the Shatsky Rise sediment cap, northwest Pacific, and implications for pelagic sedimentation atop submarine plateaus. Marine Geology, 397, 43–59.

Foulger, G. R. (2007). The “Plate” model for the genesis of melting anomalies. Special Papers-Geological Society of America, 430, 1.

Geldmacher, J., van den Bogaard, P., Heydolph, K., & Hoernle, K. (2014). The age of earth’s largest volcano: Tamu Massif on Shatsky Rise (northwest Pacific Ocean). International Journal of Earth Sciences, 103(8), 2351–2357.

Hampton, M. A., Lee, H. J., & Locat, J. (1996). Submarine landslides. Reviews of geophysics, 34(1), 33–59.

Hanyu, T., Tejada, M. L. G., Shimizu, K., Ishizuka, O., Fujii, T., Kimura, J.-I. (2017). Collision-induced post-plateau volcanism: Evidence from a seamount on Ontong Java Plateau. Lithos, 294, 87–96.

Harris, P. T., Macmillan-Lawler, M., Rupp, J., & Baker, E. K. (2014). Geomorphology of the oceans. Marine Geology, 352, 4–24.

Heaton, D. E., & Koppers, A. A. P. (2014). High Resolution Dating of Louisville Guyots from IODP Sites U1372, U1375, U1376 and U1377: Implications for post-erosional hotspot ocean island processes and volcanism. AGU Fall Meeting Abstracts, 2014, V11B-4698.

Hilde, T. W. C., Uyeda, S., & Kroenke, L. (1977). Evolution of the western Pacific and its margin. Tectonophysics, 38(1–2), 145–165.

Hirano, N., Sumino, H., Morishita, T., Machida, S., Kawano, T., Yasukawa, K., Ishii, T. (2021). A Paleogene magmatic overprint on Cretaceous seamounts of the western Pacific. Island Arc, 30(1), e12386.

Homrighausen, S., Hoernle, K., Hauff, F., Wartho, J.-A., van den Bogaard, P., & Garbe-Schönberg, D. (2019). New age and geochemical data from the Walvis Ridge: The temporal and spatial diversity of South Atlantic intraplate volcanism and its possible origin. Geochimica et Cosmochimica Acta, 245, 16–34.

Honsho, C., Tamaki, K., & Fujimoto, H. (1996). Three-dimensional magnetic and gravity studies of the Rodriguez Triple Junction in the Indian Ocean. Journal of Geophysical Research: Solid Earth, 101(B7), 15837–15848.

Huang, Y., Sager, W. W., Tominaga, M., Greene, J. A., Zhang, J., & Nakanishi, M. (2018). Magnetic anomaly map of Ori Massif and its implications for oceanic plateau formation. Earth and Planetary Science Letters, 501, 46–55.

Ito, G., & Clift, P. D. (1998). Subsidence and growth of Pacific Cretaceous plateaus. Earth and Planetary Science Letters, 161(1–4), 85–100.

Karig, D. E., Peterson, M. N. A., & Short, G. G. (1970). Sediment-capped guyots in the Mid-Pacific Mountains. Deep Sea Research and Oceanographic Abstracts, 17, 373–378. Elsevier.

Klaus, A., & Sager, W. W. (2002). Data report: High-resolution site survey seismic reflection data for ODP Leg 198 drilling on Shatsky Rise, northwest Pacific. Proc. ODP, Init. Repts, 198, 1–21.

Klitgord, K. D., & Mammerickx, J. (1982). Northern East Pacific Rise: magnetic anomaly and bathymetric framework. Journal of Geophysical Research: Solid Earth, 87(B8), 6725–6750.

Larson, R. L., & Chase, C. G. (1972). Late Mesozoic evolution of the western Pacific Ocean. Geological Society of America Bulletin, 83(12), 3627–3644.

Lonsdale, P., Dieu, J., & Natland, J. (1993). Posterosional volcanism in the Cretaceous part of the Hawaiian hotspot trail. Journal of Geophysical Research: Solid Earth, 98(B3), 4081–4098.

McClinton, T., White, S. M., Colman, A., & Sinton, J. M. (2013). Reconstructing lava flow emplacement processes at the hotspot-affected Galápagos Spreading Center, 95 W and 92 W. Geochemistry, Geophysics, Geosystems, 14(8), 2731–2756.

Macdonald, G. A., & Abbott, A. (1983). Volcanoes in the sea: the geology of Hawaii. University of Hawaii Press.

Mitchum, R. M., Jr, Vail, P. R., & Sangree, J. B. (1977). Seismic stratigraphy and global changes of sea level: Part 6. Stratigraphic interpretation of seismic reflection patterns in depositional sequences: Section 2. Application of seismic reflection configuration to stratigraphic interpretation.

Nakanishi, M., Tamaki, K., & Kobayashi, K. (1989). Mesozoic magnetic anomaly lineations and seafloor spreading history of the northwestern Pacific. Journal of Geophysical Research: Solid Earth, 94(B11), 15437–15462.

Nakanishi, M., Sager, W. W., & Klaus, A. (1999). Magnetic lineations within Shatsky Rise, northwest Pacific Ocean: Implications for hotspot-triple junction interaction and oceanic plateau formation. Journal of Geophysical Research: Solid Earth, 104(B4), 7539–7556.

Nakanishi, M., Sager, W. W., & Korenaga, J. (2015). Reorganization of the Pacific-Izanagi-Farallon triple junction in the Late Jurassic: Tectonic events before the formation of the Shatsky Rise. The Origin, Evolution, and Environmental Evolution of Oceanic Large Igneous Provinces: Geological Society of America Special Papers, 511, 85–101.

Navarro, A., Lourenço, N., Chorowicz, J., Miranda, J. M., & Catalão, J. (2009). Analysis of geometry of volcanoes and faults in Terceira Island (Azores): Evidence for reactivation tectonics at the EUR/AFR plate boundary in the Azores triple junction. Tectonophysics, 465(1–4), 98–113.

O'Connor, J. M., & Jokat, W. (2015). Tracking the Tristan-Gough mantle plume using discrete chains of intraplate volcanic centers buried in the Walvis Ridge. Geology, 43(8), 715–718.

Ohira, A., Kodaira, S., Nakamura, Y., Fujie, G., Arai, R., & Miura, S. (2017). Structural variation of the oceanic Moho in the Pacific plate revealed by active-source seismic data. Earth and Planetary Science Letters, 476, 111–121.

Ogg, J. G. (2012). Geomagnetic polarity time scale. In F. M. Gradstein, J. G. Ogg, M. Schmitz, G. Ogg (Eds.), The geologic time scale 2012 (pp. 85–113).

Pietsch, R., & Uenzelmann-Neben, G. (2015). The Manihiki Plateau—A multistage volcanic emplacement history. Geochemistry, Geophysics, Geosystems, 16(8), 2480–2498.

Pockalny, R., Murphy, E., & Spivack, A. (2007). Seamount Moats in the Central Equatorial Pacific Ocean: Origins and Implications. AGU Fall Meeting Abstracts, 2007, T12A-05.

Rea, D. K., & Lyle, M. W. (2005). Paleogene calcite compensation depth in the eastern subtropical Pacific: Answers and questions. Paleoceanography, 20(1).

Richards, M. A., Duncan, R. A., & Courtillot, V. E. (1989). Flood basalts and hot-spot tracks: plume heads and tails. Science, 246(4926), 103–107.

Rogers, A. (2012). An ecosystem approach to management of seamounts in the Southern Indian Ocean: volume 1: overview of seamount ecosystems and biodiversity.

Sager, W. W., Handschumacher, D. W., Hilde, T. W. C., & Bracey, D. R. (1988). Tectonic evolution of the northern Pacific plate and Pacific-Farallon Izanagi triple junction in the Late Jurassic and Early Cretaceous (M21-M10). Tectonophysics, 155(1–4), 345–364.

Sager, W. W., Kim, J., Klaus, A., Nakanishi, M., & Khankishieva, L. M. (1999). Bathymetry of Shatsky Rise, northwest Pacific Ocean: Implications for ocean plateau development at a triple junction. Journal of Geophysical Research: Solid Earth, 104(B4), 7557–7576.

Sager, W. W., Sano, T., & Geldmacher, J. (2011). How do oceanic plateaus form? Clues from drilling at Shatsky Rise. Eos, Transactions American Geophysical Union, 92(5), 37–38.

Sager, W. W., Zhang, J., Korenaga, J., Sano, T., Koppers, A. A. P., Widdowson, M., & Mahoney, J. J. (2013). An immense shield volcano within the Shatsky Rise oceanic plateau, northwest Pacific Ocean. Nature Geoscience, 6(11), 976–981.

Sager, W. W., Pueringer, M., Carvallo, C., Ooga, M., Housen, B., & Tominaga, M. (2015). Paleomagnetism of igneous rocks from the Shatsky Rise: Implications for paleolatitude and oceanic plateau volcanism. Geological Society of America Special Papers, 511, 147–171.

Sager, W. W., Huang, Y., Tominaga, M., Greene, J. A., Nakanishi, M., & Zhang, J. (2019). Oceanic plateau formation by seafloor spreading implied by Tamu Massif magnetic anomalies. Nature Geoscience, 12(8), 661–666.

Sano, T., Hanyu, T., Tejada, M. L. G., Koppers, A. A. P., Shimizu, S., Miyazaki, T. (2020). Two-stages of plume tail volcanism formed Ojin Rise Seamounts adjoining Shatsky Rise. Lithos, 372, 105652.

Saunders, A. D., England, R. W., Reichow, M. K., & White, R. V. (2005). A mantle plume origin for the Siberian traps: uplift and extension in the West Siberian Basin, Russia. Lithos, 79(3–4), 407–424.

Seton, M., Müller, R. D., Zahirovic, S., Gaina, C., Torsvik, T., Shephard, G. (2012). Global continental and ocean basin reconstructions since 200 Ma. Earth-Science Reviews, 113(3–4), 212–270.

Shimizu, S., Nakanishi, M., & Sano, T. (2020). Near-ridge-axis volcanism affected by hotspot: insights from effective elastic thickness and topography of the Ojin Rise Seamounts, east of Shatsky Rise in the northwest Pacific Ocean. Earth, Planets and Space, 72(1), 1–8.

Shipley, T. H., Winterer, E. L., & Lonsdale, P. (1983). Seismic-stratigraphic analysis in the pelagic environment: the central Hess Rise, Northwest Pacific. Marine Geology, 51(1–2), 47–62.

Sliter, W. V., & Brown, G. R. (1993). Shatsky Rise: seismic stratigraphy and sedimentary record of Pacific paleoceanography since the Early Cretaceous. Natland, JH, Storms, MA, et al., Proc. ODP, Sci. Results, 132, 3–13.

Smith, W. H. F., & Sandwell, D. T. (1997). Global sea floor topography from satellite altimetry and ship depth soundings. Science, 277(5334), 1956–1962.

Tejada, M.L.G., Mahoney, J.J., Sager, W.W., and Shipboard Scientific Party, 1995. Isotopic study of basement rocks from Shatsky Rise, northwestern Pacific Ocean (abstract). EOS, Trans. AGU, Fall Mtg. Suppl., 76: F699

Tejada, M. L. G., Geldmacher, J., Hauff, F., Heaton, D., Koppers, A. A. P., Garbe-Schönberg, D., Sager, W. W. (2016). Geochemistry and age of Shatsky, Hess, and Ojin Rise seamounts: Implications for a connection between the Shatsky and Hess Rises. Geochimica et Cosmochimica Acta, 185, 302–327.

Torsvik, T. H., Steinberger, B., Shephard, G. E., Doubrovine, P. V., Gaina, C., Domeier, M., Sager, W. W. (2019). Pacific‐Panthalassic reconstructions: Overview, errata and the way forward. Geochemistry, Geophysics, Geosystems, 20(7), 3659–3689.

Tozer, B., Sandwell, D. T., Smith, W. H. F., Olson, C., Beale, J. R., & Wessel, P. (2019). Global bathymetry and topography at 15 arc sec: SRTM15+. Earth and Space Science, 6(10), 1847–1864.

Urlaub, M., Talling, P. J., Zervos, A., & Masson, D. (2015). What causes large submarine landslides on low gradient (< 2°) continental slopes with slow (0.15 m/kyr) sediment accumulation? Journal of Geophysical Research: Solid Earth, 120(10), 6722–6739.

Watts, A. B. (1982). Seamounts and flexure of the lithosphere. Nature, 297(5863), 182–183.

Wessel, P., Luis, J. F., Uieda, L., Scharroo, R., Wobbe, F., Smith, W. H. F., & Tian, D. (2019). The generic mapping tools version 6. Geochemistry, Geophysics, Geosystems, 20(11), 5556–5564.

Whittaker, J. M., Afonso, J. C., Masterton, S., Müller, R. D., Wessel, P., Williams, S. E., & Seton, M. (2015). Long-term interaction between mid-ocean ridges and mantle plumes. Nature Geoscience, 8(6), 479–483.

Yeo, I. A., & Searle, R. C. (2013). High-resolution Remotely Operated Vehicle (ROV) mapping of a slow-spreading ridge: Mid-Atlantic Ridge 45° N. Geochemistry, Geophysics, Geosystems, 14(6), 1693–1702.

Zhang, J., Sager, W. W., & Korenaga, J. (2015). The Shatsky Rise oceanic plateau structure from two-dimensional multichannel seismic reflection profiles and implications for oceanic plateau formation. The origin, evolution, and environmental impact of oceanic large igneous provinces, geophysical society of america special paper, 511, 103–126.

Zhang, J., Sager, W. W., & Korenaga, J. (2016). The seismic Moho structure of Shatsky Rise oceanic plateau, northwest Pacific Ocean. Earth and Planetary Science Letters, 441, 143–154.

Zhang, J., Sager, W. W., & Durkin, W. J. (2017). Morphology of Shatsky Rise oceanic plateau from high resolution bathymetry. Marine Geophysical Research, 38(1–2), 169–185.